POLITECNICO DI TORINO

Master's Degree in Mechanical Engineering

Master's Thesis

Aeromechanical Optimization of Aeronautical Low-Pressure Turbine Components

Avio Aero
A GE Aviation Business

Supervisors:

Prof. Christian Maria Firrone

Ing. Marco Moletta

Candidate:

Valeria Pinto

April 2020

Abstract

The aeronautical market is facing a continuous expansion and the competition among the main aircraft manufacturers is intensely growing. At the same time, climate changes have become a matter of serious concern for our society and stringent limitations on polluting emissions have been introduced. Therefore, great emphasis is placed on producing engines able to combine high efficiency with excellent performance and reliability. The engine's overall improvement comes from optimization of the key engine's components from different engineering points of view; among them, Low Pressure Turbines (LPT) play a crucial role. The design process of an LPT involves many different disciplines (such as Aerodynamics, Vibration Mechanics, Aeroelasticity, etc.) and, consequently, many specifications must be taken into account. In particular, the need of decreasing the overall system mass has led to critical engineering issues and, among these, Aeromechanical stabilization has become one of the top priorities. In order to contain costs and time related to the design process, it would be convenient if the main aspects and related parameters coming from different optimization perspectives were all already considered in the early phases of the design process. The thesis work here presented, carried out in collaboration with GE Avio Aero, starts from a previous aerodynamics-focused study conducted by means of the Smith Chart and the two main parameters that it introduces: the Flow Coefficient and the Stage Loading Factor. The purpose is the identification of the blade profiles that show the best performance in terms of aeromechanical stabilization and to compare them with the best results from the aerodynamic point of view. The final target is to promote a functional integration between Aerodynamics and Aeromechanics in early design phases, in order to make the design process more efficient and less time-consuming.

Contents

1 Introduction

The goal that research in the aeronautic field has always tried to pursue is that of satisfy the requirements of a sector that is constantly growing, by offering increasingly higher quality standards and by adopting sustainable solutions under the economic and ecologic profile. This purpose has guided the evolution of the sector through the years, by means of technological processes that made air transport ever safer, more comfortable and more efficient. However, nowadays a new important step forward is required and it has to do with environmental requirements.

1.1 Great 2020

The European Commission, together with experts group ACARE (Advisory Council for Aviation Research and Innovation in Europe), has set the sector's strategic goals to be achieved by 2020 and by 2050. These objectives may be summarized in the following points:

- higher efficiency, which would lead to an overall quality improvement of the service offered to the user, including safety, vehicle on-board comfort and flight punctuality:
- a drastic reduction of the environmental impact.

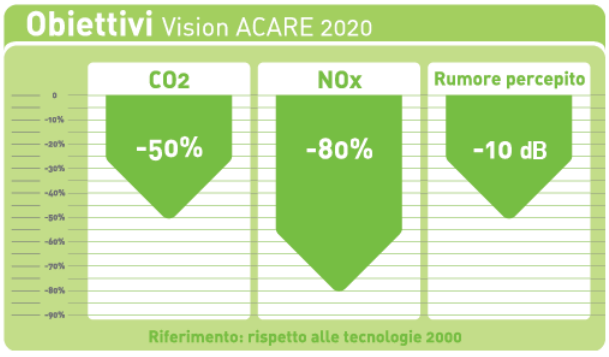

Efficiency and ecocompatibility goals bring into play every level of the aeronautic sector and the research sector in particular. In fact, several European research projects have been promoted with the purpose of leading to the development of technologies needed in order to achieve ACARE objectives. In this context, a series of projects have been launched in Europe, and among them there is the Green Engines for Air Traffic 2020 project (GREAT 2020). In Piedmont, this focus on research activities resulted in a partnership between Politecnico di Torino and GE Avio Aero, which led to founding of Great Lab in 2008.

2 The aircraft engine

The first attempts of using gas turbine engines as aircraft power plants date back to the first decades of 1900. In 1913 René Lorin, a French engineer, patented the first jet propulsion engine but at that time it could not be manufactured or used for two main reasons: firstly, suitable heat resisting materials were not developed yet; furthermore, jet propulsion would have been extremely inefficient at the low speeds of the aircrafts of those days. Later, in 1930, Frank Whittle obtained his first patent for using a gas turbine to produce a propulsive jet, but it completed its first flight only eleven years later. However, it can be said that Whittle's engine set the basis for the modern gas turbine engine.

Jet propulsion is a practical application of Newton's Third Law that states that *for every force acting on a body there is an opposite and equal reaction.* When applying it to aircraft propulsion, the "body" is the atmospheric air that is accelerated through the engine; the force employed to cause this acceleration has an equal effect in the opposite direction, so there is a force acting on the system that is producing the acceleration. This reaction force, called *thrust*, is proportional to the mass of the air expelled by the engine and to the velocity change imparted to it. This means that the same thrust can be obtained by giving a small acceleration to a large mass of air or by giving a large acceleration to a small quantity of air. In practice, the former option is preferred, as it allows to obtain a higher propulsive efficiency[1].

The gas turbine is essentially a heat engine that uses air as a working fluid. In order to obtain the air acceleration needed to provide the thrust, first of all the air pressure energy is increased (with velocity decreasing), then there is the addiction of heat energy and finally all the energy is converted into kinetic energy. Therefore the engine working cycle, named *Brayton cycle*, is composed by four phases: induction, compression, combustion and exhaust. The combustion occurs at a constant pressure and it occurs continuously, thus enabling more fuel to be burnt in a shorter time - when compared, for

instance, to a piston engine - and so a greater power output for a given size of the engine.

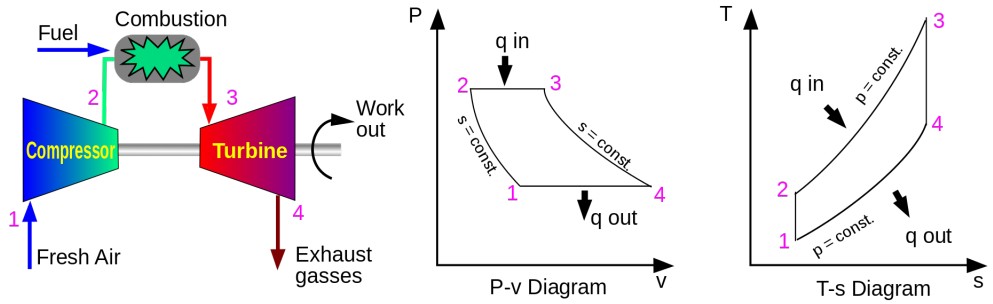

Figure 2: Idealized Brayton cycle [28].

2.1 Main types of aircraft engines

Engines employed for aircraft propulsion are usually called air breathing jet engines, in order to underline that in these kind of reaction engines the air is forced into the engine itself. There are different types of jet engines, each of which has benefits, drawbacks and best use cases.

2.1.1 Turbojet engine

The turbojet engine concept was developed independently by two engineers, Frank Whittle in the UK and Hans Von Ohain in Germany, during the late 1930s. Turbojets are made up of five main components: inlet, compressor, combustor, turbine and propelling nozzle. Differently from the turbofan, in the turbojet all the inlet air passes through each element of the engine. After entering the engine through an inlet duct, the air pass through the compressor that increases its pressure and then reach the combustion chamber, where fuel is injected. The heat developed by the combustion leads to an expansion that takes place thorough the turbine. The turbine exhaust is then expanded in

the propelling nozzle, where it is accelerated to high speed to provide thrust. Beyond the basic configuration that features a single compressor driven by a single turbine, it is possible to have more complex configurations in which the compression and the expansion are split among two or more stages of compressor and turbine. For instance, in a twin-spool engine (shown in Figure 3) there is a low-pressure compressor driven by a low-pressure turbine and a high-pressure compressor driven by a high-pressure turbine. The two units rotate at different speeds in order to maintain a high efficiency in all stages of compression.

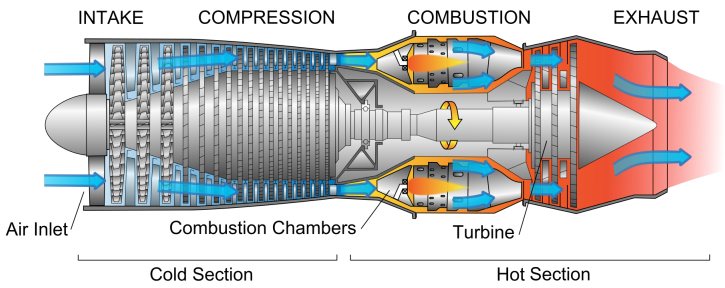

Figure 3: Twin-spool turbojet engine [30].

2.1.2 Turbofan engine

The turbofan engine, largely employed in modern aircraft, features the same components described in 2.1.1 with the addiction of a particular low-pressure compressor, usually known as *fan*, that compresses air into a bypass duct whilst its inner portion supercharges the core compressor. The bypass air, that do not take part to the combustion process, either passes through a separate "cold nozzle" or mixes with the low-pressure turbine exhaust gases and then expands through a "mixed-flow nozzle". Compared to a turbojet able to produce the same thrust, a turbofan has a much larger mass flow rate and a lower velocity of the mixed exhaust air (low specific thrust), as the air flowing in the additional duct has not been ignited and therefore it has a

relatively low speed. Overall, a turbofan can be much more fuel efficient and quieter than a turbojet and it is allows to reach greater net thrust at low speeds.

The bypass ratio can be defined as follows:

$$BPR = \frac{\dot{m}_b}{\dot{m}_c} \tag{1}$$

where $\dot{m}_b$ is the bypass flow and $\dot{m}_c$ is the core flow. In modern engines, ratios from 4:1 up to 8:1 are employed.

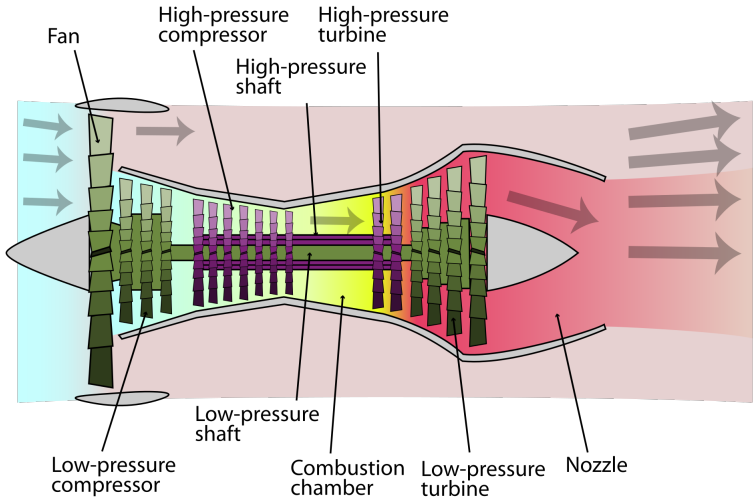

Figure 4: Turbofan engine [31].

2.1.3 Turboprop engine

Turboprop engines are jet engines derivatives in which a portion of the engine's thrust is produced by spinning a propeller and the remaining part comes from the high-speed jet exhaust. They differ from turbofans in that a traditional propeller usually provides the majority of thrust, while a ducted fan only contributes to a minor part of the thrust production. Moreover, most turboprops use gear reduction between the turbine shaft and the propeller, as can been seen in Figure 5. The hot-jet exhaust is an important

contribution to thrust and the maximum thrust is obtained by matching the two thrust contributions. Turboprops have usually better performance than turbojets or turbofans at low speeds (where propeller efficiency is high), while they tend to become noisy and inefficient at high speeds [30]. For this reason, turboprops are used mainly for low speed aicrafts like cargo planes [29].

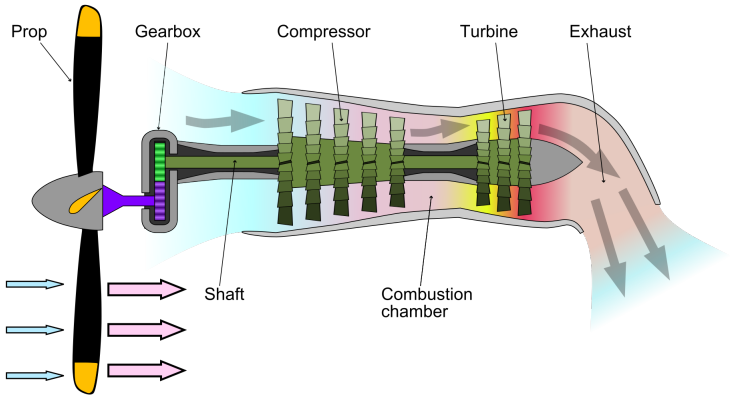

Figure 5: Turboprop engine [30].

2.1.4 Turboshaft engine

Turboshafts are similar to turboprops, with the difference that nearly all energy extracted by the turbine is used to spin the rotating shaft, which is used to power machinery rather than a propeller. Therefore they generate little to no jet thrust and are commonly used in applications that require a sustained high power output, high reliability and small size and weight; these include helicopters but also auxiliary power units, boats and ships [33].

A turboshaft is generally made up of two major part assemblies: the *gas generator* and the *power section*. The gas generator consists of compressor, combustion chamber with ignitors and fuel nozzles and one or more stage of turbine, while the power section includes additional stages of turbine, a gear reduction system and the shaft output. The gas generator extracts energy

from hot expanding gases and such energy is used to drive the power section. Depending on the design, the engine accessories may be either driven by the gas generator or by the power section.

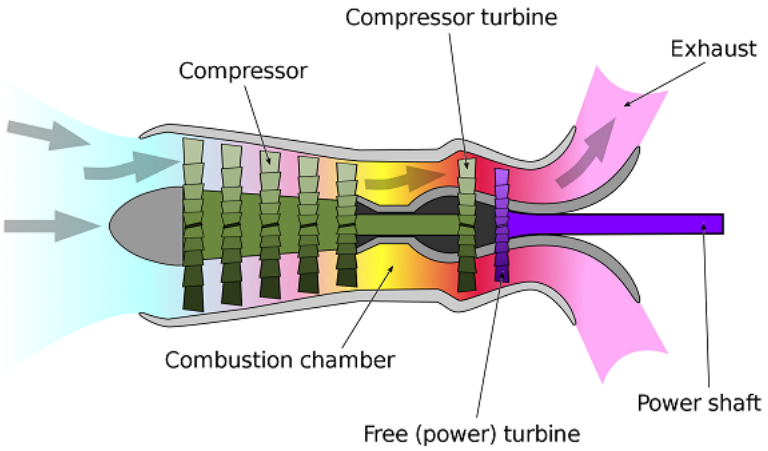

Figure 6: Turboshaft engine [33].

3 Low-pression turbine (LPT)

The turbine has the task of providing the power to drive the compressor and providing shaft power to the propeller or rotor when they are present. It does this by extracting energy from the hot gases released from the combustion system and expanding them to a lower pressure and temperature. To produce the driving torque, the turbine may consist of several stages each employing one row of stationary guide *vanes* (also called *nozzles*) and one row of moving *blades*. The number of stages depends upon the relationship between the power required from the gas flow, the rotational speed at which it must be produced and the diameter of the turbine permitted. In an aircraft engine, the number of shafts, and therefore turbines, varies with the type of engine. High compression ratio engines usually feature two shafts and, consequently, two turbines: the high-pressure turbine drives the high-pressure compressor, while the low-pressure turbine drives the low-pressure compressor and, in the case of a turbofan engine, the fan itself [1].

3.1 Design principles

The turbine expands the flow and extracts work from it. As shown in Figure 7, the change in tangential velocity that occurs in the rotor ($\triangle c_\vartheta$) is in the direction opposite to the blade speed U. As a consequence, there is a change in the tangential momentum of the fluid that results in a torque on the rotor in the direction of motion.

Torque is defined mathematically as the rate of change of angular momentum:

$$\sum \tau = \dot{m} \left[(rc_\vartheta)_2 - (rc_\vartheta)_1 \right], \tag{2}$$

so it is possible to express the power output of a turbine as:

$$P = \dot{m}(U_2 c_{\vartheta 2} - U_3 c_{\vartheta 3}) \,. \tag{3}$$

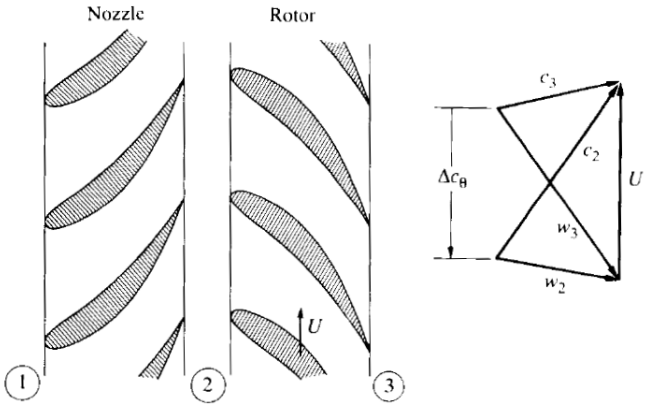

Figure 7: Turbine blades and velocity triangles [2].

In an axial turbine, $U_2 \simeq U_3 = U$, so the turbine work per unit mass is:

$$W_T = U(c_{\vartheta 2} - c_{\vartheta 3}) = c_p(T_{01} - T_{03}) \,. \tag{4}$$

By defining $\triangle T_0 = T_{01} - T_{03} = T_{02} - T_{03}$, the stage work ratio con be written as:

$$\frac{\triangle T_0}{T_{01}} = \frac{U(c_{\vartheta 2} - c_{\vartheta 3})}{c_p T_{01}} \,. \tag{5}$$

If considering the purpose of maximizing the turbine work per stage, it is possible to see that the work may be limited in two different ways:

1. The available pressure ratio, and thus $\frac{\Delta T_0}{T_{01}}$, may be limited; in this case the maximum work will be directly proportional to T_{01}.

2. The available pressure ratio is sufficiently high that the the limit on the work is imposed by the allowable blade speed U and the allowable turning of the fluid Δc_ϑ.

Blade speed is limited by the allowable rotational stresses at the operating temperature, while Δc_ϑ must be limited to maintain high efficiency. The

allowable turning in a turbine stage is much higher than in a compressor stage; in fact, boundary layers in turbines tend to well behave because of the generally falling pressure gradients. However, there could be a zone of adverse gradient, depending on the turning and on the spacing of the blades, and in this region boundary layers could grow rapidly or even separate, with a negative impact on turbine efficiency.

Another parameter employed to characterize the turbine's performance is the *Degree of Reaction*, defined as the ratio of the static enthalpy drop in the rotor to the static enthalpy drop in the stage:

$$R = \frac{\Delta h_{rotor}}{\Delta h_{stage}} = \frac{h_2 - h_3}{h_1 - h_3} \,. \tag{6}$$

Turbine stages in which the entire pressure drop occurs in the nozzle are called *impulse stages*, while stages in which a portion of the pressure drop occurs in the nozzle and the rest in the rotor are called *reaction stages*. Usually, gas turbine engines do not use pure impulse or pure reaction turbine blades but the impulse-reaction combination. Although the degree of reaction depends on the type of engine in which the turbine is to operate and on specific design considerations, its values is usually around 0.5, which means that the enthalpy drop is equally split between the stator and the rotor.

With regard to the 3D design of the turbine, it must be pointed out that the nozzle guide vanes and the blades of the turbine are *twisted*, which means that stagger angle (i.e. the angle between the chord line and the turbine axial direction) is greater at the tip than at the root of the blade, as showed in Figure 9. The purpose of this twist is to make the gas expanding in the turbine do equal work at all positions along the length of the blade and to guarantee a uniform axial velocity of the flow that enters the exhaust system. However, this design leads to some changes in velocity, pressure, temperature and *Degree of Reaction* along the blade radius. In fact, if a value R=0.5 has been chosen for the mean section, there will be R<0.5 at the root and R>0.5 at the tip [1].

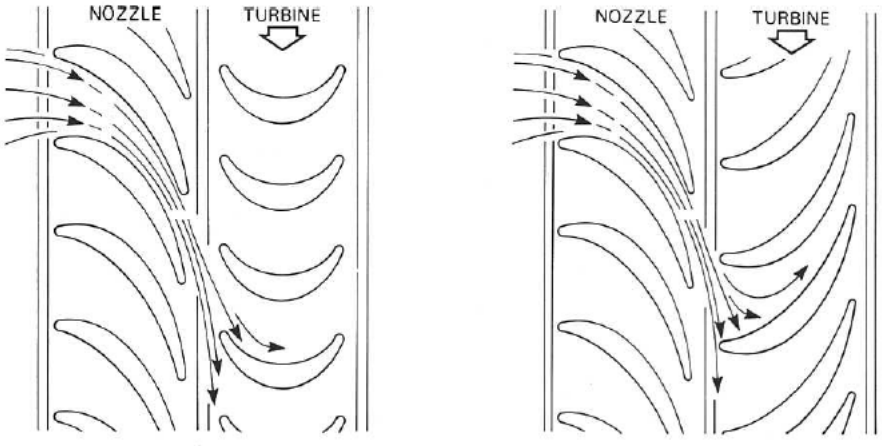

Figure 8: Comparison between a pure impulse turbine (left) and a impulse-reaction turbine (right) [2].

Another important aspect to be considered in the design of either rotating or non-rotating elements of a turbine is the *hot to cold scaling*. Usually, the first step of the turbine's design is the definition of the flow path, that is the channel traveled by the air flow while expanding, that occurs with reference to the *hot condition*. The following steps include the definition of the bi-dimensional profiles that realize the optimum velocity triangles and their interpolation in radial direction in order to obtain the tri-dimensional profile. However, as the turbine assembly takes place in *cold condition*, in order to guarantee the correct positioning of the blade profiles in working conditions, a series of operations need to be performed:

- *Scaling*: it is the scale reduction of the blade profile, performed in order to take into account the dilation due to high temperatures.
- *Twisting*: the blade has to be twisted around the radial direction, so that in operating conditions this twist will disappear as, being the blade loaded by hot gases, it will tend to return to the original design configuration.

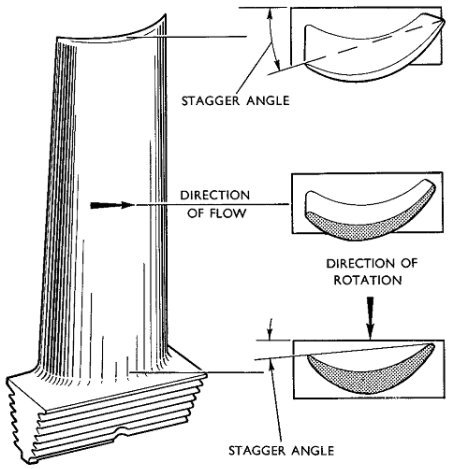

Figure 9: Twisted contour of turbine blades [1].

- *Positioning*: it defines the position of the platforms needed to keep the blade profile fixed (outer bands for the stator and platforms and shrouds for the rotor).

3.2 Stresses in axial flow turbines

The cold blade profile has to be structurally verified by taking into account four main categories of stresses: thermal, centrifugal, bending and vibrations.

1. The high temperature of the exhaust gas flowing through the turbine causes thermal expansion of all components involved. Hence, the components will experience a thermal strain that is generally proportional to the temperature change according to the following equation:

$$\varepsilon_T = \alpha \Delta T \,. \tag{7}$$

Temperature changes do not lead to mechanical stress if the component is free to expand; however, shrouded turbine blades during operation nearly behave as clamped-clamped structures and such condition do not allow the natural extension of the blade. Another phenomenon that may take place

in turbine components is creep, which comes from a long term exposure to levels of stress that are below the yeld strength of the material. In order to limit thermal stresses, attention should be given to the material choice and to to the possibility of providing a cooling system for the blade.

2. Due to high rotation speeds (about 7000 rpm for the low-pressure shaft and 1200 rpm for the high-pressure shaft), centrifugal loads have to be taken into account in the structure validation of the rotor blade. The centrifugal force acting on the selected cross-section is given by:

$$F_c = \int_r^R dF_c = \rho\omega^2 \int_r^R r \cdot dV = \rho\omega^2 \int_r^R rA(r) \cdot dr \,, \tag{8}$$

where ρ is the material density, ω is the rotation speed, $A(r)$ is the blade cross section at the generic radius r and R is the maximum blade radius. From Equation (8) it can be deduced that the section that is most afflicted by centrifugal stress is the root. Consequently, in order to prevent the blade root failure, a possible solution is a suitable design of the *shank* between the root and the platform.

3. The blade root is also subjected to the bending moment that comes from the pressure exerted by hot gases on the pressure side of the blade (and, in particular, from its stationary component). As showed in Figure 10, an efficient way to attenuate the bending stress at the root generated by M_{flow} is introducing a blade skew in the flow direction. In practice, an inclination of 1 or 2 degrees with respect to the radial direction is given to the airfoil and, as a consequence, the centrifugal force will generate a moment M_c that will compensate M_{flow}. Of course, a total compensation can only occur for a specific value of the rotation speed, while for other working conditions the bending stress will be decreased but not completely eliminated.

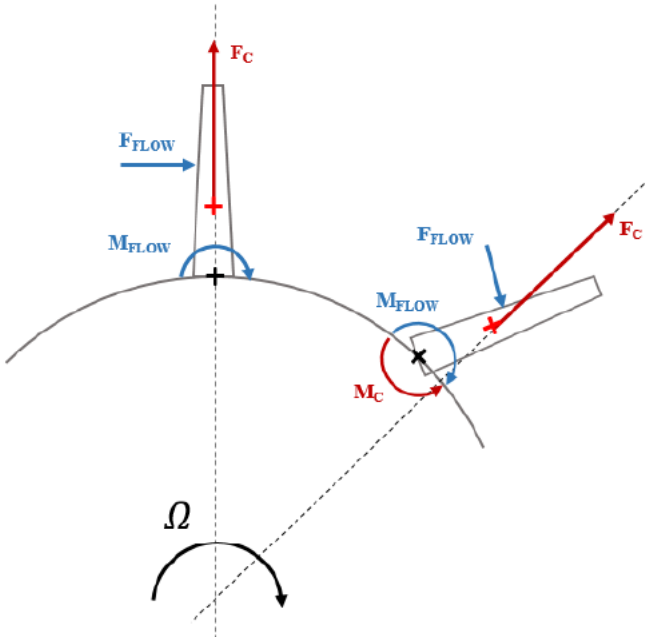

Figure 10: Compensation of the aerodynamic momentum M_{flow} with the momentum produced by the centrifugal force M_c.

4. Finally, turbine bladed discs are affected by vibration stresses that results from dynamic excitations that fall into two categories, depending on the source that generates them:

- mechanical excitations: they may derive from wrong rotor balance (*whirl*) or from contact between blade tip and casing;
- aerodynamic excitations: they are caused by the non-stationary component of the gas flow pressure and may derive from flow-structure interaction in presence of a non-uniform circumferential pressure distribution, stator-rotor interactions and self-excited aeroelastic phenomena (*flutter*).

In bladed discs, both mechanical and aerodynamic excitations are the main responsible for high cycle fatigue (HCF). Therefore, the design of blade and

discs is a very complex process and a compromise must be found between structural resistance and weight limitations, which are mandatory in order to achieve high efficiency.

3.3 Efficiency definitions

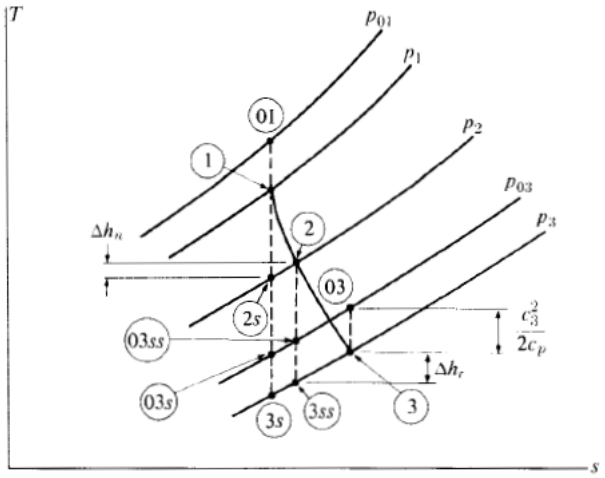

Figure 11: Expansion in a turbine stage (T-s diagram) [2].

There are two turbine efficiency definitions in common usage; the choice between them depends on the application for which the turbine is used [2]. For some conventional turbine applications, the useful output consists of the shaft power and the exhaust kinetic energy is considered as a loss. In this case the ideal turbine would be an isoentropic machine with no exhaust kinetic energy and work could be evaluated as:

$$W_{T,ideal} = c_p(T_{01} - T_{3s})\,. \tag{9}$$

This consideration leads to the definition of the *total-to-static efficiency*, that can be written as:

$$\eta_{ts} = \frac{T_{01} - T_{03}}{T_{01} - T_{3s}} \,. \tag{10}$$

However, in some applications, particularly turbojets, the exhaust kinetic energy is not considered a loss since exhaust gases are intended to come out of the turbine with high velocity. In this case, the ideal work is:

$$W_{T,ideal} = c_p \left(T_{01} - T_{3s} + \frac{c_3^2}{2c_p} \right) = c_p (T_{01} - T_{03s}) \,. \tag{11}$$

This leads to the definition of the *total-to-total-efficiency*, defined by:

$$\eta_{tt} = \frac{T_{01} - T_{03}}{T_{01} - T_{03s}} \,. \tag{12}$$

However, the energy associated with the tangential component of the exhaust velocity must be considered a loss, since it will not give any contribution to the thrust.

3.4 Performance parameters

Generally, in early stages of a turbine's design process, namely *Concept* and *Preliminary Design*, geometric dimensions are still unknown, as they are parameters that need to be optimized. For this reason, some dimensionless parameters are introduced in order to study how the turbine operates; the main parameters introduced in this phase are:

- the *Stage Loading Factor*;
- the *Flow Coefficient*;
- the *Degree of Reaction*.

The *Stage Loading Coefficient* is defined as:

$$\psi = \frac{\triangle H}{U^2} \,, \tag{13}$$

where $\triangle H$ is the enthalpy gap on a single row and U is the tangential velocity. Evaluating the maximum $\triangle H$ that it is possible to obtain through the single turbine stage is essential in order to choose the number of stages. In fact, once the thermodynamic cycle is known, the total enthalpy change across the turbine will be divided among a certain number of stages, taking into account temperature and velocity limitations on each stage. The *Stage Loading Factor* is therefore one of the most significant indicators of the stage efficiency as it influences the off-design operation conditions. This coefficient can also be interpreted as the ratio of the specific work produced by one real stage to half the specific work produced by a reference stage that operates at the same tangential velocity U. In fact, if the considered reference stage has null swirl angle ($\alpha_3 = 0 \Rightarrow c_{\vartheta 3} = 0$) and null degree of reaction ($R = 0 \Rightarrow w_2 = w_3$), the specific work produced by it will be equal to $2U^2$. Therefore, Equation (13) can be written as:

$$\psi = \frac{\triangle H}{U^2} = \frac{U(c_{\vartheta 2} - c_{\vartheta 3})}{U^2} = \frac{(c_{\vartheta 2} - c_{\vartheta 3})}{U} \,. \tag{14}$$

It is possible to observe that a turbine stage with high loading factor will be characterized by high flow deflection, which in turn leads to high losses and low stage efficiency. On the other hand, low loading factors are associated with high values of peripheral speed, which would impact negatively on the engine dimensions and weight, that are subjected to strict limitations.

Another important parameter is the *Flow Coefficient*, which is the ratio of the flow axial speed to the peripheral speed:

$$\phi = \frac{c_{ax}}{U} \,. \tag{15}$$

Low values of the coefficient implies high flow deflections, while for high values the flow deflection is small and the blade's profile will be more stretched in the axial direction and more slender. Therefore, limitations on the values of the flow coefficient are usually introduced in order to minimize losses [21]:

$$0.4 < \phi < 1.4\,. \tag{16}$$

In fact, for $\phi < 0.4$ the high flow deflection would lead to potential high losses due to flow detachment on the blade suction side. On the other hand, choosing $\phi > 1.4$ would lead to high profile losses, as these losses are proportional to the square of the velocity and will result not negligible. For each value of the *Stage Loading Factor* it is possible to identify a corresponding value of the *Flow Coefficient* so that a good compromise between losses associated with flow detachment and profile losses can be obtained. The dependency of turbine's efficiency on ψ and ϕ values can be investigated by mean of the *Smith Chart* (3.5).

After the enthalpy variation has being split among the turbine's stage, it has to be further divided between the stator and the rotor of the single stage. This consideration leads to the last dimensionless parameter, which is the *Degree of Reaction*, already introduced in 3.1:

$$R = \frac{h_2 - h_3}{h_1 - h_3}\,. \tag{17}$$

This parameter defines the enthalpy variation over the rotor as a percentage of the total enthalpy variation over the stage. Figure 12 shows how the turbine's efficiency is related to the *Degree of Reaction*. Aeronautical turbines usually work with R=0.5, which means that the enthalpy variation is equally divided between stator and rotor; this leads to a higher efficiency with respect to the other possible values of R.

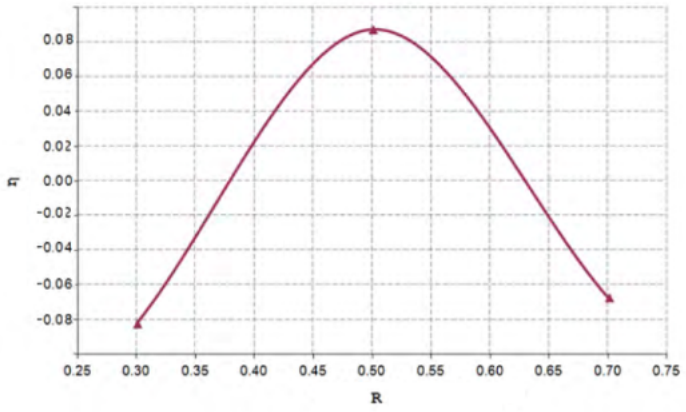

Figure 12: Turbine's efficiency versus Degree of Reaction [20].

3.5 Smith Chart

By considering the *Stage Loading Factor* and the *Flow Coefficient* introduced in 3.4, it is possible to represent the different types of turbine on a $\phi - \psi$ diagram. Different authors, among them Shapiro, Soderberg, Stening, Taylor and Horlock, gave contribution to this classification; the results are shown in Figure 13:

It can be observed that each type of turbine works in a certain range of $\phi$and ψ. Pelton turbines, employed for hydroelectric power generation, are the most efficient among the impulse turbines; they work with low mass flow and high loads, so they are reported in the low ϕ region. On the other hand, Kaplan turbines work with higher flow mass and low loads, so they a re located in the low ψ region. The most largely employed hydraulic turbines are Francis turbines, that are able to work in a wider range of flow mass and with higher loading factors with respect to Kaplan turbines.

The diagram also shows the lines that correspond to constant values of

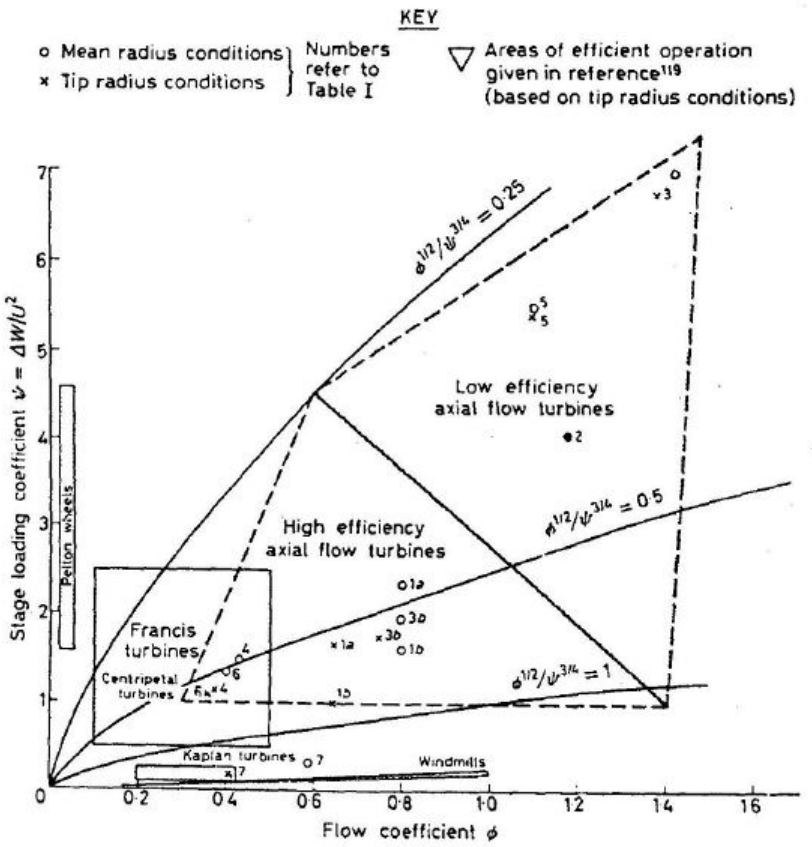

Figure 13: Different types of turbine on a $\phi - \psi$ diagram [3].

the adimensional parameter defined as:

$$k = \frac{\phi^{1/2}}{\psi^{3/4}} \,. \tag{18}$$

ACARE 2020 objectives, in terms of CO2, NOx and noise emissions [37].This parameter allows the designer to have a preliminary idea of the most suited type of turbine for the considered design conditions.

Aeronautical applications generally employ high efficiency axial turbines. A detailed experimental study on this specific type of turbines has been

conducted by Smith in 1965 [5]. He focused his attention on the diagram area represented in Figure 14, thus giving a fundamental contribution to the design method for aeronautical turbines.

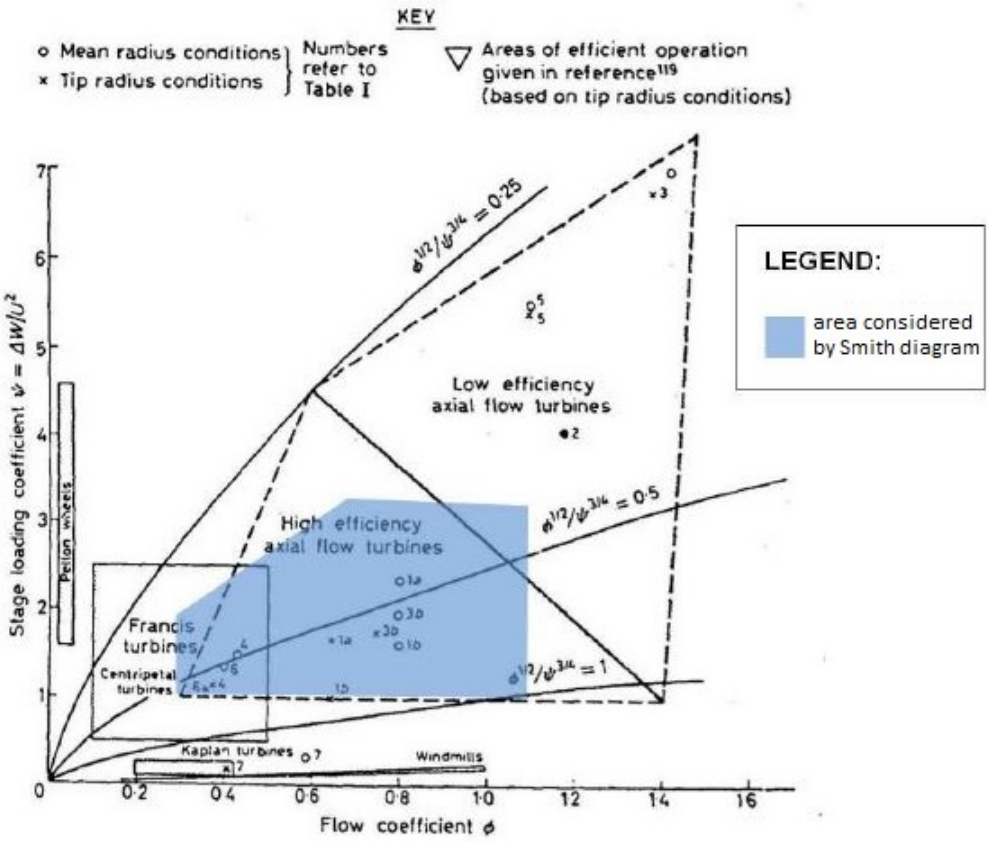

Figure 14: $\phi - \psi$ diagram's area considered by Smith [20].

The original Smith chart represents the isoefficiency curves (considering η_{TT}) obtained by the experimental analysis of 70 axial turbines characterized by constant axial velocity over the stage, null incidence angle at design point and a degree of reaction (evaluated at the mean radius) which varies between 0.2 and 0.6. Moreover, the Reynolds number varies between 10^5 and $3 \cdot 10^5$ and the *aspect ratio* (defined as the ratio of the blade's height to the mean

axial chord) ranging from 3 and 4. Effects related to Mach number variation or to the leading edge thickness are not taken into account.

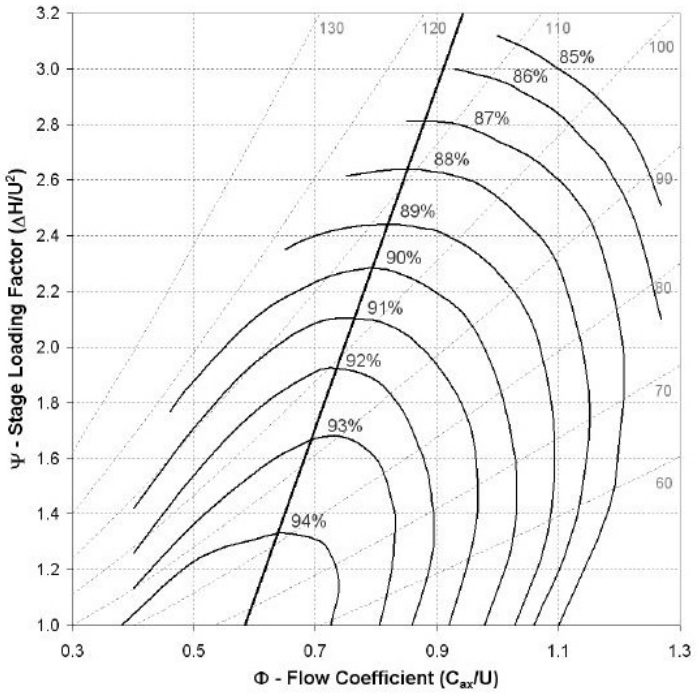

Figure 15: Smith chart [5].

Smith chart, showed in Figure 15, reports and the horizontal axis the *Flow Coefficient* and on the vertical axis the *Stage Loading Factor*. Three kind of curves are reported: the isoefficiency curves, the rotor's deflection angle curves and the optimum line, which identifies for each value of ϕ the corresponding value of ψ that allows to reach the maximum efficiency. Smith chart is an useful tool to be employed during the *Concept* and *Preliminary Design* phases, as it allows to infer the operating conditions of the considered turbine's stage starting from the knowledge of simple aerodynamic parameters. In fact, once ϕ and ψ have been defined, it is possible to desume the stage efficiency, the rotor's deflection angle and the distance of the operating point from the optimum line. Therefore, by varing the input parameters, it is

possible to move the operating point across the whole chart. From Figure 15 it is possible to observe that maximum efficiency values occur at low values of ϕ and ψ, while for deflection angles lower than 40° or higher than 130° losses become very high.

It is possible to represent different types of axial turbines on the Smith chart in order to highlight the differences that occur in terms of *Stage Loading Factor*, *Flow Coefficient* and Efficiency (Figure 13). Power generation turbines fall in the high efficiency area, as they do not have strict weight limitations so they can operate with low loading factors as well as low flow coefficients. In the central area of the diagram it is possible to find aeronautical turbines for civil application, that works with intermediate value of loading factor and flow coefficients, as a result of the compromise between low turbine weight and high efficiency; typical value of the load factor are around $\psi = 2$. Finally, in the upper part of the chart there are turbines for military application, that requires high specific power at the expenses of fuel consumption; consequently, they operate with high loads and relatively low efficiency.

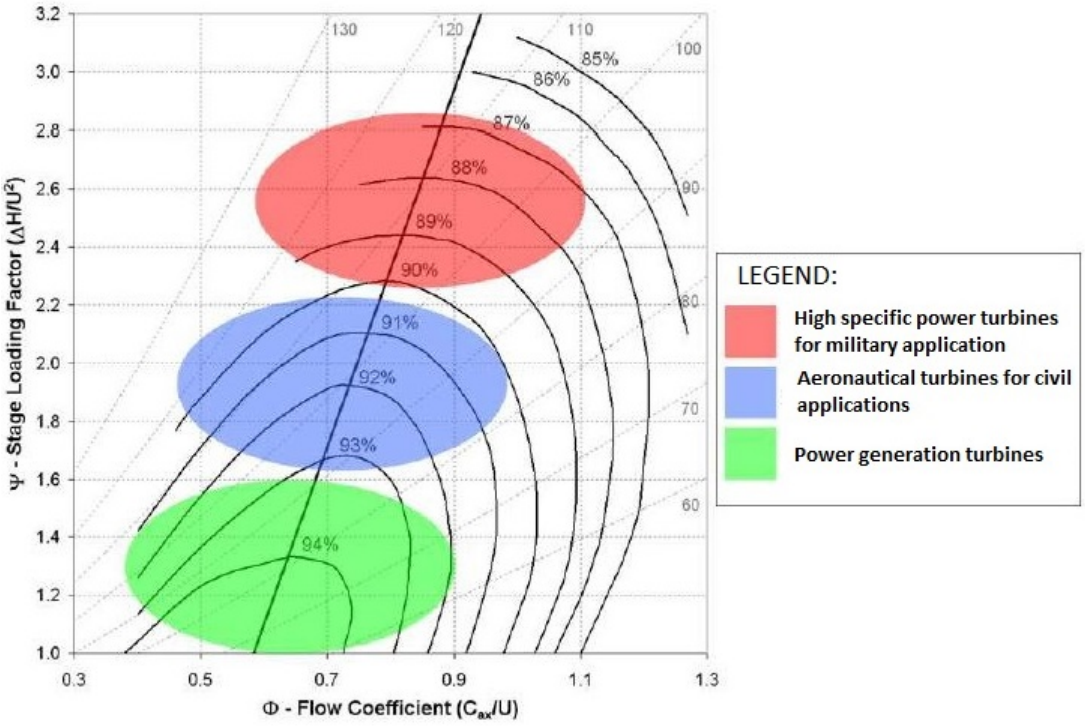

Figure 16: Different types of axial turbines on the Smith chart [20].

3.6 Use of the Smith chart in the design phase

Smith chart allows the representation of the turbine stage efficiency under development by mean of the aerodynamic parameters available to the designer. During the design phase it is possibile to decide in which area of the Smith diagram the turbine stage will operate by varying two main parameters: the number of stages and flow channel's height. On the other hand, the OEM (*Overall Engine Manufacturer*) imposes to the turbine designer the rotational speed (which depends on the fan rotational speed), inlet and outlet radius, the flow rate, the length of the turbine module and inlet and outlet pressures. The power generated by the turbine can be written as:

$$W = \dot{m} \triangle H \,, \tag{19}$$

where $\triangle H$ and W are respectively the enthalpy change and the power referred to the whole turbine module. The designer can move the operating point on the *Smith Chart* by varying the load on the single stage (and therefore ψ), which in turn involves a variation of the number of stages. In fact the turbine power can be reformulated as follows:

$$W = \dot{m} \triangle H = \dot{m} \triangle H_m N_{stages} \,, \tag{20}$$

where $\triangle H_m$ is the enthalpy change over the single stage and N_{stages} is the number of turbine stages. As regards the possibility to vary the *Flow Coefficient* ϕ, it has to be taken into account that the flow rate is imposed by the OEM and it influences the turbine power. By introducing the definition of flow rate:

$$\dot{m} = \rho A c_{ax} \simeq \rho r_m h_m c_{ax} \,, \tag{21}$$

it can be seen that, being the flow rate and the mean radius fixed, the mean channel height h_m is the only free parameter that can be changed in order to vary $c_{ax}$and therefore ϕ.

As concerns the *Degree of Reaction*, it must be taken into account that inlet and outlet speeds and flow angles are imposed and, as a consequence, there is a constraint on the Degree of Reaction's evolution across the stage, particularly for the first and the last stages, which operating condition will differ from the ideal condition $R = 0.5$.

Another parameter to be considered in order to move the operating point over the Smith Chart is the deflection angle. The relation that links the rotor deflection δ_b to the three main performance parameters ϕ, ψ and R, can be analytically deduced and it is reported in Equation (22) [20].

$$\tan \delta_b = \frac{\frac{\psi}{\phi}}{1 - \frac{1}{4\phi^2}(\psi^2 - 4R^2)} \,. \tag{22}$$

By referring to the mathematical formulation or, more simply, to Figure 15, it can be deduced that deflection increases when ϕ decreases and ψ increases; as concerns the Degree of Reaction, when R increases, deflection tends to decrease on the rotor and to increase on the stator.

The variation of the previously mentioned parameters has the purpose of moving the operating point as close as possible tot the optimum line. This line allows to identify, for a given efficiency, the maximum load that is possible to have on the single stage; in fact, the aim of the design process is to reach a good compromise between load and efficiency. Moreover, being able to evaluate the operating point relative position with respect to the optimum line in the early phases of the design process allows to act on turbine parameters and modify them, thus avoiding significant increase in costs and time.

3.7 Zweifel's Criterion

In 1945, Zeweifel adressed the issue of the optimal blade solidity and he got to the formulation of a theory that allows to find the optimal ratio between tha tangential step (s) and the profile's axial chord (c_{ax}). By consindering the axial chord constant, if the step is drecreased the flow will be better guided through the channel and this will result in a lower load on each profile. However, this implies a higher number of blades and thus an increment in the blade's surface, which would lead in turn to higher profile losses. On the other hand, by increasing the profile step, losses would lower but the number of blades would decrease and therefore the load acting on each blade would increase, thus leading to increasing secondary flows.

Zweifel's Criterion affirms that the ratio between the real load and the ideal load acting on a blade should be as near as possible to a constant value

that allows losses limitation. Ideal and real load distributions are showed in Figure 17. The ideal pressure distribution is the one that shows the maximum load on the profile in absence of flow separation on the suction side. If the load distribution on a real profile is considered, the maximum pressure value can be found on the pressure side at the stagnation point; the pressure trend is then decreasing until the value p_2 is reached at the row's exit. On the suction side, pressure tends to decrease down to a minimum; after that, it increases up to the trailing edge. From a theoretical point of view, pressure on suction side could decrease until very low pressure levels are reached. However, in practice, below a certain level of pressure fluid detatchment phenomena occur. Therefore, pressure condition on suction side defines the maximum load that a profile can withstand. The real aerodynamic load for

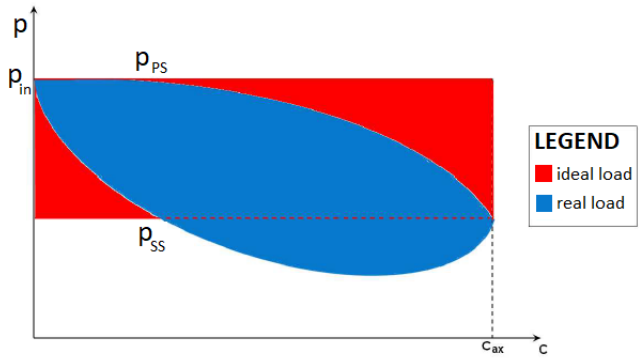

Figure 17: Aerodynamic load distribution on a blade's profile.

unit of length acting on the blade can be written as:

$$W = \int_0^{c_{ax}} (p_{PS} - p_{SS}) dx \, . \tag{23}$$

Under the assumption of incompressible flow, static pressure at the row's inlet and outlet can be respectevely expressed as:

$$p_1 = p_{tot} - \frac{1}{2}\rho c_1^2 \, ; \qquad p_2 = p_{tot} - \frac{1}{2}\rho c_2^2 \, . \tag{24}$$

The ideal load condition is reached when total pression is acting on pressure side, while the static pressure value is reached on the suction side:

$$W_{id} = \int_0^{c_{ax}} (p_{tot} - p_2) dx = (p_{tot} - p_2) c_{ax} \, . \tag{25}$$

The expression of Zweifel Coefficient for an incompressible flow is given by:

$$Zw = \frac{W}{W_{id}} = \frac{\int_0^{c_{ax}} (p_{PS} - p_{SS}) dx}{(p_{tot} - p_2) c_{ax}} \, . \tag{26}$$

Therefore, through simple mathematical passages, the expression of Zweiful Coefficient for an incompressbile flow in stationary condition can be obtained:

$$Zw = \frac{W}{W_{id}} = \frac{\rho s c_{ax}^2 (\tan \alpha_1 - \tan \alpha_2)}{\frac{1}{2} \rho c_2^2 c_{ax}} = 2 \frac{s}{c_{ax}} \cos^2 \alpha_2 (\tan \alpha_1 - \tan \alpha_2) \, . \tag{27}$$

It is possible to observe that by increasing the solidity ($\sigma = s/c_{ax}$), Zweifel Coefficient decreases; on the contrary, an increasement in Zweifel Coefficient leads to an increasment in the load acting on the profile, with higher values of pressure on the pressure side and lower values of pression on the suction side. By carrying out a series of analyses on turbine cascades, Zweifel observed that minimum losses are obtained for $Zw \cong 0.8$ for stators and $Zw \cong 1$ for rotors. Therefore, once the geometrical angles are fixed, by using 27 it is possible to find the optimal solidity that allows to minimize losses. In the modern design of turbine cascades, Zweifel coefficient is in part outdated as modern cascades often works with $Zw > 1$ and allows to contain losses at the same time, thanks to an adequate design. Nevertheless, it is correct to state the an optimal value of solidity can be found: in fact, when blades number is too high profile losses increase, while when blades number is too low, diffusion losses increase, so a compromise must be found.

4 Rotor dynamics

In order to optimize the design of bladed discs, all the source of stresses mentioned in 3.2 have to be taken into account. However, among these, a particular importance is usually given to time-varying excitations, as they are the major responsibles of failure due to HCF. Therefore, studying the bladed discs dynamics is essential in order to obtain an accurate prediction of natural frequencies and mode shapes, in order to manage to limit the effects of unavoidable resonances that may occur during turbine operation.

4.1 Cyclic symmetry

Bladed discs fall in the category of structures showing *rotational periodicity* or *cyclic symmetry*, which means that they consist of a finite number of identical substructures or sectors forming a closed geometry. From a mathematical point of view, the main characteristic of these structures is that the disc geometry for any radial and axial position at a certain angle θ is identical to the geometry at the angular position $(\theta + n\alpha_n)$. The angle $\alpha_n = 2\pi/N$ represents the so-called *sector angle*, while N is the number of disc sectors and $n = 1, ..., N$ is the number of the considered disc sector.

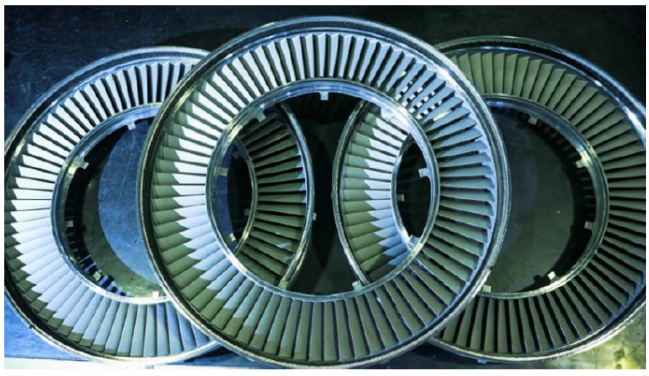

Figure 18: Example of cyclic symmetry structure [35].

4.2 Mode shapes of structures in cyclic symmetry

In order to evaluate natural frequencies and mode shapes of complex structures, *Finite Element* (FE) analysis is performed. This procedure, also known as *meshing*, consists of the discretization of the structure in a certain number of elements, thus allowing to turn a continuous structure into a descrete mathematical model, characterized by a mass and a stiffness matrix, M and K respectively. By applying the aforementioned discretization, the bladed disc can be studied as a *Multi Degrees of Freedom* (*multiple DOF*) system, whose linear and conservative equation of motion can be expressed in the following general form:

$$M\left\{\ddot{x}(t)\right\} + K\left\{x(t)\right\} = F(t)\,, \tag{28}$$

where $x(t)$ is the vector containing the nodal displacements, $\ddot{x}(t)$ the acceleration vector and $F(t)$ is the vector of external forces. If n_n is the total number of nodes resulting from the discretization, the following statements hold:

$$\begin{array}{ll} M \in \mathbb{R}^{3n_n \times 3n_n} & K \in \mathbb{R}^{3n_n \times 3n_n} \\ x(t) \in \mathbb{R}^{3n_n \times 1} & f(t) \in \mathbb{R}^{3n_n \times 1} \end{array}\,. \tag{29}$$

M is positive definite, while K is generally semi-positive definite, as it allows null elements. When considering a cyclic structure, it is convenient to rearrange matrices and vectors so that n_s DOF of the first sector are followed by n_s DOF of the second sector and so on:

$$M = \begin{bmatrix} M_0 & M_1 & M_2 & \dots & M_2 & M_1 \\ M_1 & M_0 & M_1 & \dots & M_3 & M_2 \\ M_2 & M_1 & M_0 & \dots & M_4 & M_3 \\ \vdots & \vdots & \vdots & \ddots & \vdots & \vdots \\ M_2 & M_3 & M_4 & \dots & M_0 & M_1 \\ M_1 & M_2 & M_3 & \dots & M_1 & M_0 \end{bmatrix} \quad K = \begin{bmatrix} K_0 & K_1 & K_2 & \dots & K_2 & K_1 \\ K_1 & K_0 & K_1 & \dots & K_3 & K_2 \\ K_2 & K_1 & K_0 & \dots & K_4 & K_3 \\ \vdots & \vdots & \vdots & \ddots & \vdots & \vdots \\ K_2 & K_3 & K_4 & \dots & K_0 & K_1 \\ K_1 & K_2 & K_3 & \dots & K_1 & K_0 \end{bmatrix}$$

$$x = \begin{Bmatrix} x_1 \\ x_2 \\ x_3 \\ \vdots \\ x_{N-1} \\ x_N \end{Bmatrix} \quad f = \begin{Bmatrix} f_1 \\ f_2 \\ f_3 \\ \vdots \\ f_{N-1} \\ f_N \end{Bmatrix} . \tag{30}$$

M and K have a *block circulant symmetric* structure, where the submatrices M_h and K_h are symmetric matrices of dimension $3n_s \times 3n_s$ and

$$\begin{cases} h = 0, ..., \frac{N}{2} & if\ N\ is\ even \\ h = 0, ..., \frac{N-1}{2} & if\ N\ is\ odd \end{cases} . \tag{31}$$

After the mass and stiffness matrix are obtained through the FE model, natural frequencies and mode shapes can be obtained by solving the following eigenproblem:

$$\left(K - \omega_i^2 M\right) u_i = 0 \qquad i = 1, ..., N \cdot n_s \, , \tag{32}$$

where ω_i^2 and u_i are the real i^{th} eigenvalue and eigenvector respectively. The eigenvector can be written as follows:

$$u_i = \begin{bmatrix} (u_{1i})^T & (u_{2i})^T & \dots & (u_{Ni})^T \end{bmatrix}^T , \tag{33}$$

where u_{ni}, $(n = 1, ..., N)$ is a vector of size n_s containing the modal displacements of the n^{th} substructure when the i^{th} mode shape occurs.

When looking at the mode shapes of a cylindrical symmetrical structure, there are three possible cases.

1. Each sector has the same mode shape as its neighbors and vibrates in-phase with them:

$$u_{n_i} = u_{(n+1)_i} \qquad \forall n \, . \tag{34}$$

It follows that the mode shape of the complete structure can be written as $\begin{bmatrix} (u_{1i})^T & (u_{1i})^T & \dots & (u_{1i})^T \end{bmatrix}$ and it can clearly be observed that a rotation of the mode shape of an arbitrary number of sectors would leave the mode shape unchanged. In this case what we observe is a *standing wave mode shape*, which is described by a single eigenvalue and a single eigenvector.

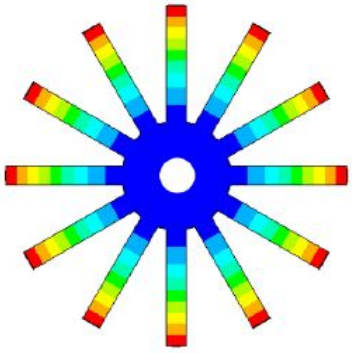

Figure 19: Example of a standing wave mode shape with the blades vibrating in-phase with each other [19].

2. Each sector has the same mode shape as its neighbors, but it vibrates

in anti-phase with them:

$$u_{n_i} = -u_{(n+1)_i} \,. \tag{35}$$

Therefore, the displacement of the whole structure can be written as $\begin{bmatrix} (u_{1i})^T & -(u_{1i})^T & (u_{1i})^T & \dots & (u_{1i})^T - (u_{1i})^T \end{bmatrix}^T$. In this case, a rotation of the mode shape of an even number of sections leaves the mode shape unchanged, while a rotation of an odd number of sections will result in a mode shape with inverted sign $(-u_{1i})$. This means that the mode shape experience a change of phase of π, but it is still a standing mode and so it can be described by a single eigenvalue and a single eigenvector.

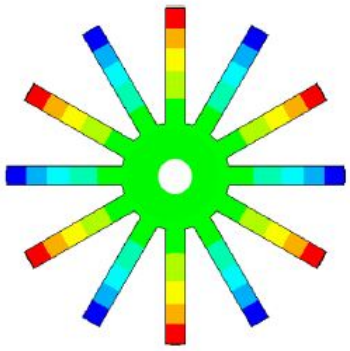

Figure 20: Example of a standing wave mode shape with the blades vibrating in anti-phase with each other [19].

3. For all other existing mode shapes, it is possible to write:

$$u_{n_i} \neq u_{(n+1)_i} \,, \qquad u_{n_i} \neq -u_{(n+1)_i} \qquad \forall n \,. \tag{36}$$

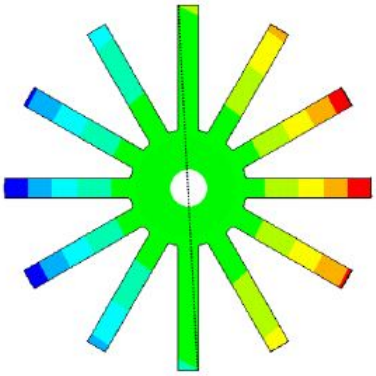

Figure 21: Example of a rotating mode shape [19].

These modes occur in orthogonal pairs of standing waves, described by the same eigenvalue and the same eigenvector. Their combination results in a *rotating mode shape*. Since all the sectors are identical, by shifting a mode shape u_i of one sector's angle α_n, the new mode shape $u_i^{'}$ will have the same eigenvalue as the starting mode shape. Therefore, the set of all possible eigenvectors obtained by performing sequential shifts of u_i, each one of an angle equal to α_n, is given by:

$$U_i = \left[\begin{array}{cc} u_i & \bar{u}_i \end{array} \right] , \tag{37}$$

where $u_i^T \cdot \bar{u}_i = 0$ and the corresponding eigenvalue is ω_i^2 for both eigenvectors. Moreover, the eigenvector $u_i^{'}$ can be expressed as a linear combination of u_i and $\bar{u}_i$:

$$u_i^{'} = cu_i + s\bar{u}_i \qquad c, s \in \mathbb{R} \, . \tag{38}$$

It is possible to demonstrate that $c = cos(\varphi_h)$ and $s = -sin(\varphi_h)$, where φ_h is the generic rotation needed to obtain vector $u_i^{'}$ starting from u_i

and it can be expressed as:

$$\varphi_h = \pm \frac{2\pi}{N} h \,. \tag{39}$$

The angle φ_h is called *inter-blade phase angle* (*IBPA*) and the parameter h represents the number of *nodal diameters* of a mode shape, i.e. the number of nodal lines crossing the center of the structure along which the displacements are null. The following relation holds:

$$0 \leq h \leq \tilde{h} \qquad \tilde{h} = \begin{cases} \frac{N}{2} & if\ N\ is\ even \\ \frac{N-1}{2} & if\ N\ is\ odd \end{cases} . \tag{40}$$

According to Equation (38), every linear combination of standing modes falling in the class (3) still satisfys the eigenproblem in Equation (32). However, valid solutions of the eigenproblem are also represented by the following complex vectors:

$$z_i = u_i + j\bar{u}_i \qquad \bar{z}_i = u_i - j\bar{u}_i \,. \tag{41}$$

Therefore, in general, is it possible to have real and complex eigenvectors, that differ in that for real eigenvectors all the DOFs pulsate without any relative delay between them, while for complex eigenvectors the same instantaneous spatial configuration appears rotated of one sector after an interval of time $t = \varphi_h/\omega$, ad showed in Figure 22. By recalling the concept of IBPA, it is possible to write the eigenvectors in a general form as:

$$z_i^{'} = z_i e^{i\varphi_h} \,. \tag{42}$$

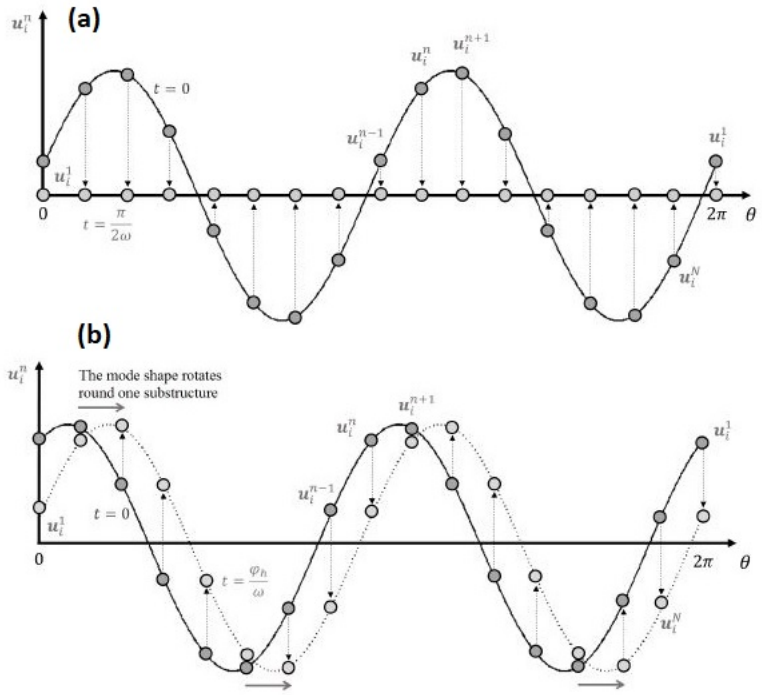

Figure 22: Schematic representation of a standing mode shape (a) and a rotating mode shape (b) of a cyclic symmetric structure.

4.3 Modal analysis

According to the approach firstly introduced by Mead, it is possible to express the vector containing the sector DOFs as follows:

$$x_s = \left\{ \begin{array}{c} x_l \\ x_i \\ x_r \end{array} \right\} , \tag{43}$$

where:

- x_l represents the DOFs at the left frontier of the fundamental sector;
- x_i represents the internal DOFs of the fundamental sector, i.e. those

not shared with the neighbor sectors;

- x_r represents the DOFs at the right frontier of the fundamental sector.

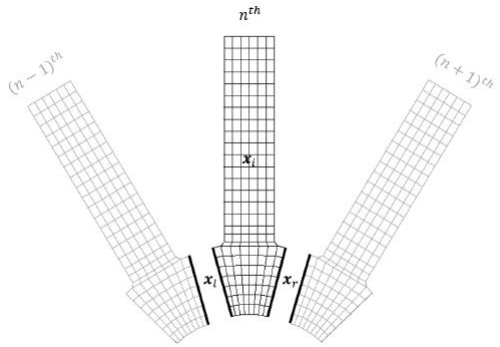

Figure 23: DOFs partition of the n^{th} fundamental sector.

It is possible to state that the number of DOFs at the left and at the right frontier is the same and that the DOFs at the right frontier of one sector can be seen as the left DOFs of the following sector. With reference to Equation (42), it is possible to express the right frontier nodes as a function of the left frontier nodes:

$$\{x_r\} = \{x_l\}\, e^{j\varphi_h} \quad \Longrightarrow \quad x_s = \left\{ \begin{array}{c} x_l \\ x_i \\ x_l e^{j\varphi_h} \end{array} \right\} . \tag{44}$$

Therefore, Mead's approach starts from the model of an isolated sector consisting of $n_l + n_i + n_r$ DOFs and leads to a reduced model with $n_l + n_i$ DOFs. In other words, by varying the value of φ_h it is possible to evaluate the dynamic behavior of the whole structure starting from the matrices of isolated sectors, thus making the whole modal analysis more simple and less time-consuming.

4.4 Bladed-disc dynamics

The dynamics of a bladed disc can be synthesized by mean of the *FreND diagram*, which represents the plot of the natural frequencies versus the number of nodal diameters characterizing the associated mode shapes.

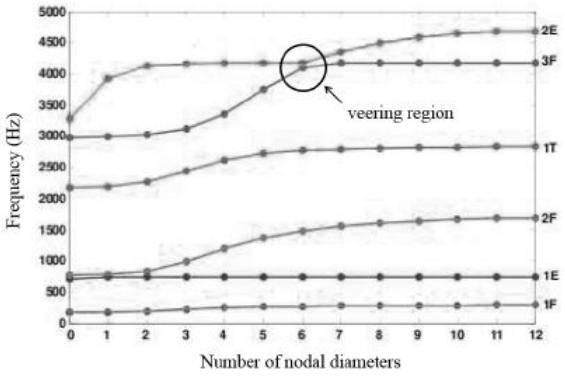

Figure 24: Example of a FreND diagram for a bladed disc.

As shown in Equation (42), each modal family is represented by a line connecting modes from $h = 0$ to $\tilde{h}$ and modes having the same sector deformed shape (i.e. 1F-2F, 1T-2T, ...) are grouped into distinct families. In most cases, the curves starts with a parabolic trend, which denotes that disc dominated mode shapes: for low values of h, the blades are dragged by the discs during vibration. As the number of nodal diameters increases, the disc becomes stiffer and the natural frequencies increases, until the curves for each modal family asymptotically approach one natural frequency, which corresponds to that of the clamped, blade-alone configuration. Therefore, the quasi-horizontal curves represent blade-dominated vibration modes, where the disc can be considered nearly motionless and the blades are weakly coupled among themselves. Another characteristic is the presence of veering regions, as the one that can be observed in Figure 24, which occur when two different families get close to each other and that are symptomatic of large vibration amplitudes due to mistuning phenomena [13].

As mentioned before, the mode shapes can be divided into two main families: *system modes* (i.e. displacements involving also the disc) ad *airfoil modes* (i.e. displacements concentrated on the blade profile). For each of the two families, a further classification can be made:

- System modes:
    1. Edgewise: the tip of the blade moves in the direction of the turbine rotating axis (with respect to the hub).
    2. Flapwise: the tip of the blade moves in the tangential direction (with respect to the hub).
- Airfoil modes:
    1. Bending: the blade's nodes move in a plane perpendicular to the turbine axis; the hub and the tip of the blade are subjected to null displacement (clamped configuration), while the maximum displacement can be observed at midspan.
    2. Torsional: the blade's nodes twist around the blade's radial direction, with null displacement at the hub and the tip.

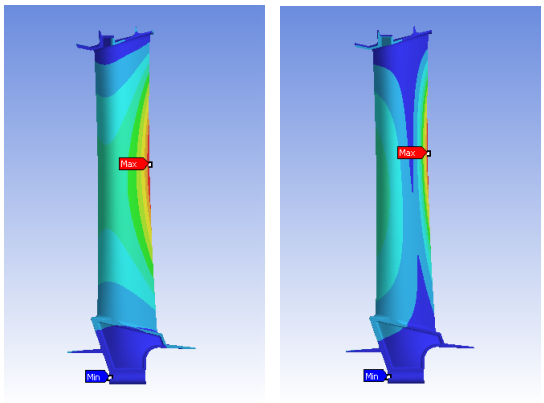

Figure 25: Example of bending (left) and torsional (right) modes.

The natural frequencies of a rotor-dynamical system often depend on the rotational speed, because of the effect of gyroscopic phenomena, and, in the case of gas turbine engines, of the stiffening induced by large centrifugal forces. The excitation frequency depends on the rotational speed as well: most of the dynamic excitations (with the exception of mechanical impacts and self-excited phenomena) induce *synchronous vibrations*. This means that their excitation frequency ω depends on the rotor angular velocity Ω according to the following relationship:

$$\omega = EO \cdot \frac{\Omega}{2\pi}\,, \tag{45}$$

where $[\omega] = Hz$, $[\Omega] = rpm$ and the coefficient EO, which stands for *Engine Order*, denotes the periodicity of the excitation over the bladed disc. For instance, if the excitation is caused by the previous stator wakes, EO represents the number of stator vanes.

In order to study the forced response of a bladed disc, *Campbell's Diagram* is commonly used (Figure 26). In the diagram, the natural frequencies are represented as a set of lines which trend depends on the rotation speed, while the EO excitation frequencies are represented by straight lines starting from the axes origin.

The intersections between the two sets of line represent possible resonances. In must be pointed out that, among all the crossings, just few of them are representative of an actual resonance condition. The critical intersections are those for which the following relation holds:

$$EO = z \cdot N \pm h \qquad \forall z \in \mathbb{N}\,. \tag{46}$$

For $z = 0$ the EO equals the number of nodal diameters h of the mode shape. What happens in this case is that the force distribution over the structure exactly match the shape of the mode and, therefore, when the excitation frequency equals the natural frequency of the mode shape, the maximum

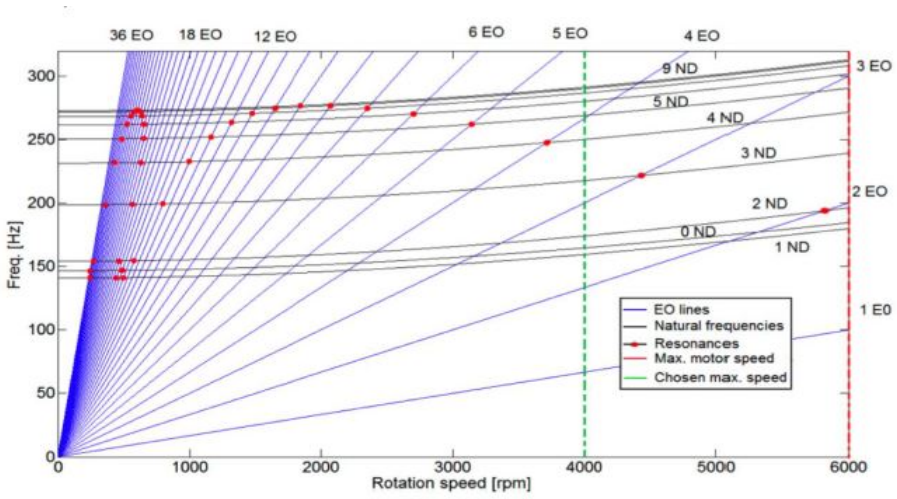

Figure 26: Example of Campbell's Diagram.

response amplification is obtained. On the contrary, given a certain EO, mode shapes such that $h \neq EO$ cannot be excited in resonance condition because the force projection onto the mode, i.e. the modal force, is null. On the other hand, when $z \neq 0$ a mode with h nodal diameters is critically excited due to the *aliasing phenomenon*: as the rotor blades do not represent a continuous system but a discrete one, they sample the forcing term with a finite number of points and this allows the disc to perceive the force as it had $EO = h$. As shown in Figure 27, the wave representing the EO=24 is seen by the row of blades as a wave characterized by *EO=8*, so the wave is able to excite in resonance condition a mode shape with *h=8*.

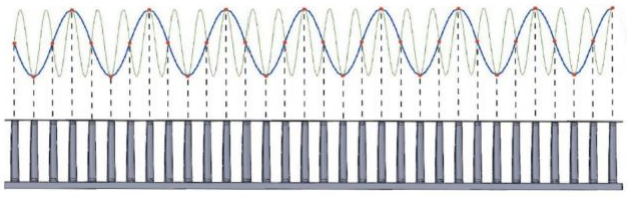

Figure 27: Example of aliasing: a forcing term with EO=24 excites in resonance condition a mode shape with h=8 nodal diameters.

4.5 Aeromechanical instabilities

Besides resonances, mentioned in 4.4, other phenomena that must be taken into account when considering a turbine rotor are aeromechanical instabilities. Among these, *flutter* plays an important role; it occurs when, following an initial structure displacement, the fluid enhances the vibration and this increment in amplitude may lead to structure rupture long before than the classical fatigue analysis prediction. The discipline that studies the interaction between the modal behavior of a structure and the fluid flow is called *Aeroelasticity*. In order to understand its field of interest and its interaction with other relevant disciplines, it is useful to give a look to the *Collar Diagram*, also known as *Collar Triangle*.

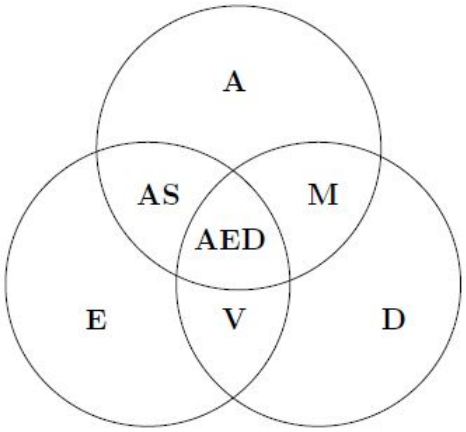

Figure 28: Collar Diagram.

A	Aerodynamics
E	Elasticity
D	Dynamics
AS	Static Aeroelasticity
V	Vibration Mechanics
M	Mechanics of Flight
AED	Dynamic Aeroelasticity

Table 1: Collar Diagram's legend.

As it can be observed in 4.4, a first classification of aeroelastic phenomena can be made as follows:

1. Static aeroelastic phenomena, that do not take into account inertial loads;

2. Dynamic aeroelastic phenomena, that take into account inertial loads.

In both categories it is possible to identify a further classification:

1. Aeroelastic stability, that do not consider external loads;

2. Aeroelastic response, that takes into account external forces.

The flutter phenomenon falls in the subcategory of dynamic aeroelastic stability problem. Its origin may be related to the detachment of the fluid flow from the airfoil or to the detachment of the wake vortex from the LE, which both cause auto-excited vibrations. In the first case *Stall Flutter* is observed, whereas in the second case, depending on the Reynolds number value, the phenomenon is denominated as *Vortex Shading*, *Galopping* or *Transonic buffering*. In turbine rotors usually only Stall Flutter is taken into account, as as the other types of flutter are not considered to be dangerous from a structural point of view. Stall Flutter is a complex phenomenon and it is possible to describe it according to various physical models; however, in the current report, only the *Classic Flutter semi-stationary model* will be considered.

4.5.1 Classic Flutter Model

The classic flutter model is based on the idea that, once the airfoil motion is known, it is possible to express the aerodynamic forces as functions of h, ϑ, I_h, I_ϑ, m_h and m_ϑ. As flutter takes place when the real part of the system's eigenvalue becomes null, the blade's motion can be assumed purely harmonic. It is possible to express the vector of the aerodynamic forces as:

$$\{F_a(t)\} = M_a \{\ddot{x}\} + C_a \{\dot{x}\} + K_a \{x\} \ , \tag{47}$$

where the vector $\{x\}$ contains the coordinates h and ϑ (represented in Figure 29) and the matrices M_a, C_a and K_a represent, respectively, the aerodynamic inertia, the aerodynamic damping and the aerodynamic stiffness of the system. The governing equation for a generic multiple DOF system can be written as:

$$M \{\ddot{x}\} + C \{\dot{x}\} + K \{x\} = \{F_m(t)\} + \{F_a(t)\} \ . \tag{48}$$

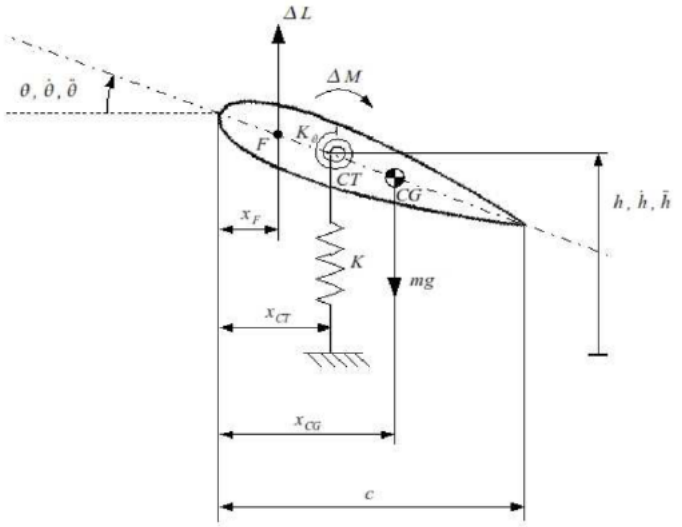

Figure 29: Example of an airfoil section with 2 DOFs.

By making the hypothesis that all the external loads that are not of aerodynamic nature can be neglected ($\{F_m(t)\} = 0$) and by replacing the aerodynamic forces vector with the expression in Equation (47), the following equation can be obtained:

$$(M - M_a)\{\ddot{x}\} + (C - C_a)\{\dot{x}\} + (K - K_a)\{x\} = 0\,. \tag{49}$$

The latter expression represents a homogeneous equation which general solution can be written as follows:

$$\{x(t)\} = \{\bar{x}_k\}\, e^{\nu_k t}\,, \tag{50}$$

where ν represents the eigenvalue and it is a complex number:

$$\nu_k = \Gamma_k \pm i\Omega_k\,, \tag{51}$$

where $k = 1, 2, ..., n_c$ and n_c is the number of complex conjugated solutions. The parameters Γ_k and Ω_k represent, respectively, the modal damping and the modal frequency and the following relations hold:

- $\Gamma_k > 0$: the vibration is aerodynamically damped, which means that no aeroelastic instability occurs.
- $\Gamma_k = 0$: the vibration is aerodynamically sustained, meaning that an instability condition is set.
- $\Gamma_k < 0$: any vibration is aerodynamically amplified, hence the fluid enhances the vibration amplitude up to the point when the structure collapses.
- $\Omega_k = 0$: the motion is time invariant.
- $\Omega_k \neq 0$: the motion is harmonic.

4.5.2 Flutter in turbomachines

It is possible to extend the considerations applied for the single airfoil profile with 2 DOFs to the whole rotor row. In this case, interaction among blades must be taken into account; as a consequence, a disturbance on one blade will not only change the conditions of the flow that surrounds it but it will move around the rotor and affect the neighboring blades. This phenomenon is known as *aerodynamic coupling* and it is showed in Figure 30. A further interaction takes place between rotor and stator; the latter is responsible of the correct direction of the flow entering the rotor; the angle of incidence, together with the flow's velocity and the blade's mode shapes, will play a crucial role in the possible occurrence of flutter.

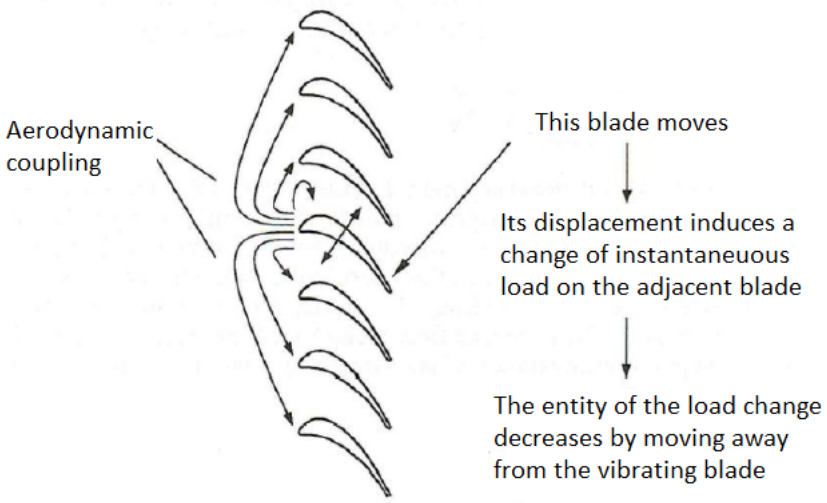

Figure 30: Aerodynamic coupling on a blade row.

Among all the parameters that can influence the aeroelastic vibrations of a bladed discs, A.V. Srinivasan identified twenty of them [14]. The most important ones are listed in the following:

- Shroud: the contact between adjacent blades shrouds introduces a cer-

tain damping (induced by friction forces) in the system's equation of motion, so it modifies the modal shapes and loads at the interface.

- Shock waves: they strongly influence the pressure load at the blade's leading edge.

- Inlet and outlet conditions: pressure and temperature depends on the flow's density and affect the aerodynamic damping.

- Reduced frequency: it is defined as the ratio between the time a particle takes to cross the airfoil semi-chord and the time needed for the aerodynamic profile to complete a full vibration cycle. In mathamatical terms:

$$k = \frac{c\omega}{2V} \,. \tag{52}$$

  When the reduced frequency k is low, the flow is considered quasi-static, while for high values of k it is considered unsteady.

- IBPA: the inter-blade phase angle, already mentioned in 4.2, is the angle that represents the phase shift between adjacent blades during their vibration; it defines the characteristics of the coupling among the blades.

- Mistuning: it is the variation in mass and/or stiffness among blades, that can be introduced on purpose, in order to modify the aerodynamic coupling, thus reaching flutter stability.

The analysis of flutter stability requires the preliminary study of the interaction among blades, from both an aerodynamic and a structural point of view. The analysis makes use of a decoupled energetic approach, according to which the blades displacement is known and the fluid motion is to be solved by taking into account only of the impact of the blade's vibration on the flow itself.

In order to know the blade's displacement, a previous modal analysis is needed; it is based on the hypotesis that the influence of the gas flow on natural frequencies and modeshapes can be neglected. Once the displacements have been found, flutter is studied by applying a linear approach in the frequency domain. Under the assumption that inertial, geometrical and dissipative properties are the same for all the blades, each rotor sector vibrates similarly to the previous one, but with a constant phase shift (IBPA); therefore, in order to solve the flow field, non-stationary aerodynamic forces acting on the blade's surfaces are evaluated for different values of the IBPA.

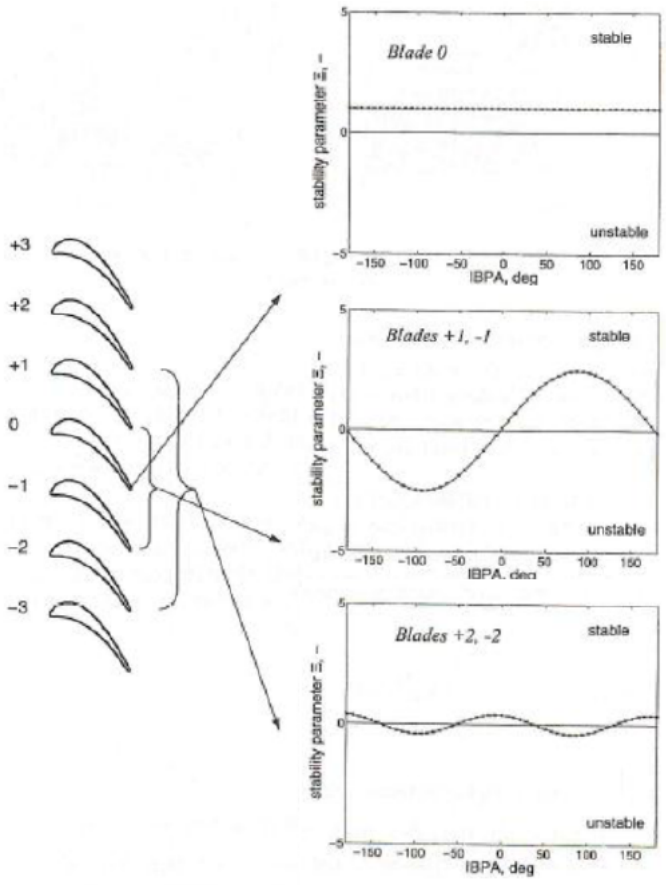

Figure 31: Influence of the adjacent blades on the reference blade flutter stability.

The occurrence of flutter instability can be identified thanks to the aerodynamic damping coefficient, which is related to the flow's work on the structure for a given frequency and modeshape. If this parameter has a negative value, this means that the structure is not able to dissipate energy and so it is instable from an aeroelastic point of view. In a row in which all the blades are vibrating, under the assumption of small obscillations, the system is linear and it is possible to apply the priciple of superposition: the overall displacement of a single blade can thus be obtained as a sum of displacements, each of which is linked to the motion of the other blades.

In order to have a better understanding of how blades influence each other vibrations, a look can be given to Figure 31. It is possible to observe that if a single obscillating blade is considered (blade 0), the aerodynamic damping is obviously constant with respect to the IBPA; however, flutter stability of the adjacent blades is influenced by the value of the IBPA and shows a sinusoidal trend. Moreover, the more the distance among the considered blades (i.e. blades with indices +2, -2) and the reference vibrating blade, the less is the influence of the aerodynamic damping.

After applying the superposition principle, the resulting aerodynamic damping coefficient varition versus the IBPA is commonly represented by the *S-curve*, also known as *Aeroplot*, showed in Figure 32. The plot allows to indentify flutter instability condition, occuring for negative values of aerodamping and flutter stability condition, occurring when the aerodamping is positive.

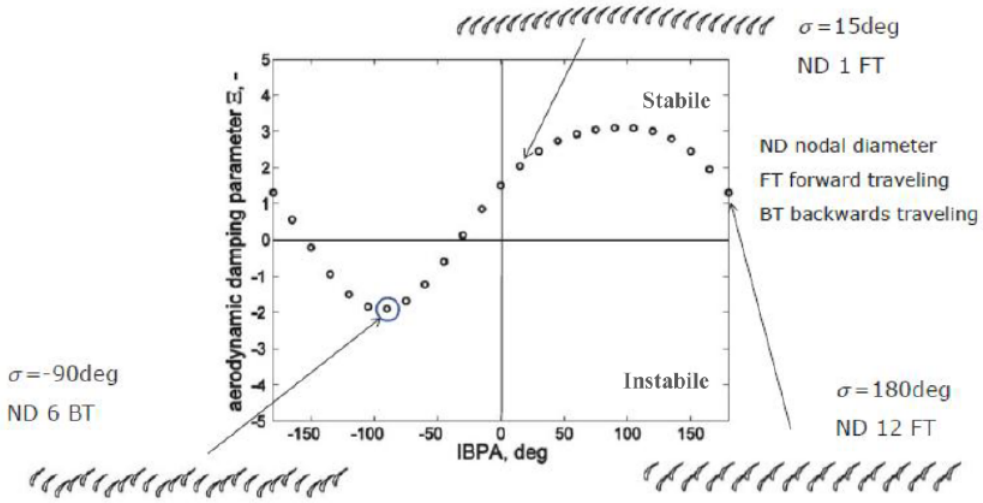

Figure 32: Example of Aeroplot.

5 CFD analysis

In order to establish wether a blade is subjected to aeromechanical instabilities (4.5), it is necessary to have as input data the results coming from the modal analysis (i.e. natural frequencies, mode shapes, etc.) and information about the flow field, in order to study how the aerodynamic forces interact with the blade vibration. The latter come from *Computational Fluid Dynamics* (CFD), which is a branch of fluid mechanics that uses numerical analysis and data structures to analyze and solve problems that involve fluid flows. The first step of the analysis process is the domain definition, followed by domain discretization (*meshing process*), which represents a critical step as the degree of refinement of the grid has a huge influence on the numerical simulation but at the same time it impacts computational costs. Besides, boundary conditions have to be accurately definied in order to give a correct representation of the physics of the problem.

A sfotware tool makes use of a mathematical model and a numerical method in order to analyze the fluid flow. Navier-Stokes equations are used for the mathematical definition of the problem; they represent a system of balance equations that describe the behaviour of a linear viscous flow.

5.1 Navier-Stokes equations

Navier-Stokes equations formulation is based on three hypotesis:

- the flow is continuous;
- the flow is homogeneous from a chimical point of view;
- the flow is free of electrical charge.

This system of equations represents the mathematical formulation of three main physical principles.

Conservation of mass (continuum equation) By considering a control volume with dimensions equal to δx, δy, δz and a compressible fluid of density ρ travelling through it, it can be stated that the mass variation in time is equal to the net flow mass through the walls of the control volume itself. The first term of the equation can be written under the assumption that the considered volume does not change in time:

$$\frac{\partial}{\partial t}(\rho \delta x \delta y \delta z) = \frac{\partial \rho}{\partial t} \delta x \delta y \delta z \,. \tag{53}$$

The second member of the equation can be written by applying the Taylor series expansion, in the following way:

$$-\frac{\partial(\rho u)}{\partial x} \delta x \delta y \delta z - \frac{\partial(\rho v)}{\partial x} \delta x \delta y \delta z - \frac{\partial(\rho w)}{\partial x} \delta x \delta y \delta z \,. \tag{54}$$

Therefore, the continuum equation can be written as:

$$\frac{\partial \rho}{\partial t} + \frac{\partial(\rho u)}{\partial x} + \frac{\partial(\rho v)}{\partial x} + \frac{\partial(\rho w)}{\partial x} = 0 \,, \tag{55}$$

which can be also rewritten in a more compact form as follows:

$$\frac{\partial \rho}{\partial t} + div(\rho \underline{u}) = 0 \,. \tag{56}$$

The first term represents the density time variation, while the second term is known as *convective term*, as it represents the net flow mass through the considered domain.

Momentum conservation equation Newton's Second Law states that the momentum variation of a particle depends on the resultant of the forces applied on it. Forces can be classified in two categories: surface forces (viscous forces and pressure) and volume forces (gravitational force, centrifgual force, etc.). In the following, force components that generate stress in the fluid elements will be considered separetely from all the other forces (grouped

together in a term representing the overall momentum variation sources). In particular, stress components can be further classified in normal stresses (p) and viscous stresses (τ_{ij}). Therefore, the momentum conservation equations along the three space directions can be written as:

$$\begin{array}{l} \frac{\partial(\rho u)}{\partial t} + div(\rho u \underline{u}) = \frac{\partial(-p+\tau_{xx})}{\partial x} + \frac{\partial \tau_{yx}}{\partial y} + \frac{\partial \tau_{zx}}{\partial z} + S_{Mx} \\ \frac{\partial(\rho v)}{\partial t} + div(\rho v \underline{u}) = \frac{\partial \tau_{xy}}{\partial x} + \frac{\partial(-p+\tau_{yy})}{\partial y} + \frac{\partial \tau_{zx}}{\partial z} + S_{My} \\ \frac{\partial(\rho w)}{\partial t} + div(\rho w \underline{u}) = \frac{\partial \tau_{xz}}{\partial x} + \frac{\partial \tau_{yz}}{\partial y} + \frac{\partial(-p+\tau_{zz})}{\partial z} + S_{Mz} \end{array} \quad , \tag{57}$$

that can be rewritten in a more compact form as:

$$\frac{\partial(\rho \underline{u})}{\partial t} + div(\rho \underline{u}\underline{u}) = div\left([\tau] - p[I]\right) + S_M \, . \tag{58}$$

For a Newtonian fluid, stresses can be expressed as functions of deformation (components s_{ij}); the latter can be classified in linear and volumetric deformation. With regard to linear deformation, by considering a cubic flow element it is possible to write elongation and shearing components respectevely as:

$$s_{xx} = \frac{\partial u}{\partial x} \, , \qquad s_{yy} = \frac{\partial v}{\partial y} \, , \qquad s_{zz} = \frac{\partial w}{\partial z} \, . \tag{59}$$

$$\begin{array}{l} s_{xy} = s_{yx} = \frac{1}{2}\left(\frac{\partial u}{\partial y} + \frac{\partial v}{\partial x}\right) \, , \\ s_{xz} = s_{zx} = \frac{1}{2}\left(\frac{\partial u}{\partial z} + \frac{\partial w}{\partial x}\right) \, , \\ s_{yz} = s_{zy} = \frac{1}{2}\left(\frac{\partial v}{\partial z} + \frac{\partial w}{\partial y}\right) \, . \end{array} \tag{60}$$

As regards the volumetric deformation, it is possible to write:

$$\frac{\partial u}{\partial x} + \frac{\partial v}{\partial y} + \frac{\partial w}{\partial z} = div \underline{u} \, . \tag{61}$$

By introducing the viscous constants μ and λ, it is finally possible to express tensions as:

$$\begin{aligned} \tau_{ii} &= 2\mu\frac{\partial u_i}{\partial i} + \lambda div\underline{u}\,, \\ \tau_{ij} = \tau_{ji} &= \mu\left(\frac{\partial u_i}{\partial j} + \frac{\partial u_j}{\partial i}\right)\,. \end{aligned} \tag{62}$$

Energy Conservation Law Ernergy Conservation Law states that the toal energy of a isolated system do not change with time. By recalling the First Law of Thermodynamics, it can be stated the the energy variation of a fluid particle equals the sum bewteen the net heat flux received by the particle and the work done on the particle itself. With regard to the heat related term, if a flow element with associated dimensions δx, δy, δz is considered, it is possible to write the conservation relations related to each of the six solid faces. By applying Taylor's expansion up to the second term, it is possible to write the net energy flux related to conductive heat exchange as:

$$-\left[\frac{\partial \dot{q}_x}{\partial x} + \frac{\partial \dot{q}_y}{\partial y} + \frac{\partial \dot{q}_z}{\partial z}\right](\delta x\delta y\delta z) = -[div\underline{\dot{q}}](\delta x\delta y\delta z)\,, \tag{63}$$

where $\dot{q}_x$, $\dot{q}_y$ and $\dot{q}_z$ represent the three component of the heat flux, that can be rewitten by applying the Fourier Law:

$$\dot{q}_i = -k\frac{\partial T}{\partial i} \quad \Rightarrow \quad \underline{\dot{q}} = -kgradT\,. \tag{64}$$

As regards the work contribute, as for the momentum equation the only forces that will be expressed in an explicit form are those associated with surface stress, namely pressure p and viscous tension τ_{ij}; all the other components will be taken into account as energy source terms. The work equation for unit of volume is:

$$\begin{aligned}
\frac{\dot{L}_x + \dot{L}_y + \dot{L}_z}{\delta x \delta y \delta z} &= [-div(p\underline{u})] + a + b + c\,, \\
a &= \frac{\partial(u\tau_{xx})}{\partial x} + \frac{\partial(u\tau_{yx})}{\partial y} + \frac{\partial(u\tau_{zx})}{\partial z}\,, \\
b &= \frac{\partial(v\tau_{xy})}{\partial x} + \frac{\partial(v\tau_{yy})}{\partial y} + \frac{\partial(v\tau_{zy})}{\partial z}\,, \\
c &= \frac{\partial(w\tau_{xz})}{\partial x} + \frac{\partial(w\tau_{yz})}{\partial y} + \frac{\partial(w\tau_{zz})}{\partial z}\,.
\end{aligned} \tag{65}$$

Therefore, by putting together the heat term and the work term, the final specific energy equation can be written as:

$$\frac{\partial(\rho E)}{\partial t} + div(\rho E\underline{u}) = [-div(p\underline{u})] + a + b + c + div(kgradT) + S_E\,. \tag{66}$$

The equations listed above show some similarities; it is therefore possible to rewrite them in a generic form by introducing the variable Θ, the diffusive coefficient Γ and the term S_θ that includes all the remaining terms:

$$\frac{\partial(\rho\Theta)}{\partial t} + div(\rho\Theta\underline{u}) = div(\Gamma grad\Theta) + S_\Theta\,. \tag{67}$$

The integration of *Partial Differential Equations* (*PDE*) is perfomed by means of the *Finite Volume Method*. It starts from Equation (67) and replace the generic variable, the diffusive contribute and the source terms with the different specific variables. The PDE thus obtained are then integrated on a tri-dimensional control volume CV that corresponds to the mesh cell; the conservation of the fluid properties is then imposed in every cell. For the generic variable Θ the integral form is:

$$\int_{CV} \frac{\partial(\rho\Theta)}{\partial t} dV + \int_{CV} div(\rho\Theta\underline{u}) dV = \int_{CV} div(\Gamma grad\Theta) dV + \int_{CV} S_\Theta dV\,. \tag{68}$$

5.2 Numerical resolution of governing equations: RANS approach

Navies-Stokes equations can not be solved in closed-form, except for some simple cases, so a numerical approach is needed in order to obtain a solution. However, if all the temporal and spatial scales of the studied phenomenon were considered, it would be necessary to employ *Direct Numerical Simulation* algorithms (DNS); the solving process would be very time expensive and incompatible with the time limitation typical of the engineering design process.

A more practical option is represented by the so-called *Reynolds Averaged Navier-Stokes* (RANS), which are derived from Navier-Stokes equations by mean of a time averaging procedure. Conceptually, this procedure is based on Reynolds decomposition, which provides for the generic varibale Θ decomposition into a mean setady value $\overline{\Theta}$ and a fluctuating component Θ':

$$\Theta = \overline{\Theta} + \Theta' \,. \tag{69}$$

This assumption can be considered true only if the flow is statistically steady or if the non-stationarity time scale is far greater than the time scale relative to the fluctuating component that is to be averaged.

By substitution of Equation (69) in Navier-Stokes equations, and by assuming that an incompressible fluid with constant viscosity is considered, the following equations can be obtained:

$$div(\underline{U}) = 0 \tag{70}$$

$$\frac{\partial(U_i)}{\partial t} + \rho div(U_i \underline{U}) = -\frac{\partial p}{\partial x_i} + D + \mu div(grad U_i) \,, \tag{71}$$

$$D = \frac{\partial(-\rho\overline{u_i' u_i'})}{\partial x_i} + \frac{\partial(-\rho\overline{u_i' u_j'})}{\partial x_j} + \frac{\partial(-\rho\overline{u_i' u_k'})}{\partial x_k} \,.$$

Some additional variables τ_{ij} are obtained; they are called *Reynolds additional stresses* and their presence is related to the non-linear nature of the equations. Turbulence models employed for RANS resolution are classified on the basis of the number of additional transport equations used to solve the new system featuring the additional variables; these latter can range from 1 to 7. Usually, the starting assumption is that of a correlation between main flow's deformation and and Reynolds stresses associated with the turbulent motion. From a mathematical point of view, these two values are linked by mean of the so-called *turbulent viscosity* μ_T, that can be written as:

$$\mu_T = \rho C \sigma l \,, \tag{72}$$

where C is a non-dimensional quantity while σ and l are respectevely the velocity and magnitude scales characteristic of large-scale vortices. The contribute of μ_T appers in the mathematical formulation of the relation bewtween turbulent stress and deformation proposed by the French mathematician Joseph Boussinesq in 1877:

$$\tau_{ij} = -\rho\overline{u_i' u_j'} = \mu_T \left(\frac{\partial U_i}{\partial x_j} + \frac{\partial U_j}{\partial x_i} \right) . \tag{73}$$

The RANS obtained with this mathematical procedure are discretized by diving the domain in small volumes, by mean of a computational grid named *mesh*.

5.2.1 Time discretization

The time discretized form of the RANS equations for a generic vectorial variable $\underline{\Theta}$ and for the generic cell of volume V can be written as:

$$V \frac{\delta \underline{\Theta}}{\delta t} + R(\underline{\Theta}) = 0 \,, \tag{74}$$

with $R(\underline{\Theta})$ being the term obtained by spatial discretization. There are two main methods to operate the time discretization: esplicit methods and implicit methods. Esplicit methods have the inconvenient of not being unconditionally stable, which means that the maximum dimension of the time steps depends on the dimension of the considered computational cell and on the velocity of perturbations travelling through the flow. Nevertheless, these kind of methods are largely employed in steady state solvers together with local time stepping techniques, which allow the use of different time steps for each of the grid's regions. For non-stationary problems, a same-time solution for the whole domain is required; therefore esplicit methods can not be used and the time stepping is fixed by the dimension of the smallest computational cells, which are usually those in the boundary layer. On the other hand, implicit methods feature time steps that are not limited by stability relations and can theoretically have any possible dimension. However, from a practial point of view, time step dimension must be compatible with the studied phenomenon's time scale. Even if these methods are more expensive from a computational point of view, they are largely employed in problems which required very elongated mesh, for instance in simulations with high values of Reynolds number.

5.3 CFD solver

In the study case considered in the present work, fluid dynamic analyses were performed by mean of a tridimensional, multistage, viscous *CFD Solver*. It solves the RANS equations (5.2), which are written in conservative form and are referred to a cylindrical coordinate system, plus the equation of state of gas. Spatial discretization is based on a cell model that enable to efficiently characterize the flow. It is possible to employ different kinds of three-dimensional grids, which can be used according to the physics of the problem that needs to be solved. One grid is usually dedicated to solving the steady state condition, for which lesser precision is required, while the other

is usually employed when dealing with non-linearities and unsteadiness.

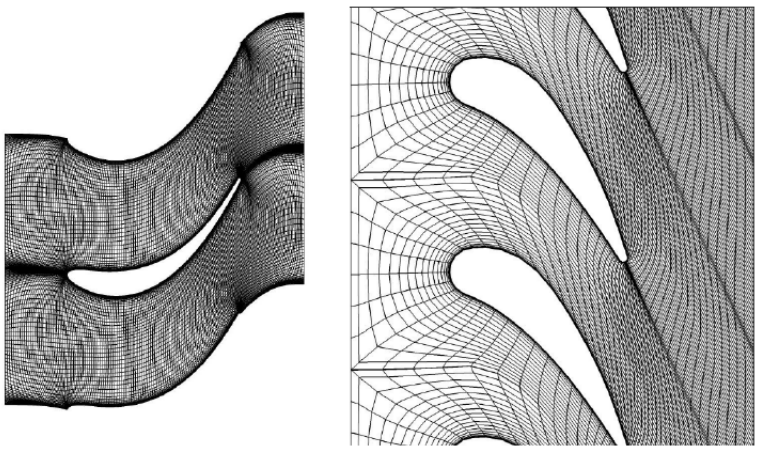

Figure 33: Example of different types of grid implemented by the CFD solver.

The *CFD Solver* can operate with both ideal and real gases, through the use of specific tables which contain gas properties. Different kinds of turbulence model can be used according to the complexity of the physics that needs to be addressed. The different levels of the turbulence model are linked to S-O-A assessment and may range from low level fidelity systems, such as Baldwin-Lomax, to higher level fidelity systems. Boundary conditions can be imposed in terms of:

- spanwise distributions of total pressure, total temperature and flow angles;
- temperature or heatflow and wall adhesion conditions;
- physical quantities conservation through the blades, in clearance regions.

The physical quantities involved in the analysis are usually made dimensionless by dividing them by a reference parameter that generally derives from

the physics of the problem that is addressed. Depending on the different turbomachinery involved, the reference quantity is adequately chosen. The outputs of the calculation include files which contain information about the geometry of the blades, the mesh parameters and the physical quantities through the turbine itself. In order to allow the mesh construction, the code needs some information about the blade's geometry, that are given through some input files:

- a file containing the coordinates of the blade's upper and lower side (Figure 34);

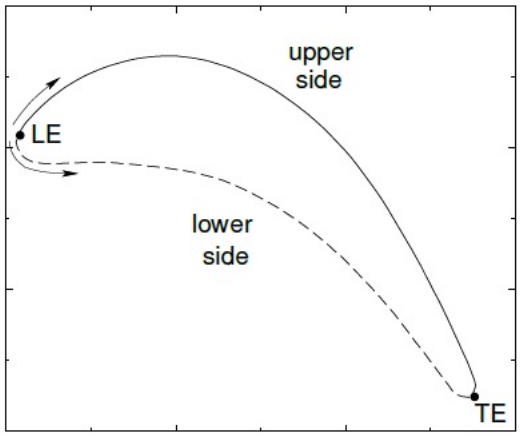

Figure 34: Airfoil geometry.

- a file containing the value fo the circumferential gap and the grid parameters used to define the position of the grid inlet and outlet boundaries and the shape of the grid.

- a file containing the coordinates of the boundary surfaces of the fluid flow (Figure 35).

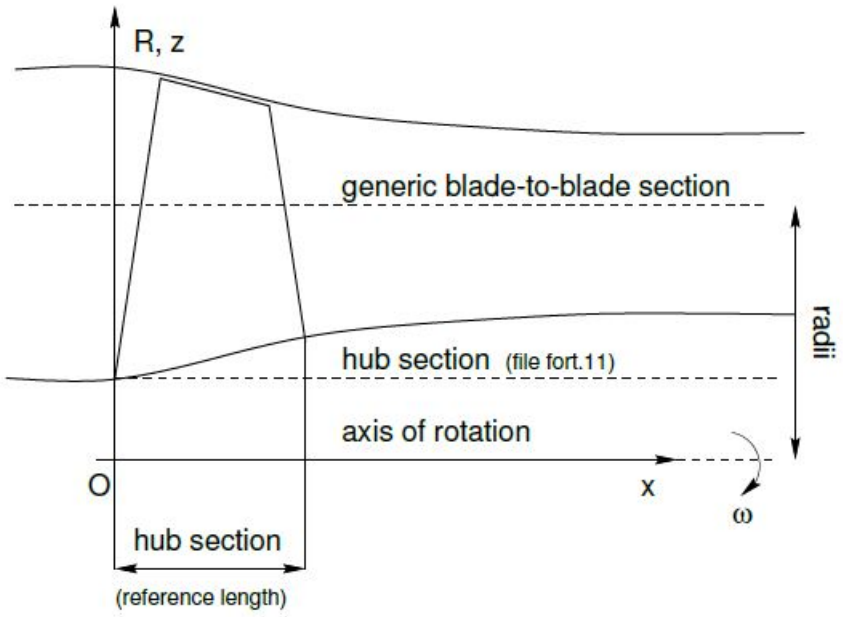

Figure 35: Meridional section of an axial turbomachine.

The grid generator has different releases depending on the grid that need to be generated (the differences between types of grid will be explained in 7.2).

6 Aeromechanical analysis

The design of a LPT is a complex process that requires inputs coming from both Aerodynamics and Structural Mechanics. Aerodynamics investigates how to maximize the conversion of the energy contained in the flow stream into mechanical power to be transmitted to the shaft; therefore, aerodynamic optimization is aimed at increasing turbine's efficiency. On the other hand, Structural Mechanics analyses are meant to guarantee the structural resistance, so that each component is able to bear static and dynamic forces which it is subjected to. The design phase starts with the generation of the CAD model. The blade's profile definition resulting from aerodynamic analyses is computed in hot condition, so it must be turned into cold condition first. In fact, blade's profile and length undergo the effect of thermal expansion in operative condition; this effects disappear if the turbine is not yet operating. After this step it is possible to move forward with the analysis, working on a suitable FE model that will allow to obtain displacements and stresses induced by the applied loads.

The first test on the model is the static pre-stressed analysis and at this point already, if the quality of the results is not satisfying, the blade will be subjected to a new process of modifications from the aerodynamic point of view. It is easy to understand that the time expenditure is a crucial issue of the design activity. Once the static analyses succeed in producing the desired results, the procedure moves forward to the dynamic analysis phase. Here, the model can present concerns about dynamic instability, which will require an increase in blade stiffness. This can be pursued by adding mass or constraints and, in both cases, the modification will lead to a disadvantage from the aerodynamic point of view. In fact, a unique optimization that considers all the existing aspects is not possible and that is the reason why the design process shows an iterative scheme.

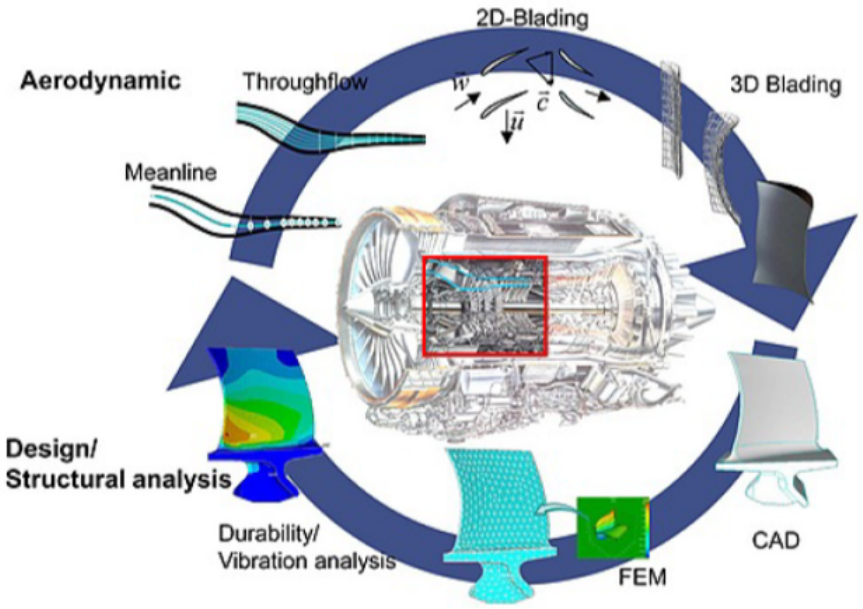

6.1 The aumotatic Aeromechanical Optimization Tool

The attempt to make the overall design process easier and faster led to the development of an automatic tool which is able to perform the Aeromechanical design. This means that the tool allows to take into account mechanical aspects already in the aerodynamic design phase, so that a trade-off between aerodynamic needs and structural requirements can be found at early design stages, thus reducing time and costs related to the design process. The main advantages of this automatic tool are synthetized in the following.

- Waste of time is drastically reduced; the traditional procedure is iterative while now the whole process is speed up by the autonomous model creation;
- User-friendly, due to a completely automated software which is easy to

use and customize;

- Feedbacks production and data collection radically assist the Aerodynamics team with information on the mechanical response;
- Results are easily readable due to the post-process dashboard.

The Tool is developed on Ansys Workbench base, which is a software that helps the design of automatic procedures. Moreover, it allows the display of multiple blocks, each with a specific type of analysis to be performed, namely static or dynamic. Figure 37 shows a simplified layout of the code workflow, in order to clarify the working steps.

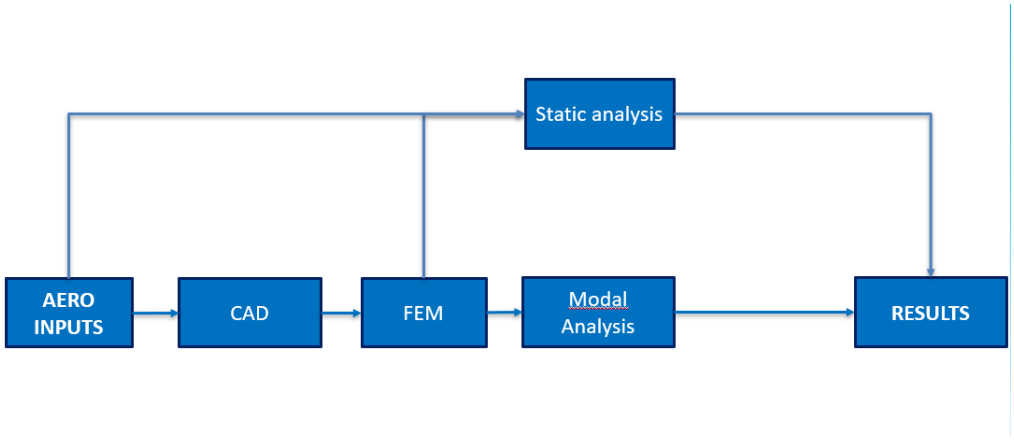

Figure 37: General workflow for the Aeromehcanical Optimization Tool.

1. CAD generation: using data from aerodynamic inputs, the *Tool* initially creates the 3D airfoil shape and then, by positioning the inner and outer templates, the ultimate CAD model.
2. FEM model: inside the analysis tool there is a code which generates FE model; the user selects the kind of analysis to launch thanks to an interface.

3. Static analysis: investigates the static deformations of the rotor, depending on the chosen boundary conditions and acting loads.

4. Modal analysis: FEM model is used to calculate natural frequencies of the body, which are data needed for flutter analysis and forced response. Even the Campbell diagram is plotted.

5. Flutter analysis: the stability of the solution is analyzed and plots showing aerodynamic damping are produced.

6. Post processing: a dashboard allows a simple and clear layout of the graphs and data collected during the whole process.

6.2 Aeroelastic Computation Tool

The *Aeroelastic Computation Tool* is a tool internally developed by GE Avio Aero in order to perform flutter analysis on LPTs, as part of the automatic *Aeromehcanicl Optimization Tool* discussed in 6.1. This kind of analysis considers the interaction between aerodynamic phenomena (previously studied through CFD analysis) and dynamic phenomena (previously investigated through FEM analysis). It can be easily understood how such analysis results utterly complex and expensive from a computational point of view: a model simplification is therefore needed. In order to do so, some assumptions need to be introduced. For instance, it is assumed that aeromechanical interaction occurs only at macroscopic scale with respect to the CFD turbulence level, and therefore only macroscopic physical characteristics are taken into account. Moreover, since only the macroscopic impact is evaluated, the grid used to study the phenomena will result in a coarser one with respect to the original grids from both CFD and FEM perspective, retaining only the degrees of freedom that are functional to the analysis; this procedure allows to lower computational costs and time. The *Aeroelastic Computation Tool* can be employed in the study of both simple and complex mode shapes;

the former occur, as described in 4.2, when the number of considered ND is different from both 0 and N/2, while the latter take place when the ND number is exactly 0 or N/2, thus configuring an in-phase and out of phase situation with respect to the two adjacent blades. The main output of the flutter computation is the so-called aerodamping (Figure 22), that is plot in function of the IBPA.

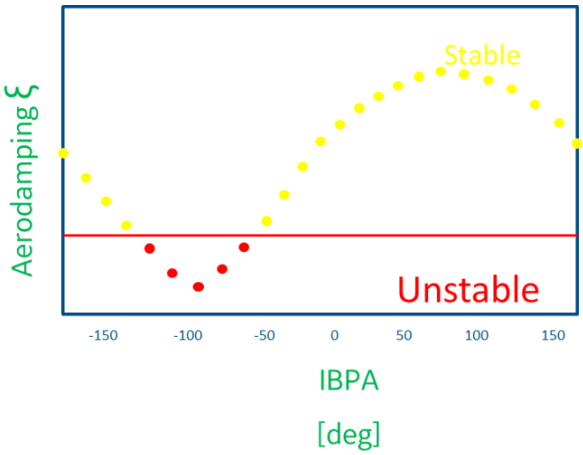

Figure 38: Schematic representationof Aerodamping versus IBPA.

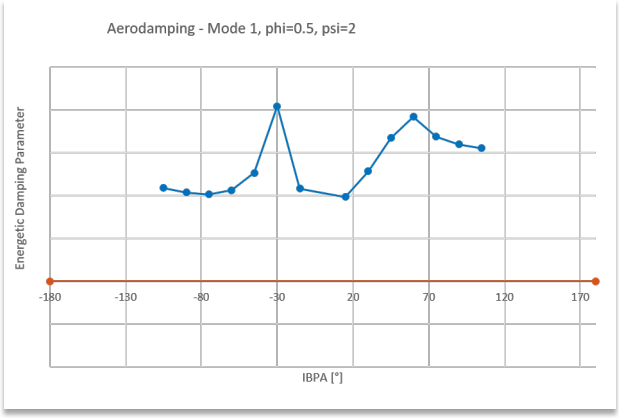

Figure 39: Example of Aerodamping chart for a stable mode.

When the aerodamping becomes negative, it is possible to conclude that the considered mode generates flutter instability on the examined blade. The *Tool* executes the aeroelastic analysis in three phases: pre-processing and post-processing are run locally, while the CFD computation and the flutter response computation are run on a High Power Computer (HPC), as their computational cost in rather high. A general workflow for flutter analysis is represented in Figure 40. Firstly, inputs from the aerodynamic calculation are needed. Once the needed information are extracted, the code proceeds with tha analysis of both the CFD domain and the FEM domain. Those domains are different by definition and need to be merged together prior to assess their reciprocal influence. There are lots of checks that are performed by the tool in order to verify that the inputs have been correctly assigned for each different physical characteristic of the flow and of the blade or vane geometry. All of those checks have been implemented in order to increase the robustness of the code and avoid errors during this complex process.

After this step, the actual flutter calculation can be performed. This requires input files from the dynamic analysis as well. Among them:

- a file containing information about the mesh structure;
- a bunch of characteristic files of the examined vibration modes.

Besides, some data required for the correct *Tool* functioning need to be inserted. At this point the extraction of the aerodamping values for the considered modes is performed on the HPC and the aerodamping plots are obtained; they show if the blade is stable or not from an aeroelastic point of view. If the blade proves to be unstable, design intervention is required in order to eliminate or at least reduce flutter instability, so that the phenomenon becomes non-destructive.

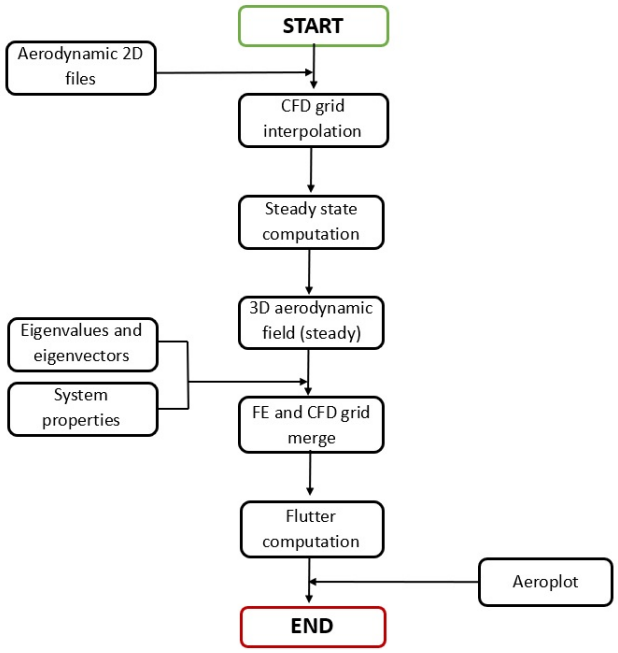

Figure 40: General workflow for the *Aeroelastic Computation Tool*.

7 Converter Tool Development

As seen in 5.3and Section §6, the *Aeroelastic Computation Tool* requires as CFD inputs those data given as outputs by the *CFD Solver*, which makes use of a CFD mesh in order to perform the volume discretization. Usually CFD solvers use millions of Degrees of Freedom (DOF) in order to reach sufficient accuracy in the domain discretization; this is mainly due to the dimensional scale of the physical phenomena that Aerodynamics is dealing with and needs to accurately capture in order to determine the overall engine performance. On the other hand, Aeromechanics is much more focused on the macroscale interaction between the aerodynamic forces and the airfoil dynamic response. This allows to potentially reduce the grid domain discretization and therefore the DOF involved. Reducing DOF of both aero and dynamic domain is crucial in order to produce aeromechanical results that are fast enough to

support the design phase. Therefore, a converter tool has been developed with the double purpose of dealing with different types of grid that are usually employed inside Aerodynamics domains (H-type grid, OH-type grid, C-type grid etc...) and to greatly reduce the number of DOF by using a coarser mesh.

7.1 Converter Tool genesis: motivation and specifications

The *Converter Tool* has been enterely developed on Matlab and it is able to access the data contained in standard CFD codes such as mesh discretization, boundary condition, flow functions, etc. The code runs in batch mode, so that the whole procedure is automatic and the user is only required to insert few keyboard inputs as the number of turbine's stages and the number of span sections to consider in order to evaluate the blade's geometry and to build the 3D mesh.

The grid conversion part has been the most critical aspect to deal with, as converting a structured mesh into an unstructured one required the extraction of specific geometry parameters that are needed to rebuilt a coarser mesh; on the other hand, it has also been necessary to find an automatic way to set the new structured grid parameters automatically, without the user interaction. This phase involved a raw statistical analysis of the parameters that had been used for a certain number of previously studied LPTs, in order to find some correlation that could be employed to built a mesh that was coarser enough to allow fast aermoechanical analysis, guaranteeing at the same time a good mesh quality, so that the required precision on macroscale phenomena can be obtained.

As previously anticipated, one of the main target to be reached through the *Converter Tool* development was to create a completely automatic procedure that required no user interaction and that could be integrated with the automatic *Aeromechanical Optimization Tool* (6.1).

7.2 Structured and unstructured grids

Grids can be classified into two main categories: structured and unstructured grids. In structured grid generation, grids are built in the solution domain in such a way that grid points can be considered as the points of intersection of curvilinear-coordinate curves (in two dimensions) or surfaces (in three dimensions). Therefore, the way in which grid points are connected to each other (their *connectivity*) in the solution domain depends on the overall generation scheme used. For instance, in two dimensions a grid point can be specified by a couple of integers *(i,j)* and the neighbouring point will be *(i+1, j),* etc. (figure 41). As a consequence, the cartesian coordinates *x(i,j)*, *y(i,j)* of a point can be conveniently stored as the elements of matrices. However, during the last years methods of unstructed grid generation have been developed, first in structual and solid mechanics and then in computational fluid dynamics as well. In these type of grid the pattern of connections among grid points can vary from point to point; therefore, the connectivity of points must be described explicitly, by means of appropriate data structures. Due to this aspect, solution algorithms for partial differential equations using unstructured grids result more expensive than for structured grids. This cost increasment can be accepted when the solution domains consist of very complex geometries, as the higher geometric flexibility of unstructured grids (with respect to structured grids), can lead to an improvement of the overall solution accuracy. Moreover, unstructured grids use has been found convenient when employed in the numerical solution of transient flows or moving boundary problems.

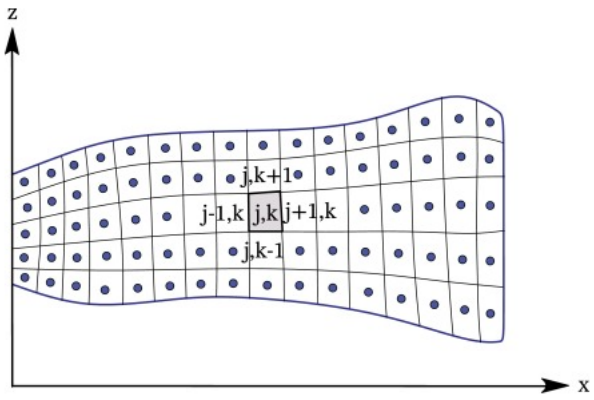

Figure 41: Example of structured grid [36].

Therefore, the mean difference between structured and unstrucured grid is that the former is identified by regular connectivity and the latter by irregular connectivity; moreover, while the possible element choices for structured grids are quadrilateral in 2D and hexaedra in 3D, unstructured grids typically employ triangles in 2D and tethraedral in 3D. A third cathegory that can be found is hybrid grids, which contain both structured portions and unstructured portions. Typically, those parts of the geometry that are regular feature structured grids, while those that are complex have unstructured grids. These grids can be non-conformal, which means that grid lines do not need to match at block boundaries.

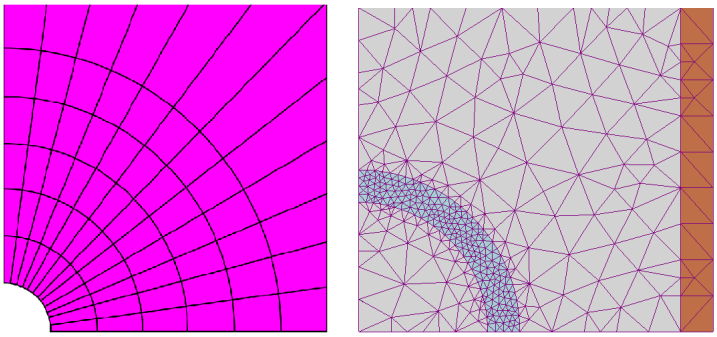

Figure 42: Structured (left) [37] and unstructured grid (right) [38].

Structured grids can be further classifid between C and H-type grids; for unstructured grids, instead, only the O-type will be considered. In C-type grids, the aerodynamic body is enclosed by one family of grid lines that start at the far-field, follow the wake, pass the trailing edge and, after wrapping around the body, continue in the far-field again. The other family of grid lines proceeds in the normal direction from the body and the wake. Therefore a "coordinate cut" is present in the grid, and it can be seen in Figure 43. This means that the segment a-b in the physical space is mapped onto two segments in the computational space and the upper part and the lower part of the cut are kept separately in the computer memory.

In the H-grid topology the aerodynamic body is described by two different grid lines and, on the contrary of C-grid, one family of grid lines closely follows the streamlines. Even though there is no evident coordinate cut, it should be pointed out that in turbomachinery the segments a-b and e-f are periodic to each other. A third cathegory of grids - which is not included in the previously mentioned grid generator - is the O-type grid. As can be seen in Figure 47, two families of grid lines are present; the first ($\eta = const$) forms close curves around the aerodynamic body, while the second family ($\xi = const$) is spanned in radial direction between the body and the outer boundary. The bounday line $\eta = 0$ represents the countour of the body (from a to a') and the coordinate cut is defined by the boundaries $\xi = 0$ (nodes $a - c$) and $\xi = 1$ (nodes $a' - c'$).

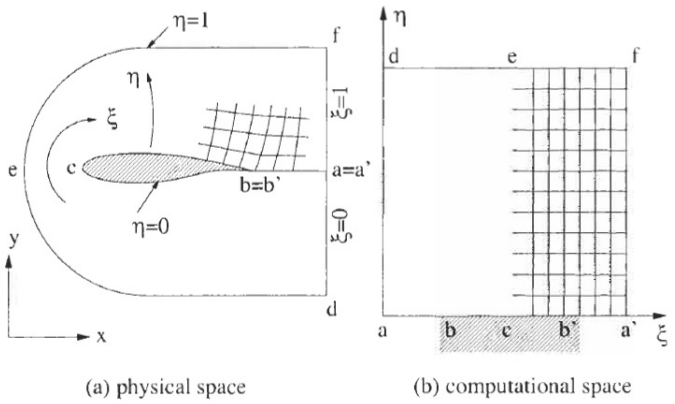

Figure 43: C-grid topology in 2D [4].

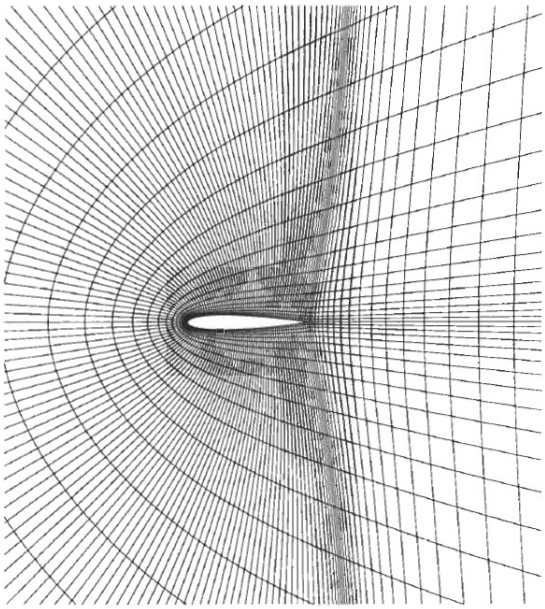

Figure 44: Partial view of a C-grid around NACA 0012 airfoil [4].

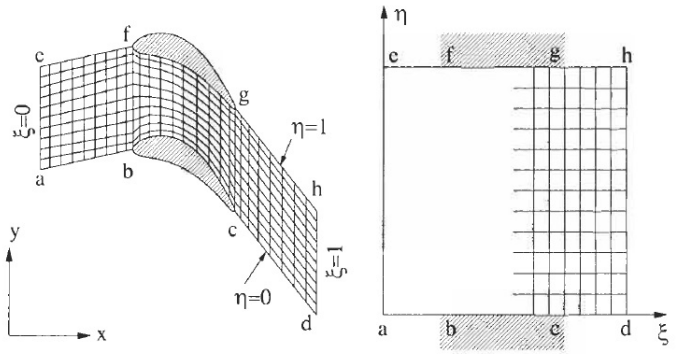

Figure 45: H-grid topology in 2D [4].

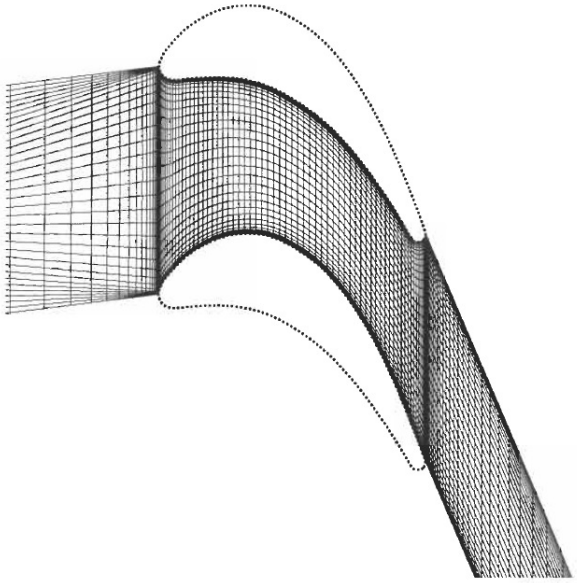

Figure 46: Partial view of an H-grid between turbine blades [4].

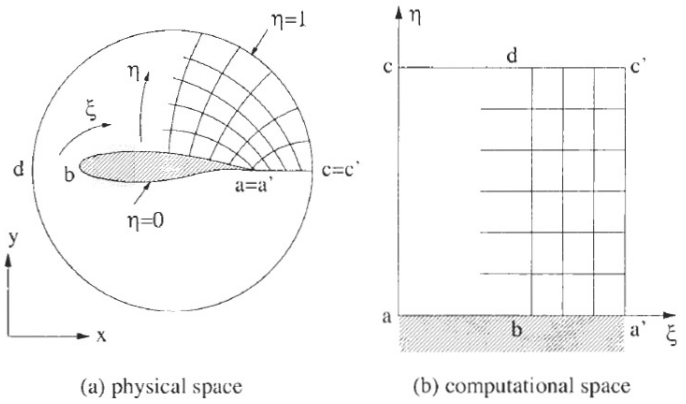

Figure 47: O-grid topology in 2D [4].

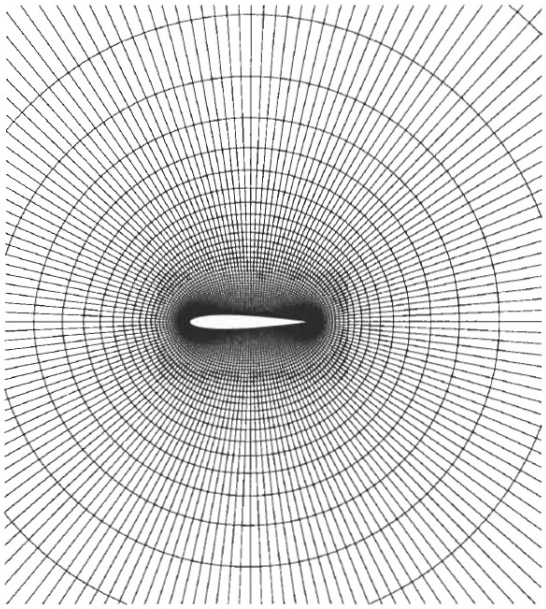

Figure 48: Partial view of an O-grid around NACA 0012 airfoil [4].

7.3 Grid conversion

In order to bluid the H-type geometry, the following information are needed:

- blade's section coordinates for different span values;
- coordinates of the plane to which the airfoil sections belong;
- mesh parameters.

As concerns the airfoil geometry, the coordinates have been obtained by the reference profile. Different sections at different spanwise locations can be generated depending on the refinement of the grid which is required. With regard to the mesh conversion, the needed parameters are summarized in Figure 49. The parameters are all made dimensionless in order to be compared with different other turbine types. In the following, the meaning of the different mesh parameters and the procedure employed to obtain them are described.

- The *inlet blade passage* represents the circumferential row distance between one blade profile and the adjacent one.
- The *outlet blade passage* is the the corresponding distance evaluated in the rear part of the stage; this dimension could be higher or lower than the inlet distance depending on the type of turbomachinery module analyzed.
- The *inlet flow* parameter represents the flow characteristic at the entrance of the row profile. Those are mainly influenced by the presence of an adjacent row.
- The *exit flow* parameter represents the exit condition of the flow after the row of interest; depending on the number of DOF it could be more or less representative of the actual wake condition.

- The *LE point* represents the first point of the row profile and the one in which the flow velocity reaches the zero value. This point is the one that marks the difference between the profile convex and concave side.
- The *TE point* represents the last point of the profile and the one from which the flow departs from the airfoil; it is also the wake start.
- *PS side definition and curvature* refers to all the series of points that describe the concave side of the profile where the flow decelerates and pression increases.
- *SS side definition and curvature* represents all the series of points that describe the convex side of the profile where the flow accelerates and pression decreases. Meshing both this area and the previous one is a delicate aspect, as they are the ones that tend to have the highest number of DOF involved; therefore, they need to be treated carefully in order to reduce the DOF and allow a quick aeromechanical assessment.

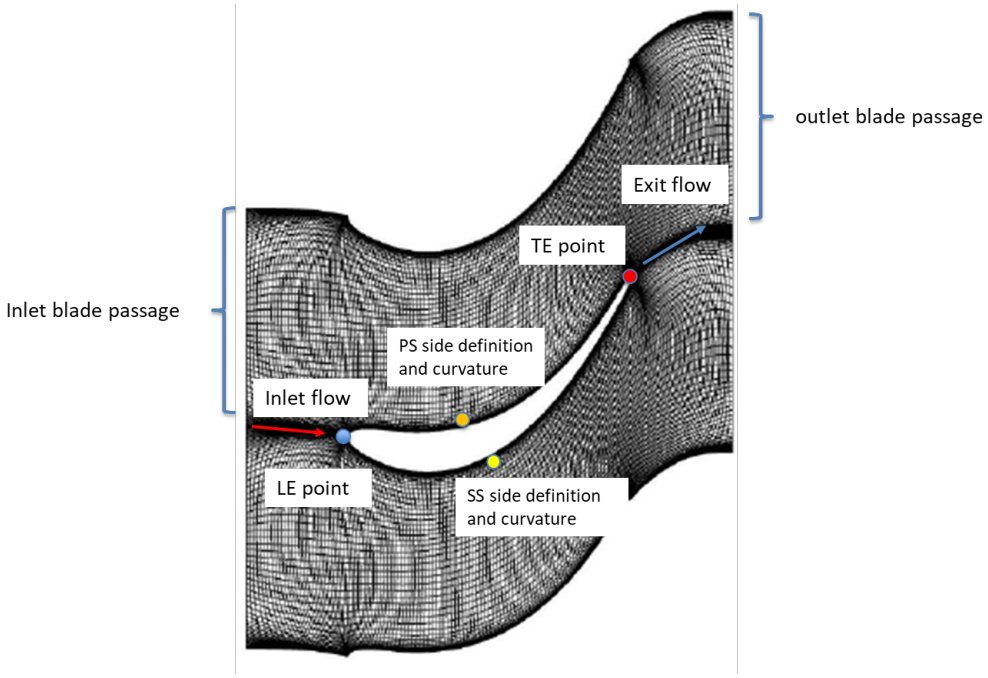

Figure 49: Main grid parameters needed for mesh conversion.

With regard to the C-type grid, the input parameters needed for the mesh creation are similar to those considered for the H-type grid and are omitted for sake of brevity. After the 2D grids have been generated, the code generates the 3D grids by stacking the different profile sections previously defined by the user. The higher the number of stacking sections, the finer the mesh and thus the higher the CPU computational effort needed to perform the aeromechanical analysis.

The input required for this phase are the followings:

- the direction of the stacking axes along which the code needs to create the full 3D grid;
- the previous generated 2D grid;
- the number of desired discretizations along the stack axes;

- the geometry of the hub and tip endwalls, as illustrated in Figure 50.

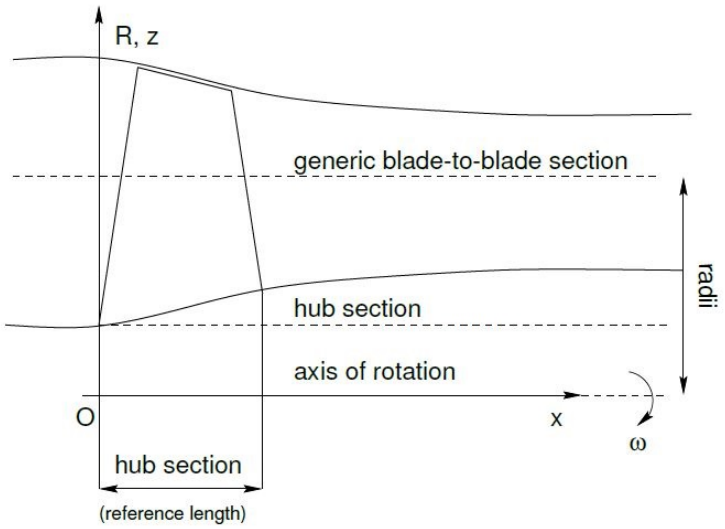

Figure 50: Schematic of the meridional section in an axial turbine.

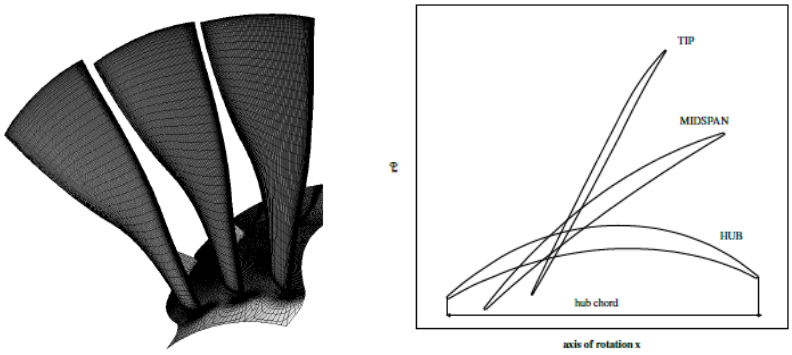

Figure 51: Example of a 3D grid (left) and different blade-to-blade sections from hub to tip (right).

8 Aeromechanical Optimization

In 3.5 and 3.6, it has been pointed out how the Smith Chart has a fundamental role in axial turbines concept design, as is allows to evaluate the fundamental characteristics of the single stages that form the turbine module. The principal parameters considered in the diagram are the *Stage Loading Faxtor* ψ and the *Flow Coefficient* ϕ; to these parameters are associated performance indicators in terms of stage efficiency and, in some versions of the diagram, deflection angle δ. Other fundamental parameters needed for a better definition of the stage performance are usually not taken into account; among them there are the *Reynolds Number*, the *Degree of Reaction* (R) and the profile *Aspect Ratio*, defined as the ratio of the blade's length to the mean axial chord ($AR = h/c$).

The aeromechanical optimization study conducted in this Thesis Project is aimed at providing a general vision on how the previously mentioned parameters influence the turbine's stage aeromechanical behaviour (in terms of flutter stability) and to confront them with a previous analysis conducted on the aerodynamic point of view (Reference [20]).

8.1 Results of the previous study

Typically, the *Concept Design* of a turbine module is performed by considering the flow at midpsan (*Meanline Analysis*). In order to get to the correct configuration, the designer has to optimize velocity triangles, flow path, solidity and chords with the aim of minimizing losses. Thanks to the evaluation of the flow at the meanline and by applying losses correlations (e.g. Craig & Cox and Ainley & Mathieson), it is possible to predict the axial turbine efficiency with good accuracy (1-2% [20]). The previous aerodynamic study ([20]) considered a reference turbine of fixed geometry which operative parameters were varied in order to make it work in a specifi point of the *Smith Chart*. The final aim was to obtain a series of additional in-

formation, usually not reported in the *Smith Chart*, which are found to be very useful in the *Concept Design* phase. For the considered configurations, corresponding blade models were obtained and CFD and CAE analyses have been conducted, in order to get a comparison with the data reported on the *Smith Chart* itself.

The analyses have been conducted by considering a constant value for the *Zweifel Coefficient,* $Zw = 1$, as it has been found that the optimal value in terms of efficiency falls in the range $0.9 \div 1.1$. With this assumption, it is possibile to prove that the number of airfoil profiles for a given row will depend on the deflection. In fact, under the assumption of incompressible and stationary flow, it is possibile to express the *Zweifel Coefficient* as:

$$Zw = 2\frac{s}{c_{ax}} \cos^2 \alpha_2 (\tan \alpha_1 + \tan \alpha_2) \,, \tag{75}$$

where:

- s is the row tangential step;
- c_{ax} is the flow axial velocity;
- α_1 is the flow inlet angle;
- α_2 is the flow exit angle.

With the hypotesis $Zw = const$ and constant axial chord, the following relation can be derived:

$$\frac{1}{s} \propto \cos^2 \alpha_2 (\tan \alpha_1 + \tan \alpha_2) \,, \tag{76}$$

which, once ψ has been fixed, proves a direct link between the number of airfoil profiles and the deflection.

With reference to Figure 52, it can be stated that, in general, the optimal chart areas from the aerodynamic point of view shows good results from the mehcanical side as well. Once that the main objective of the stage design has

been fixed, it is possible to choose the operating point on the *Smith Chart* in order to obtain the desired characteristics. It can be observed that the minimum stage's weight is obtained for low ψ and high ϕ values; however, if the whole turbine module is taken into account, low ψ values would result in a higher number of less-loaded stages, while higher ψ values would lead to a lower number of more-loaded stages. Therefore, the option with high ψ and high ϕ is the one that minimizes the overall module's weight.

As concerns the influence of the *Degree of Reaction*, the optimal aerodynamic performances are obtained with $R = 0.5$ and the same result is found also for the minimization of axial and tangential forces acting on the blade. However, in order to minimize the module's weight and to minimize the stress on both stator's vanes and rotor's blades, the best solution shows to be working with $R > 0.5$. In fact, being the blade's height condisered constant, the only paramter that influences the weight is the blade's area, which results to be proportional to the deflection; therefore, the row's weight will be proprortional to the deflection. As previously discussed in 3.6, an increasing of the *Degree of Reaction* will lead to:

- an increasement of the vanes weight, linked to the increasement in stator deflection;
- a decreasement in the blades weight, linked to the decreasment in rotor deflection.

As the weight variation in the rotor's blades will have a direct influence on the weight of the discs as well, in order to reduce the whole stage's weight it is more convenient to act a weight reduction on the rotor's blades, which implies working with $R > 0.5$.

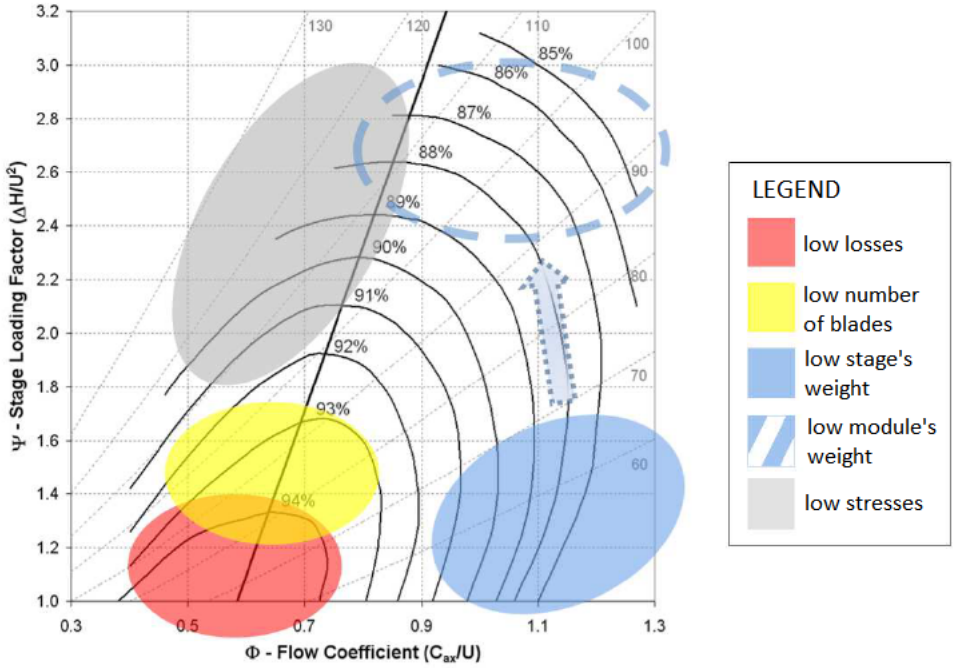

Figure 52: Smith Chart with a summary of aerodynamic and mechanical characteristics [20].

8.2 Case studies

According to the remarks made in 8.1, the study has been carried out by considering constant values of *Zweifel Ccoefficient* and *Degree of Reaction*, respectevely $Zw = 1$ and $R = 0.7$, and by varying the *Stage Loading Factor* ψ and the *Flow Coefficient* ϕ according to Table 2:

ϕ	0.5	0.7	0.7	0.7	0.8	0.8	0.9	1	1	1.1	1.2	1.3	1.3
ψ	2	1	1.7	2.2	1.4	2.8	1.9	1.1	2.4	1.6	2	1.1	2.5

Table 2: Values of Flow Coefficient and Stage Loading Factor considered in the case study.

The study was focused on the first and the second rotor of the LPT; in order to evaluate the flutter response, only the first two vibration modes have been considered, as they are the modes to which the major quantity of energy is associated. In the following, the Aerodamping plots resulting from the flutter analysis are reported. The blades of the first rotor and the second rotor will be respectevely referred to as *Blade 1* and *Blade 2*, while the considered vibration modes will be called *Mode 1* and *Mode 2*.

8.2.1 Case 1: ϕ=0.5, ψ=2

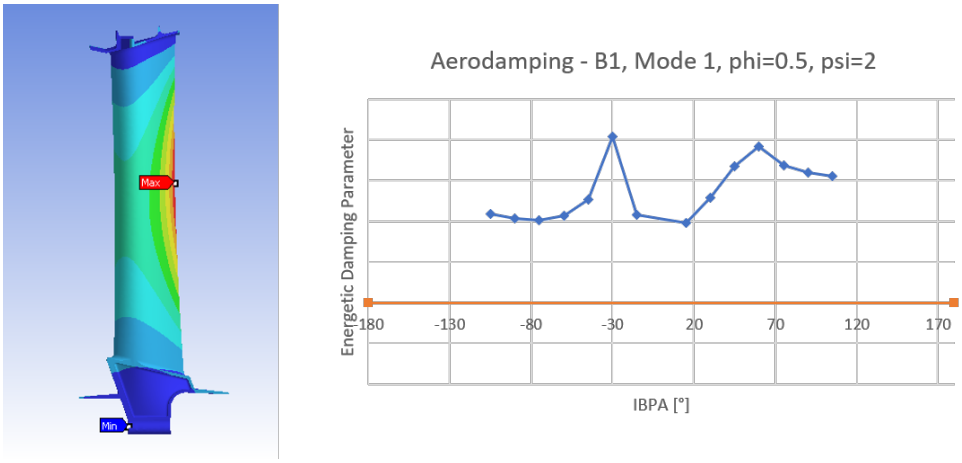

Figure 53: Case 1. Total deformation and Aeroplot for Blade 1, Mode 1.

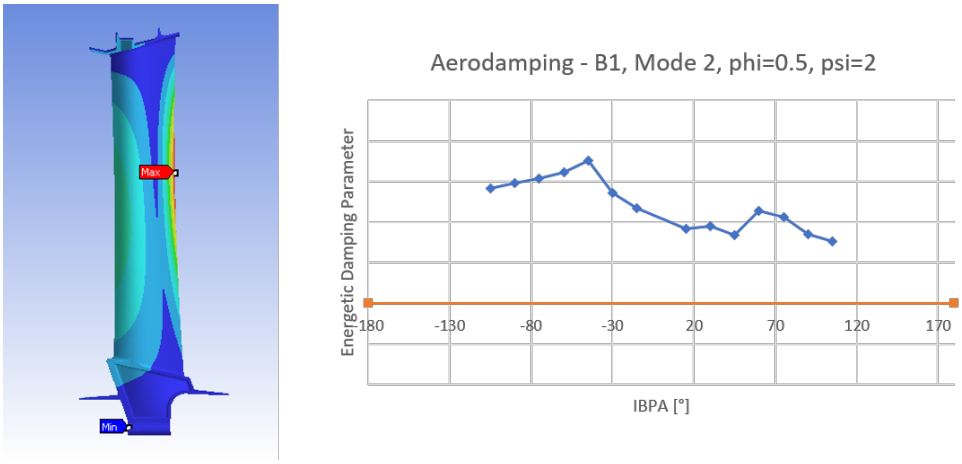

Figure 54: Case 1. Total deformation and Aeroplot for Blade 1, Mode 2.

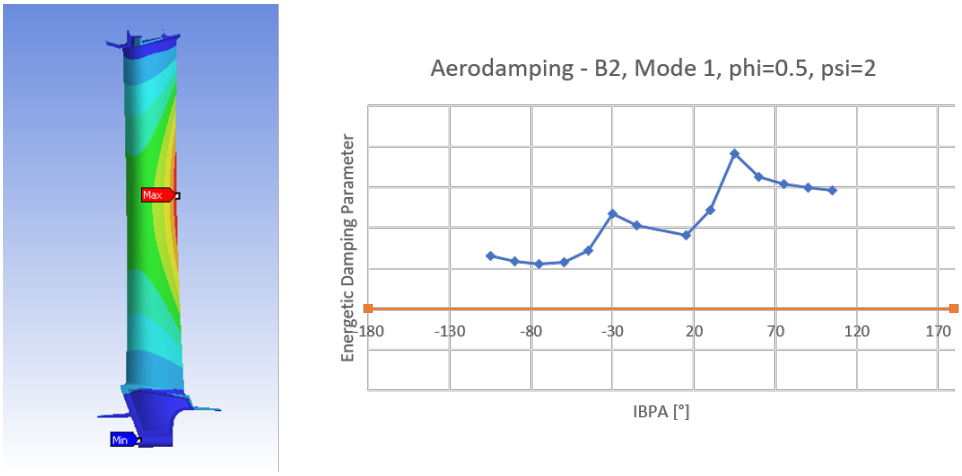

Figure 55: Case 1. Total deformation and Aeroplot for Blade 2, Mode 1.

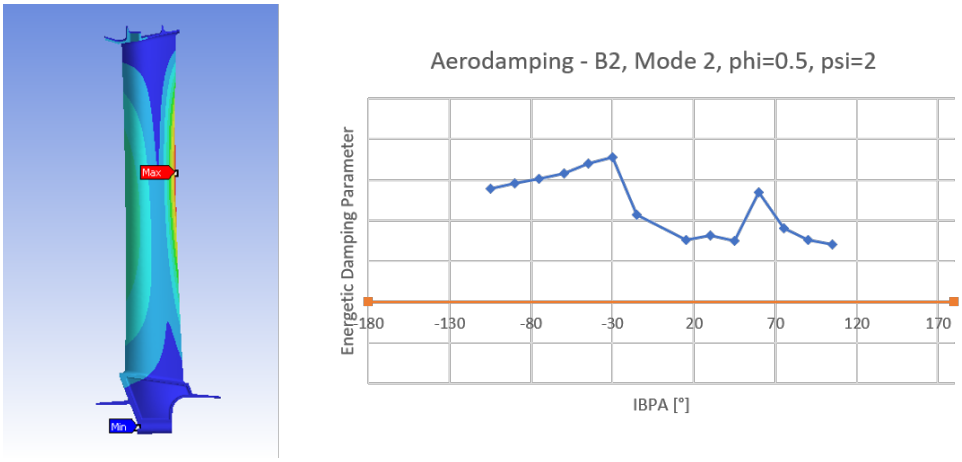

Figure 56: Case 1. Total deformation and Aeroplot for Blade 2, Mode 2.

In this case, both blades show aeromehcanical stability for both vibrating modes.

8.2.2 Case 2: ϕ=0.7, ψ=1

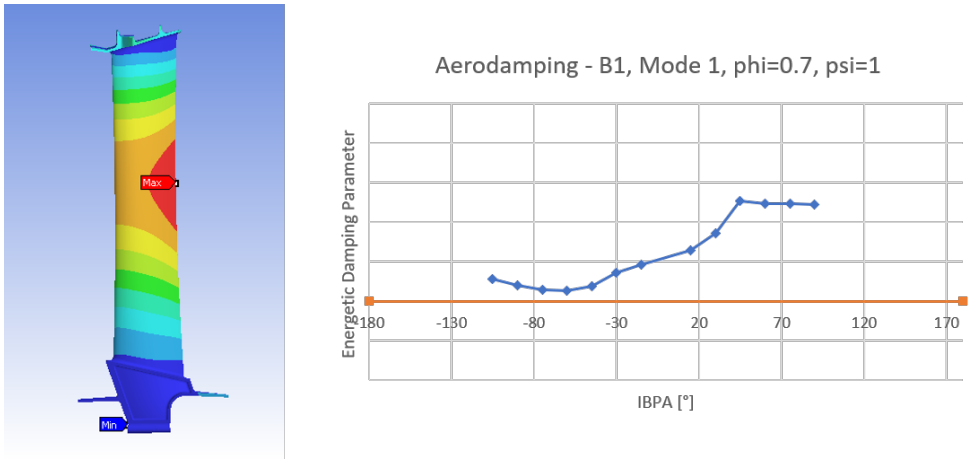

Figure 57: Case 2. Total deformation and Aeroplot for Blade 1, Mode 1.

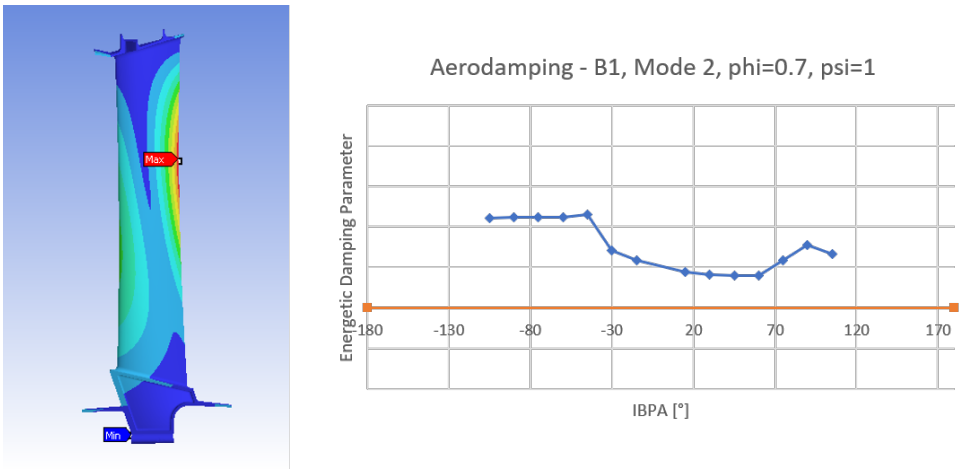

Figure 58: Case 2. Total deformation and Aeroplot for Blade 1, Mode 2.

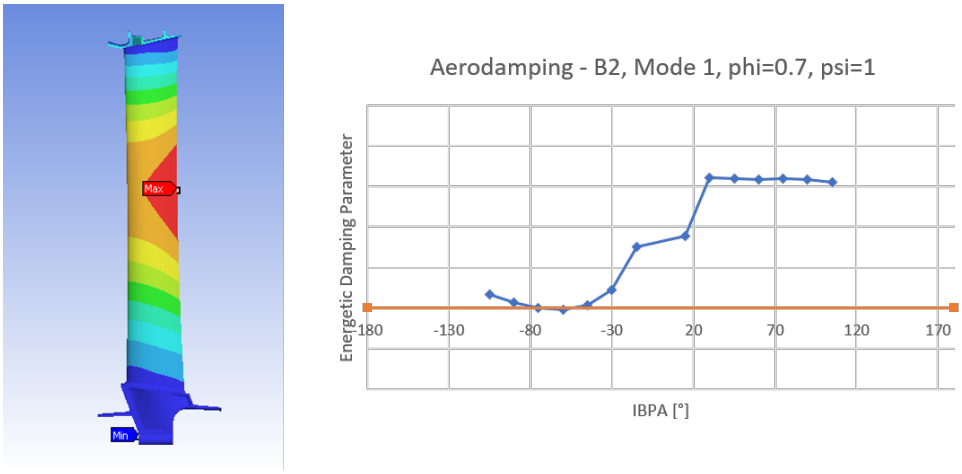

Figure 59: Case 2. Total deformation and Aeroplot for Blade 2, Mode 1.

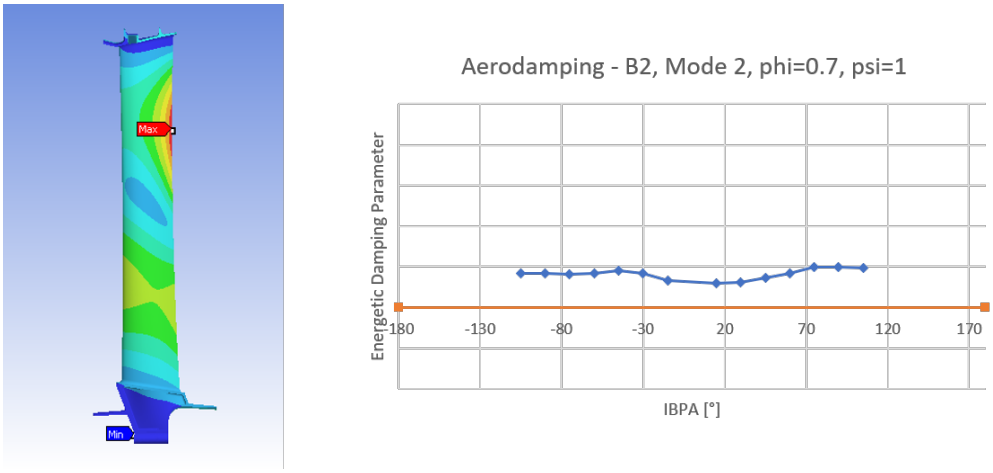

Figure 60: Case 2. Total deformation and Aeroplot for Blade 2, Mode 2.

Blade 1 shows flutter stability for both vibration modes, while Blade 2 shows negative values of the aerodamping coefficient for Mode 1 when $IBPA \simeq -60°$.

8.2.3 Case 3: ϕ=0.7, ψ=1.7

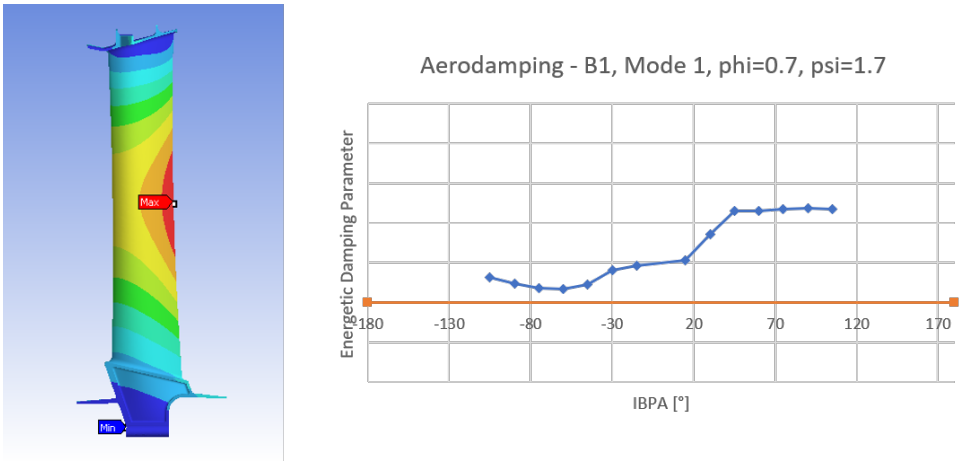

Figure 61: Case 3. Total deformation and Aeroplot for Blade 1, Mode 1.

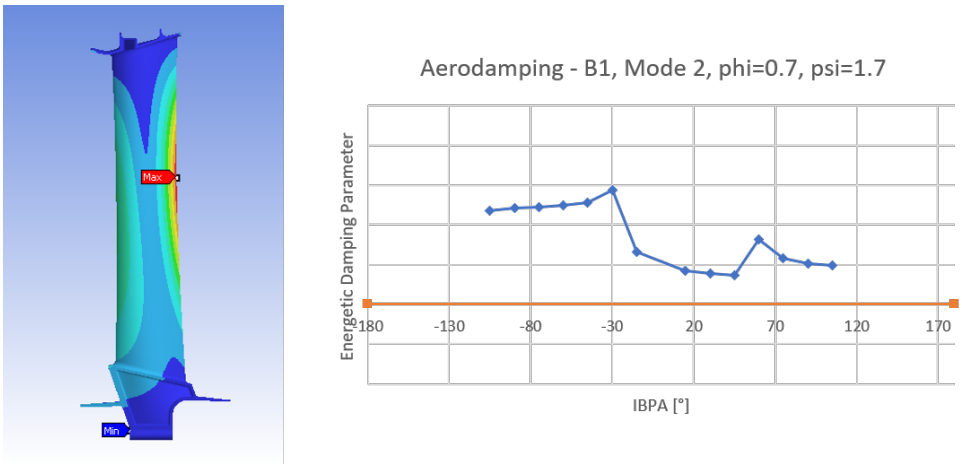

Figure 62: Case 3. Total deformation and Aeroplot for Blade 1, Mode 2.

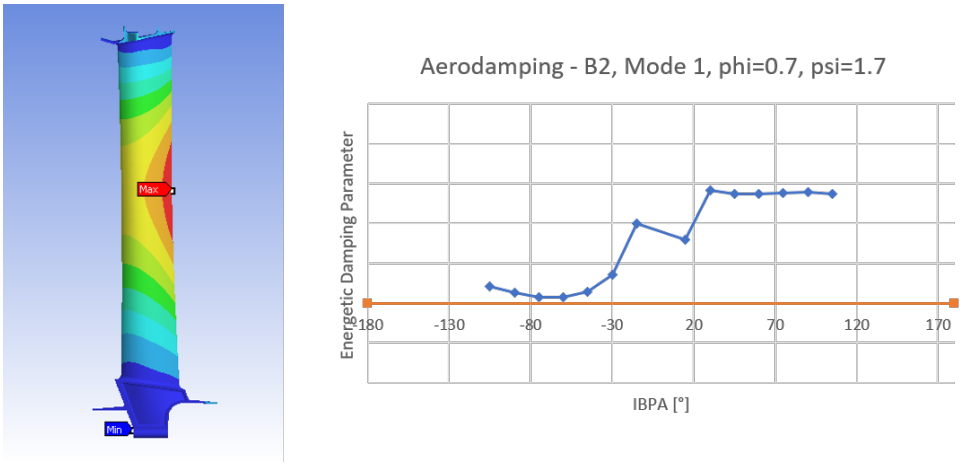

Figure 63: Case 3. Total deformation and Aeroplot for Blade 2, Mode 1.

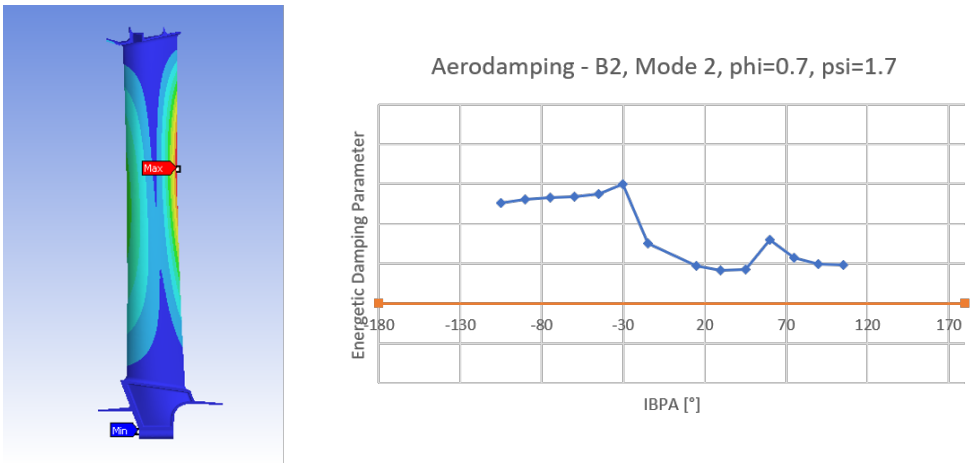

Figure 64: Case 3. Total deformation and Aeroplot for Blade 2, Mode 2.

By increasing ψ and keeping ϕ constant with respect to *Case 2*, the minimum value of the aerodamping coefficient increases for both Blade 1 and Blade 2 in both vibrating modes. In particular, Blade 2 does not show anymore flutter instability for Mode 1.

8.2.4 Case 4: ϕ=0.7, ψ=2.2

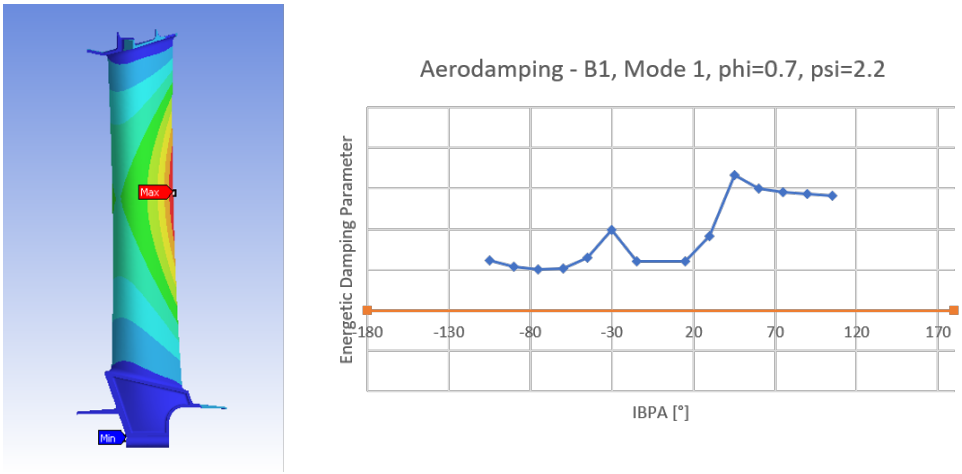

Figure 65: Case 4. Total deformation and Aeroplot for Blade 1, Mode 1.

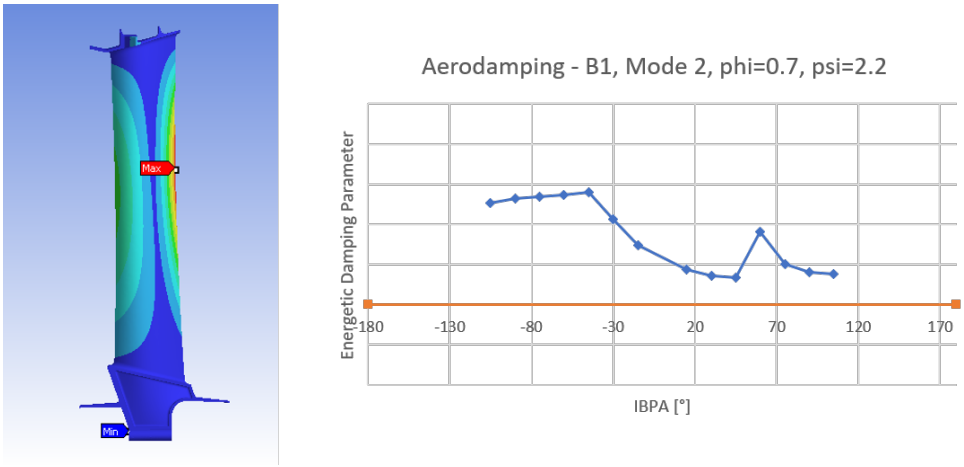

Figure 66: Case 4. Total deformation and Aeroplot for Blade 1, Mode 2.

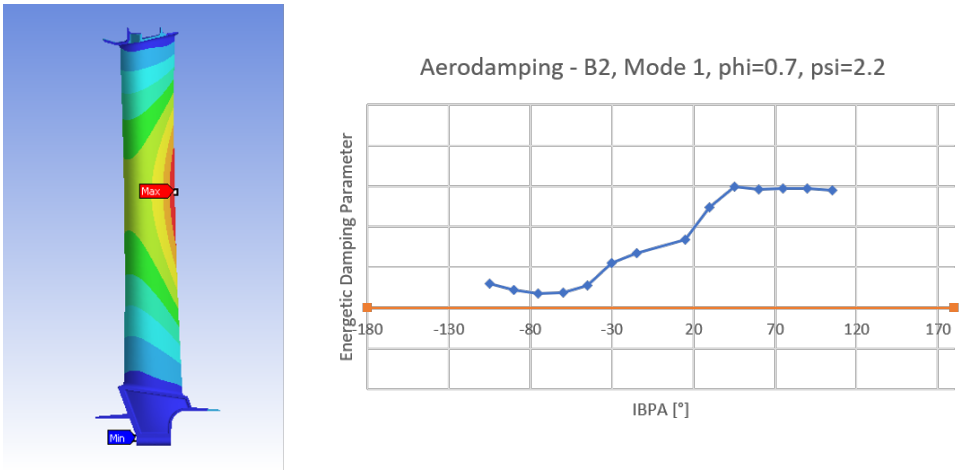

Figure 67: Case 4. Total deformation and Aeroplot for Blade 2, Mode 1.

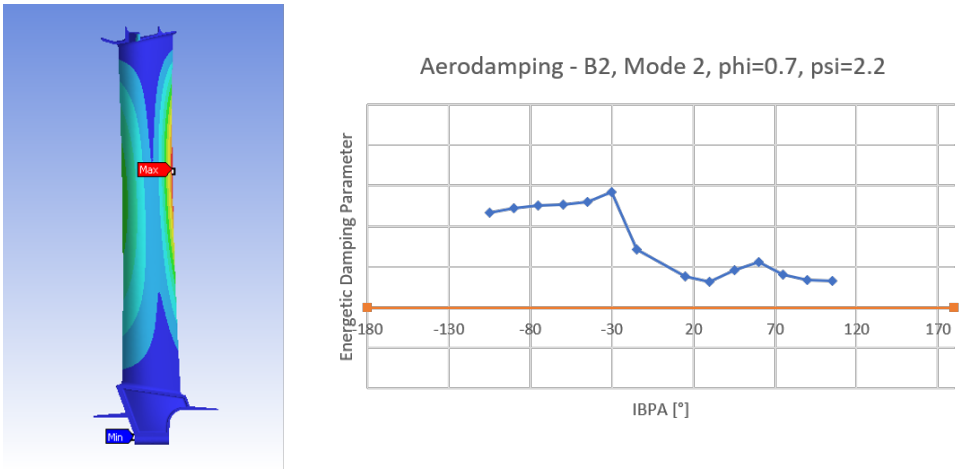

Figure 68: Case 4. Total deformation and Aeroplot for Blade 2, Mode 2.

By furtherly incrementing ψ at constant ϕ, the minimum aerodamping value continues to increase for both Blade 1 and Blade 2 with regard to Mode 1. However, for Mode 2 the trend remains approximately stable with respect to *Case 3*.

8.2.5 Case 5: ϕ=0.8, ψ=1.4

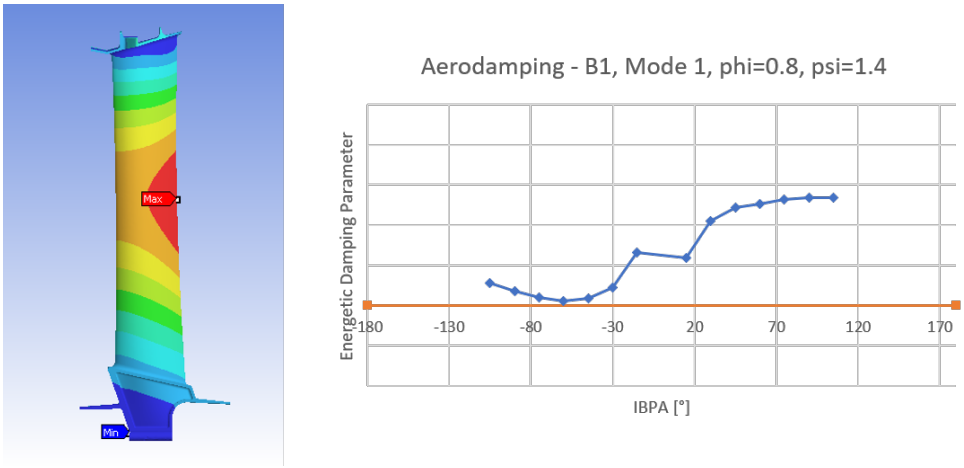

Figure 69: Case 5. Total deformation and Aeroplot for Blade 1, Mode 1.

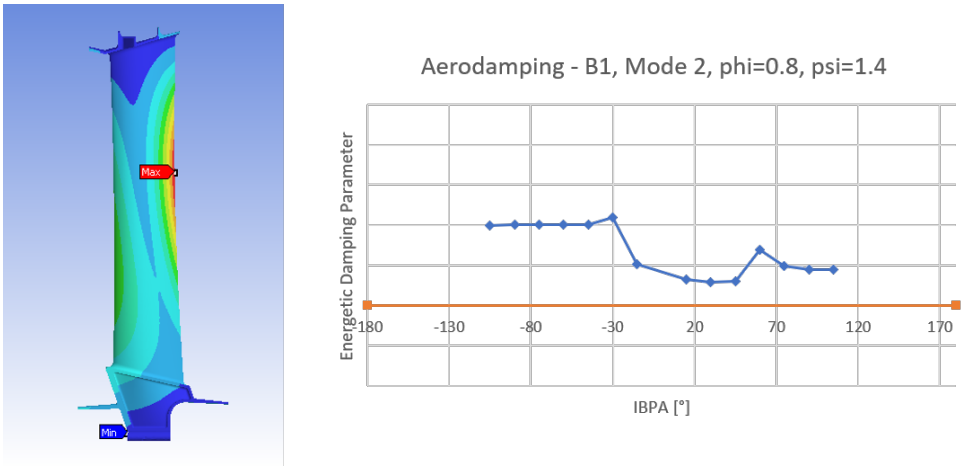

Figure 70: Case 5. Total deformation and Aeroplot for Blade 1, Mode 2.

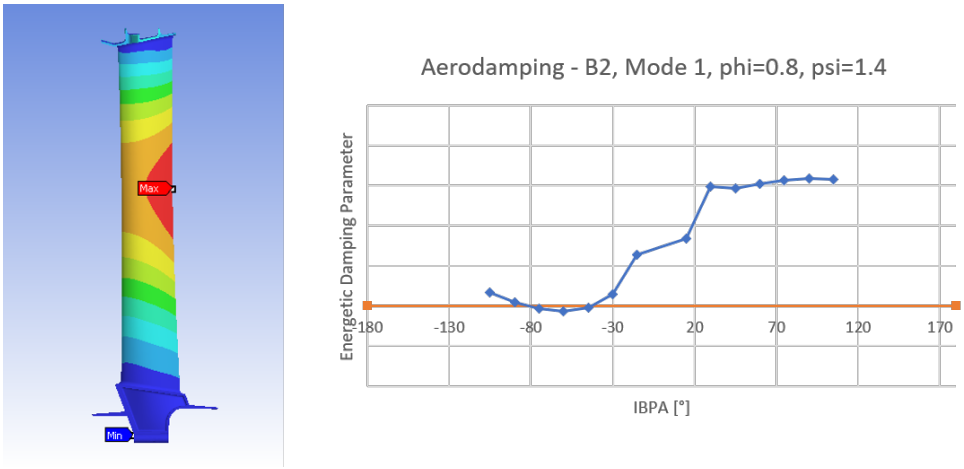

Figure 71: Case 5. Total deformation and Aeroplot for Blade 2, Mode 1.

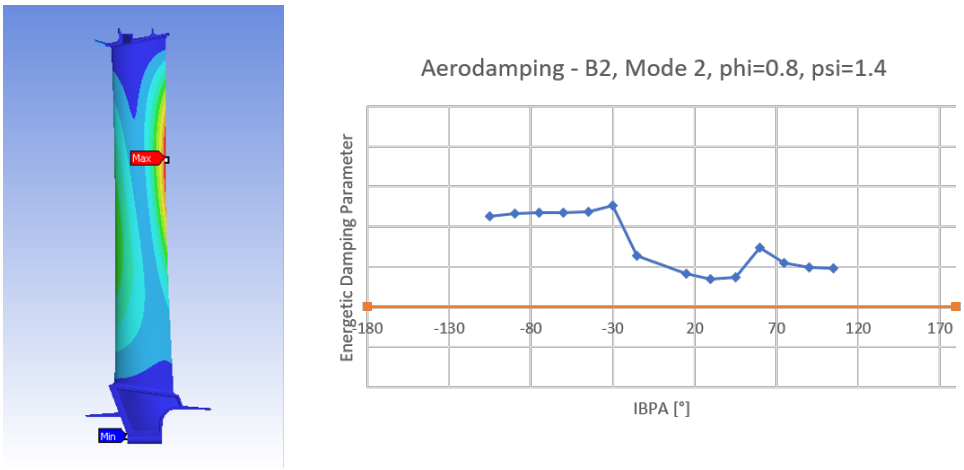

Figure 72: Case 5. Total deformation and Aeroplot for Blade 2, Mode 2.

By increasing ϕ, the aeromechanical behaviour gets worse for both blades; in particular, there is a new condition of flutter instability for Blade 2 in Mode 1, for $IBPA = -75° \div -45°$.

8.2.6 Case 6: ϕ=0.8, ψ=2.8

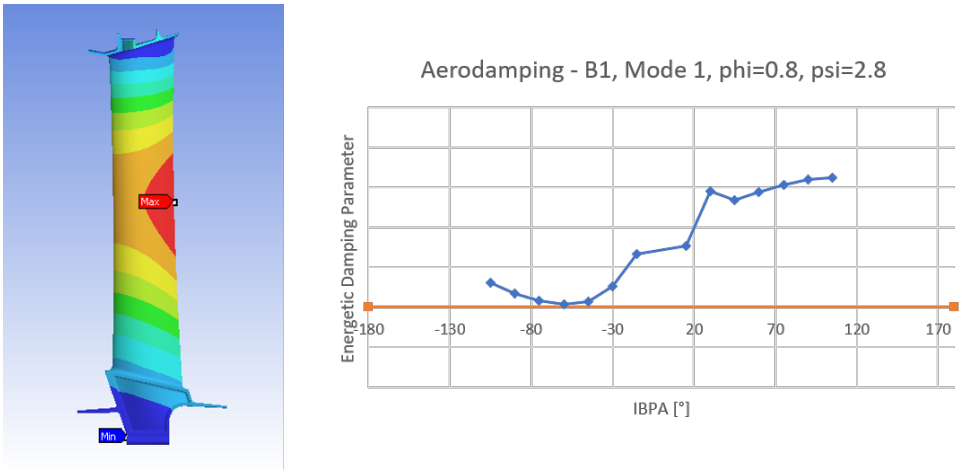

Figure 73: Case 6. Total deformation and Aeroplot for Blade 1, Mode 1.

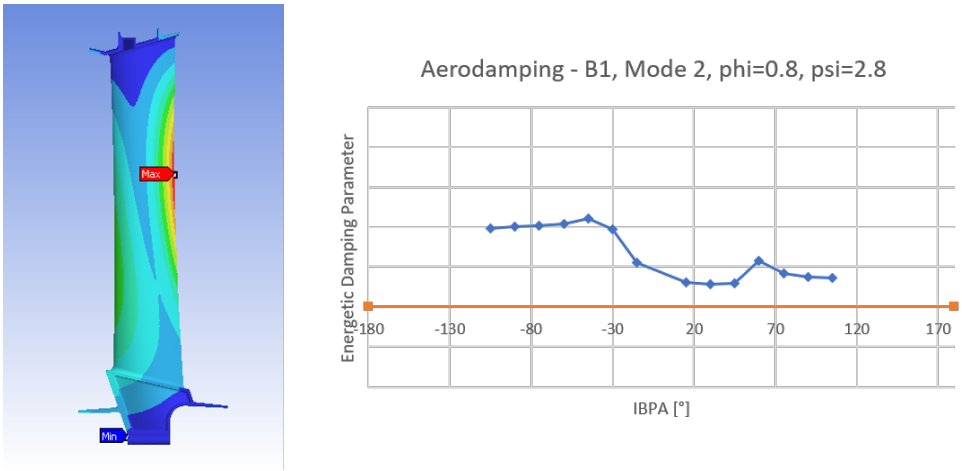

Figure 74: Case 6. Total deformation and Aeroplot for Blade 1, Mode 2.

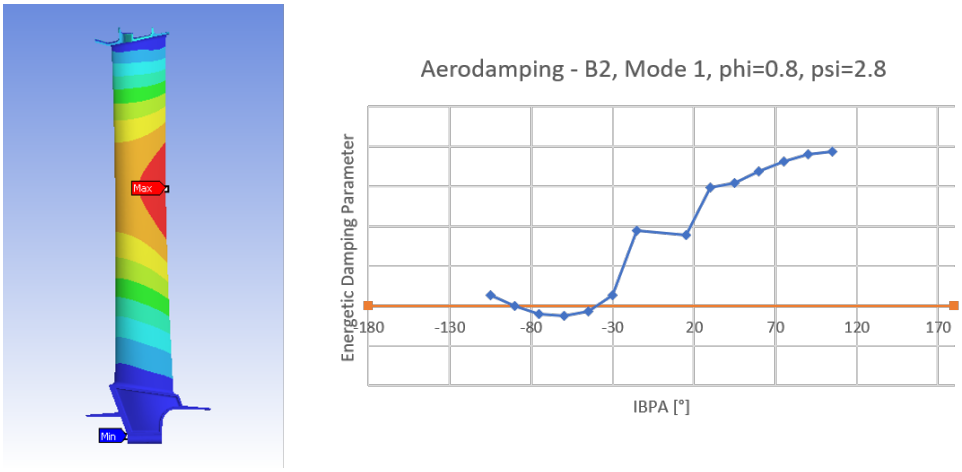

Figure 75: Case 6. Total deformation and Aeroplot for Blade 2, Mode 1.

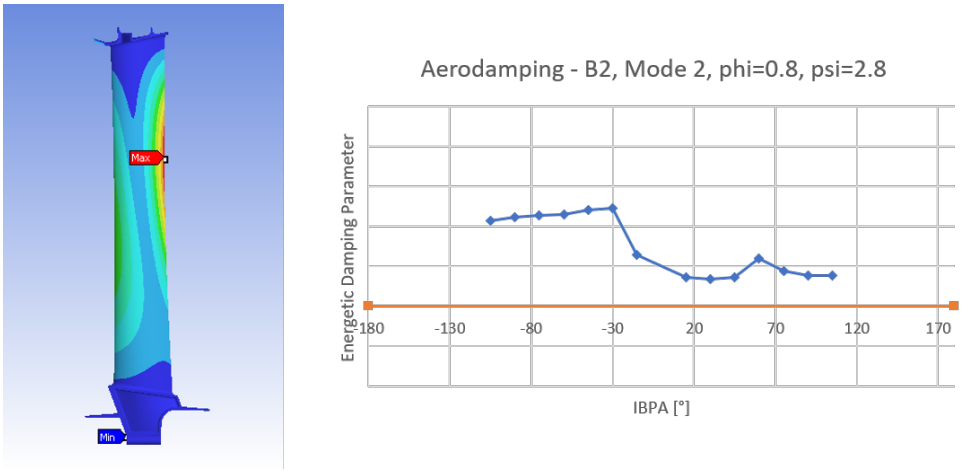

Figure 76: Case 6. Total deformation and Aeroplot for Blade 2, Mode 2.

By maintaining $\phi = const$ and increasing ψ with respect to *Case 5*, aerodamping trends remain approximately constant for both Blade 1 and Blade 2 in Mode 2. However, with regard to Mode 1, both blades show a worsening in the aeromechanical behaviour and the range of flutter instability for Blade 2 in Mode 1 widens, as negative aerodamping can be found for $IBPA = -90° \div -45°$.

8.2.7 Case 7: ϕ=0.9, ψ=1.9

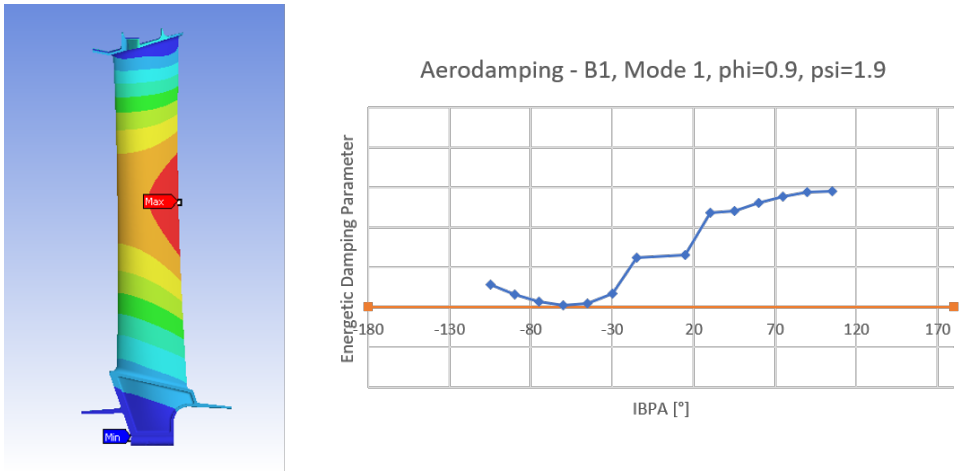

Figure 77: Case 7. Total deformation and Aeroplot for Blade 1, Mode 1.

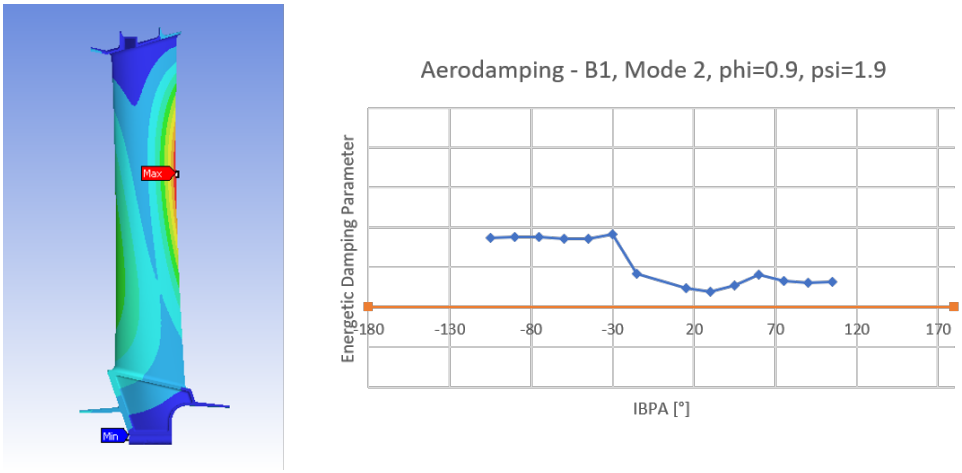

Figure 78: Case 7. Total deformation and Aeroplot for Blade 1, Mode 2.

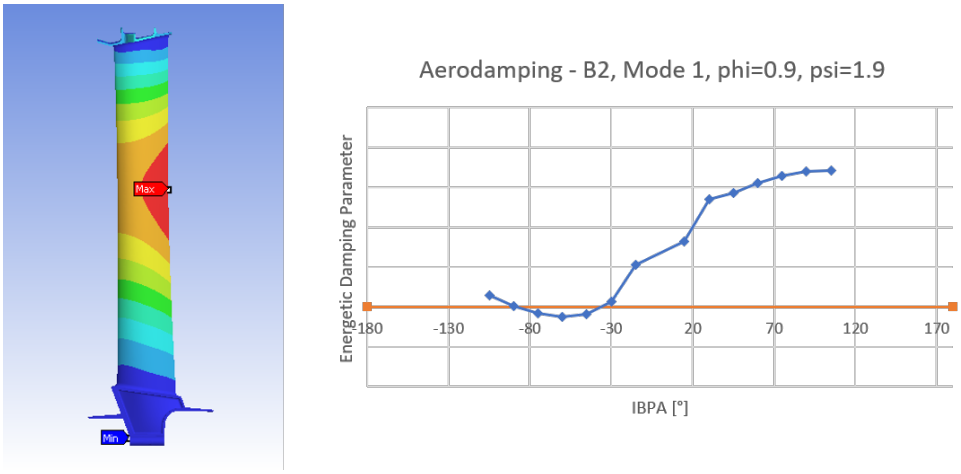

Figure 79: Case 7. Total deformation and Aeroplot for Blade 2, Mode 1.

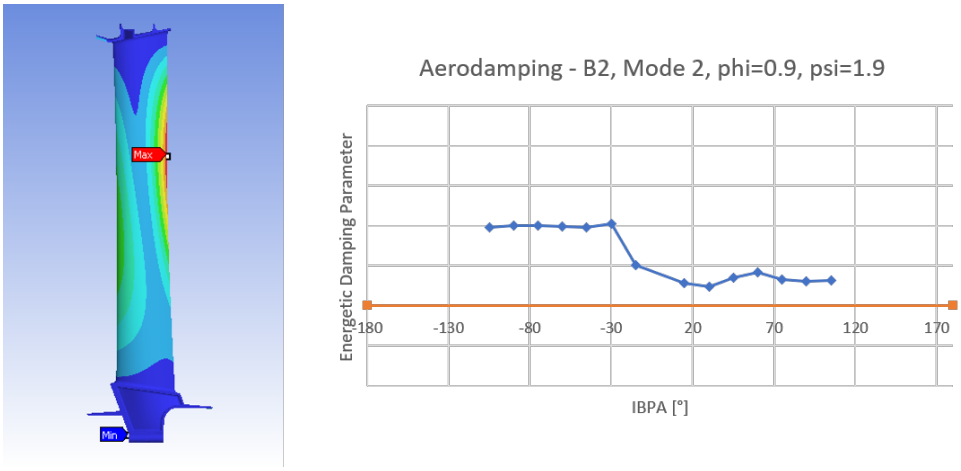

Figure 80: Case 7. Total deformation and Aeroplot for Blade 2, Mode 2.

By ulteriorly increasing ϕ with respect to *Case 6* and for the considered value of ψ, there is a slight worsening in the aeromechanical behaviour for both blades in both vibrating modes, with aerodamping minimum values that slightly decrease for all subcases and the range of negative aerodamping for Blade 2 in Mode 1 that increases ($IBPA = -105° \div -15°$).

8.2.8 Case 8: ϕ=1.1, ψ=1.6

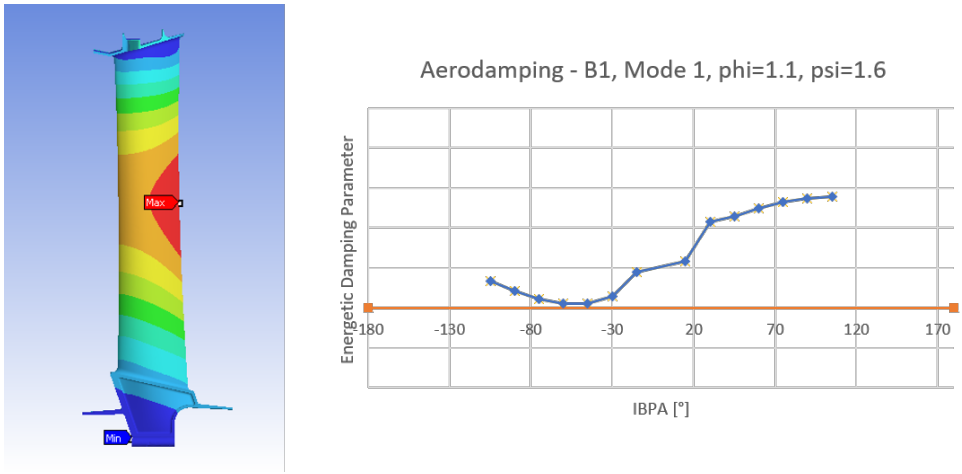

Figure 81: Case 8. Total deformation and Aeroplot for Blade 1, Mode 1.

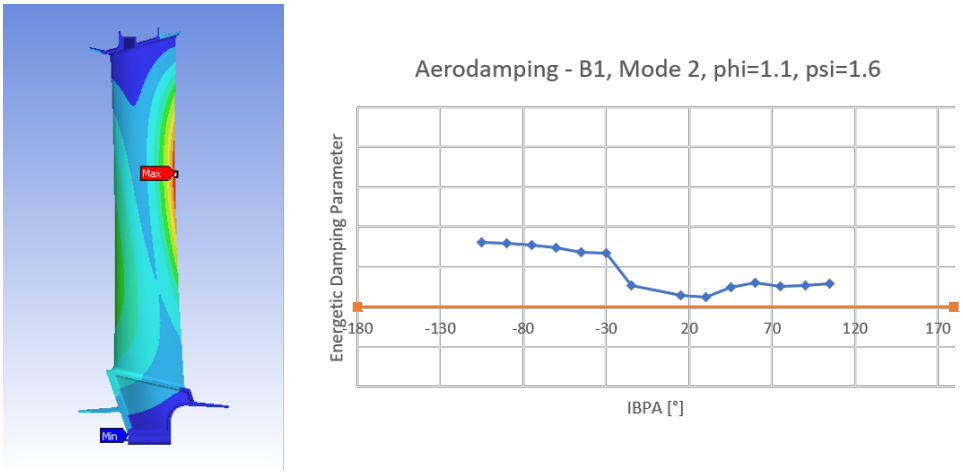

Figure 82: Case 8. Total deformation and Aeroplot for Blade 1, Mode 2.

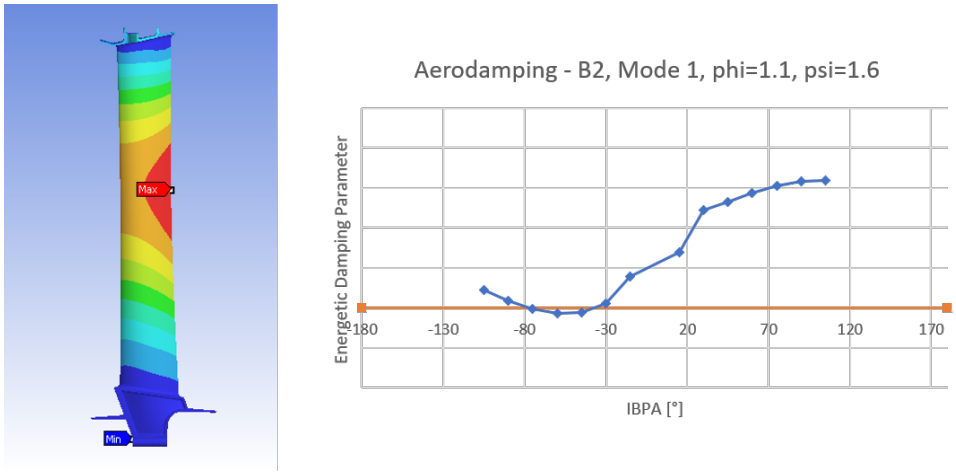

Figure 83: Case 8. Total deformation and Aeroplot for Blade 2, Mode 1.

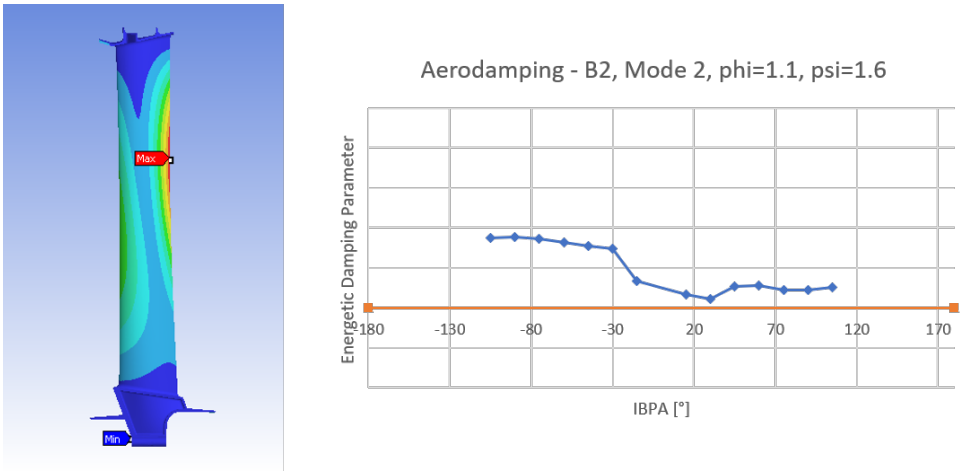

Figure 84: Case 8. Total deformation and Aeroplot for Blade 2, Mode 2.

By increasing ψ and decresing ϕ with respect to *Case 7*, there are no significant changes in the aerodamping trends.

8.2.9 Case 9: ϕ=1.2, ψ=2

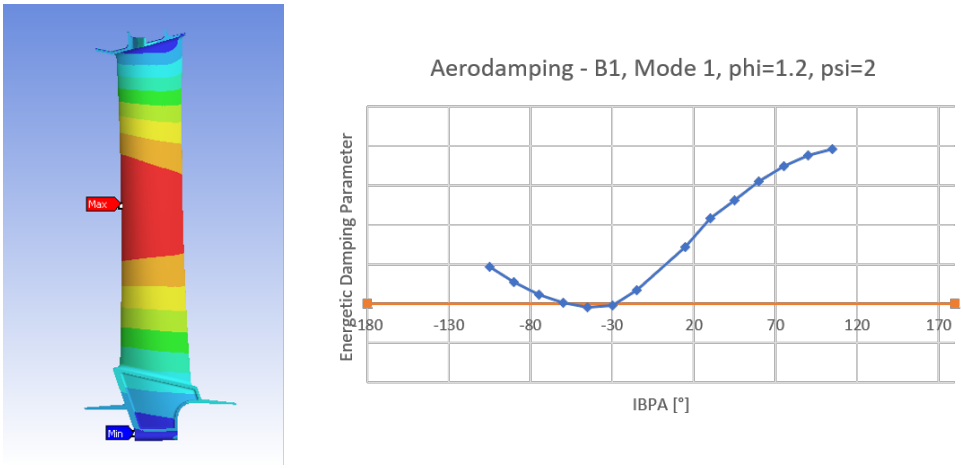

Figure 85: Case 9. Total deformation and Aeroplot for Blade 1, Mode 1.

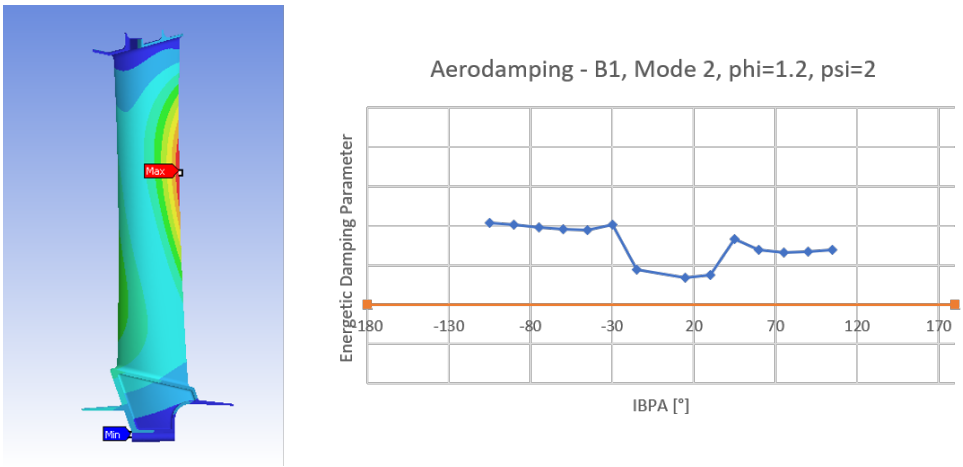

Figure 86: Case 9. Total deformation and Aeroplot for Blade 1, Mode 2.

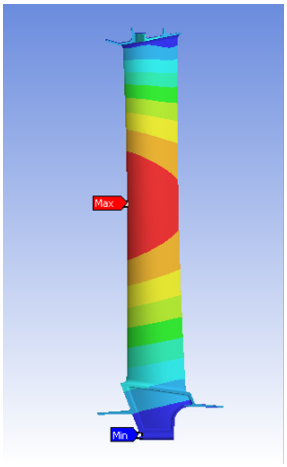

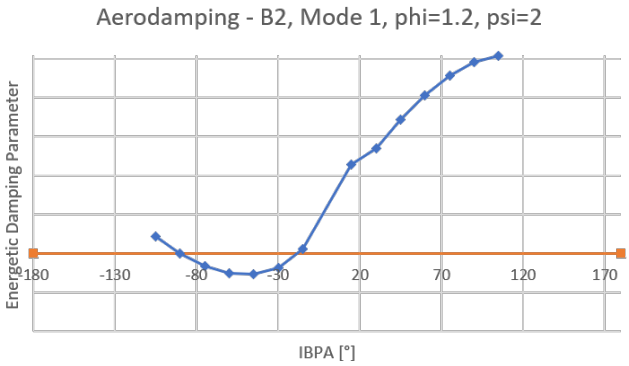

Figure 87: Case 9. Total deformation and Aeroplot for Blade 2, Mode 1.

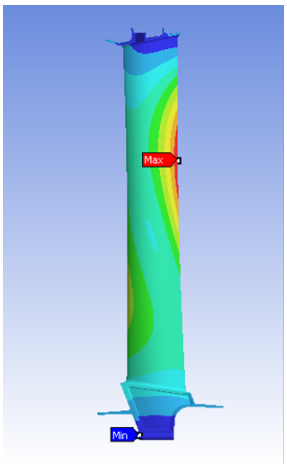

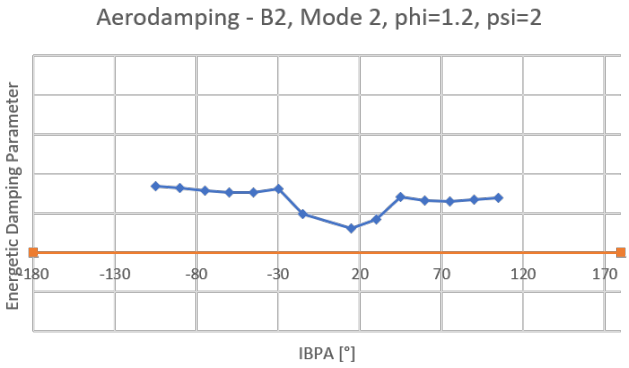

Figure 88: Case 9. Total deformation and Aeroplot for Blade 2, Mode 2.

Both ϕ and ψ are increased with respect to *Case 8*. The minimum aerodamping value becomes lower for both Blade 1 and Blade 2 in Mode 1, with the presence of a region of instability, which occurs for $IBPA = -45° \div -30°$ for Blade 1 and for $IBPA = -90° \div -30°$ for Blade 2. With regard to Mode 2, instead, the aeromechanical behaviour shows an improvement for both blades.

8.2.10 Case 10: ϕ=1.3, ψ=1.1

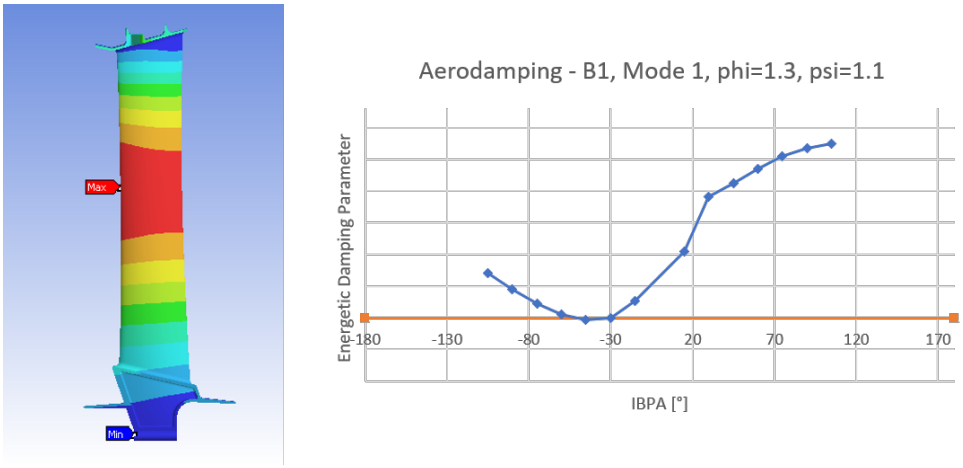

Figure 89: Case 10. Total deformation and Aeroplot for Blade 1, Mode 1.

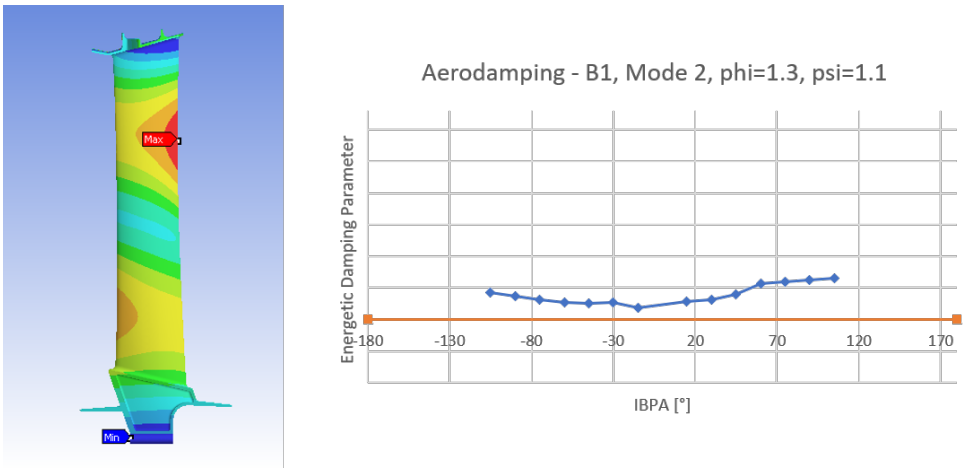

Figure 90: Case 10. Total deformation and Aeroplot for Blade 1, Mode 2.

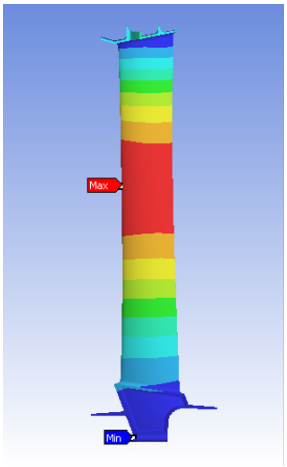

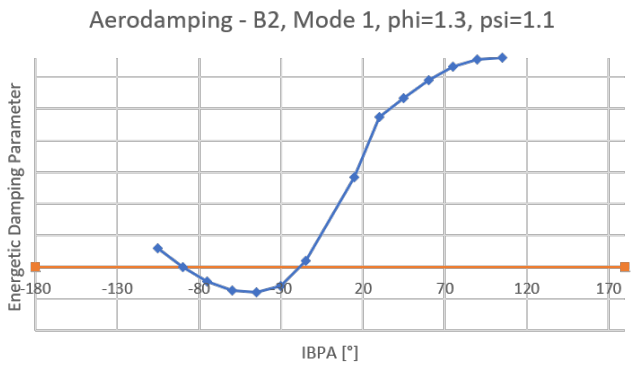

Figure 91: Case 10. Total deformation and Aeroplot for Blade 2, Mode 1.

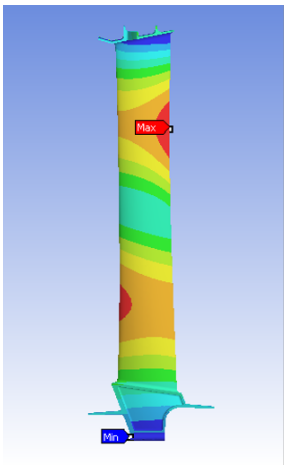

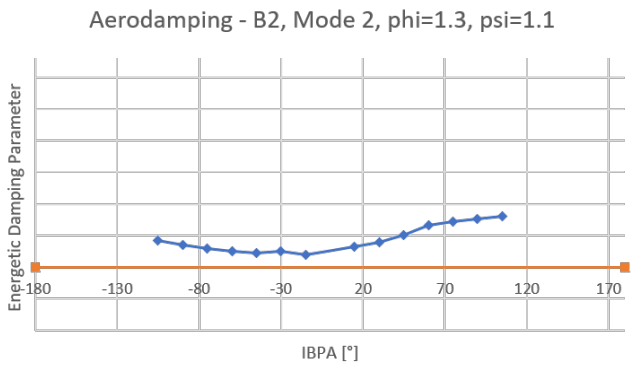

Figure 92: Case 10. Total deformation and Aeroplot for Blade 2, Mode 2.

This case features the greatest value of ϕ considered in the whole study and a relatively low value of ψ. Both blades show a region of aeromechanical instability for Mode 1, within IBPA ranges comparable with those found for *Case 9*. As regard Mode 2, both blades prove stable.

8.2.11 Case 11: ϕ=1.3, ψ=2.5

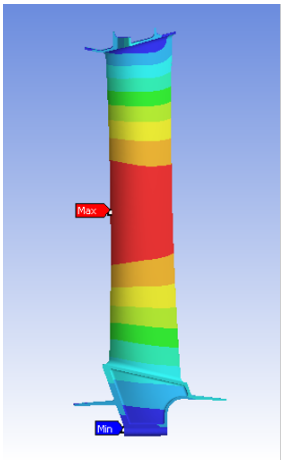

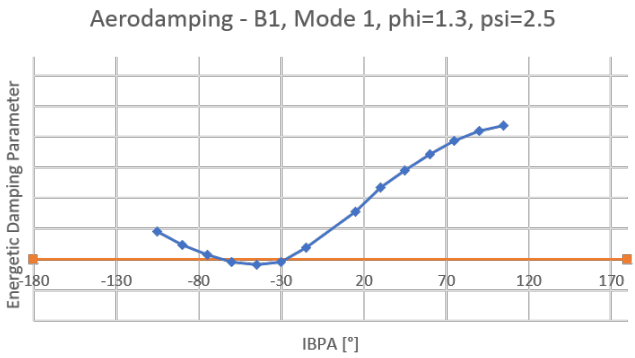

Figure 93: Case 11. Total deformation and Aeroplot for Blade 1, Mode 1.

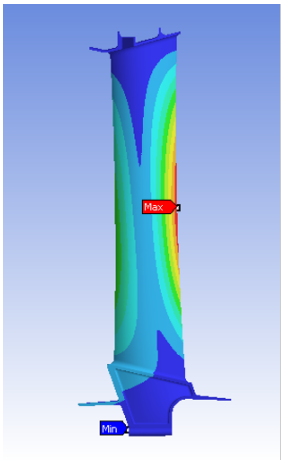

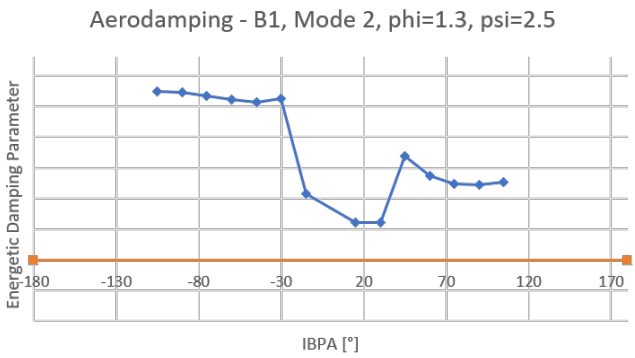

Figure 94: Case 11. Total deformation and Aeroplot for Blade 1, Mode 2.

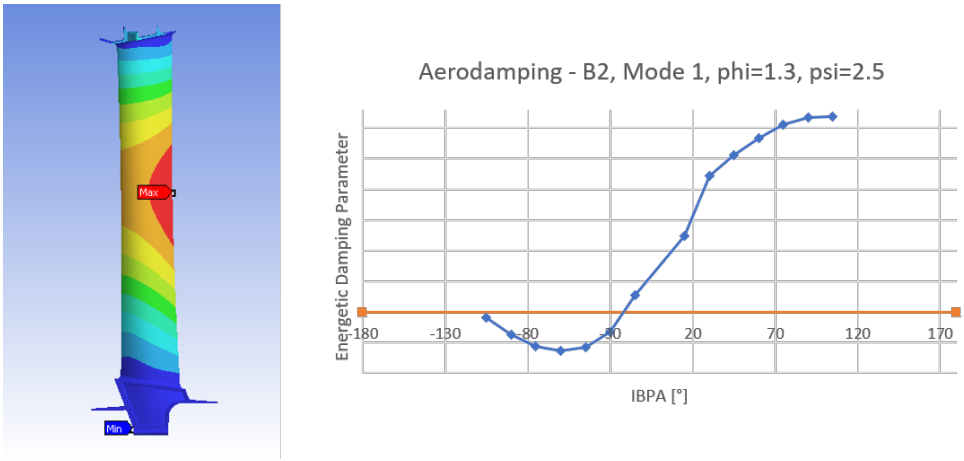

Figure 95: Case 11. Total deformation and Aeroplot for Blade 2, Mode 1.

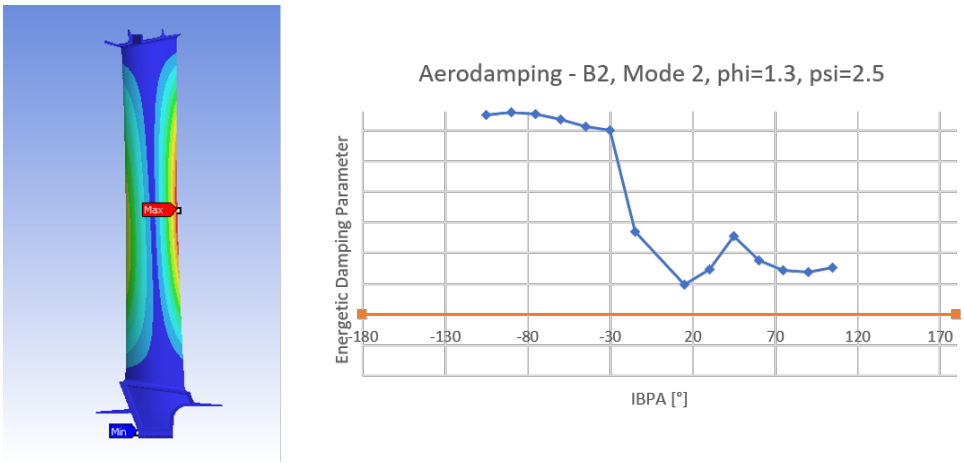

Figure 96: Case 11. Total deformation and Aeroplot for Blade 2, Mode 2.

With respect to *Case 10*, ϕ is kept constant while ψ is increased. This leads to a wider range of flutter instability for both blades in Mode 1; in particular, Blade 1 shows instability for $IBPA = -60° \div -30°$, while Blade 2 is not stable for $IBPA = -105° \div -30°$. The minimum value of the aerodamping gets lower for both blades in both modes.

8.2.12 Case 12: ϕ=1, ψ=1.1

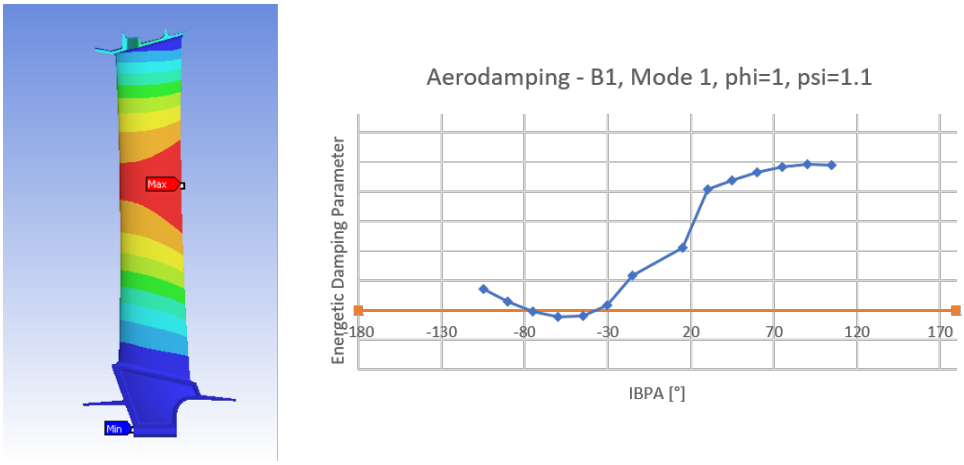

Figure 97: Case 12. Total deformation and Aeroplot for Blade 1, Mode 1.

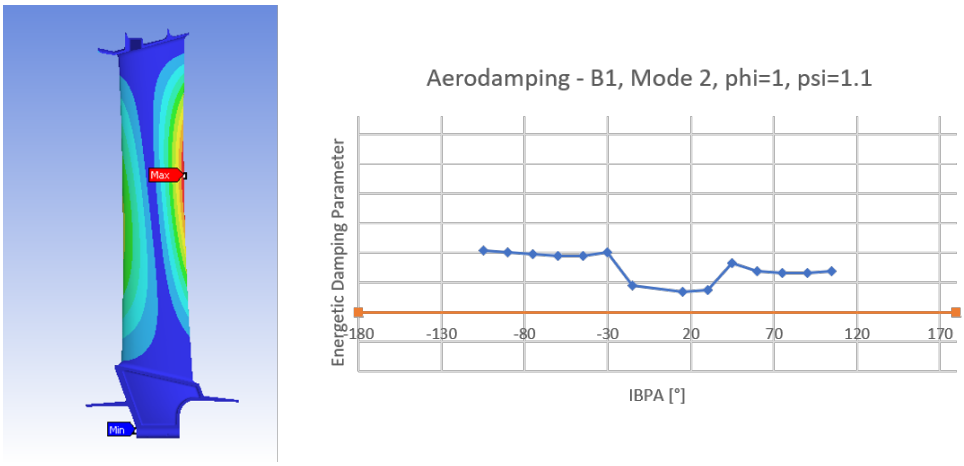

Figure 98: Case 12. Total deformation and Aeroplot for Blade 1, Mode 2.

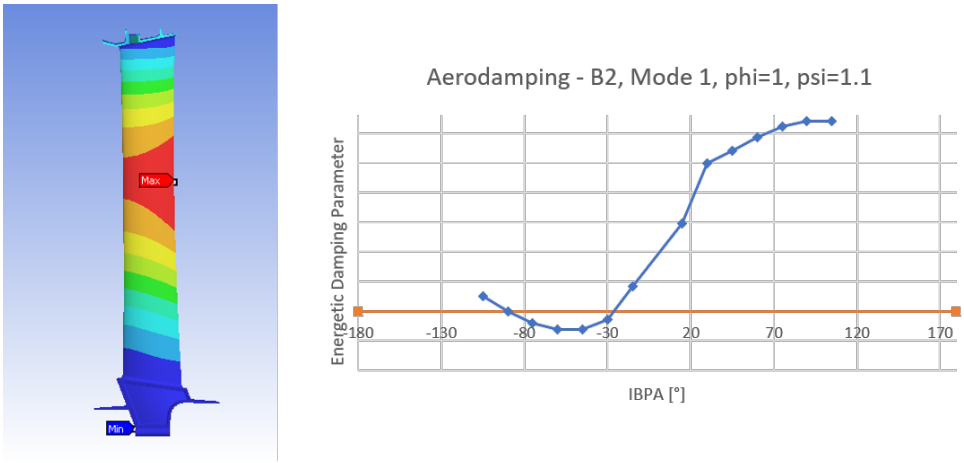

Figure 99: Case 12. Total deformation and Aeroplot for Blade 2, Mode 1.

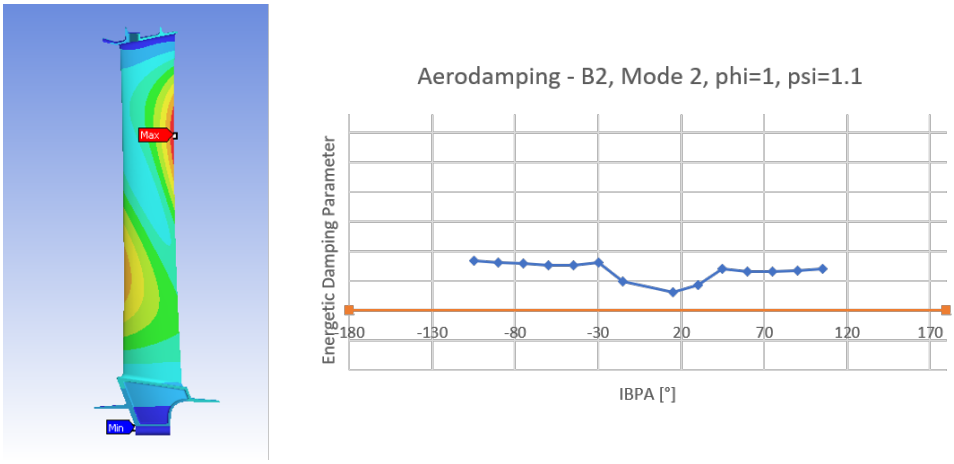

Figure 100: Case 12. Total deformation and Aeroplot for Blade 2, Mode 2.

In this test case, both Blade 1 and Blade 2 show flutter instability in Mode 1, while they are stable in Mode 2.

8.2.13 Case 13: ϕ=1, ψ=2.4

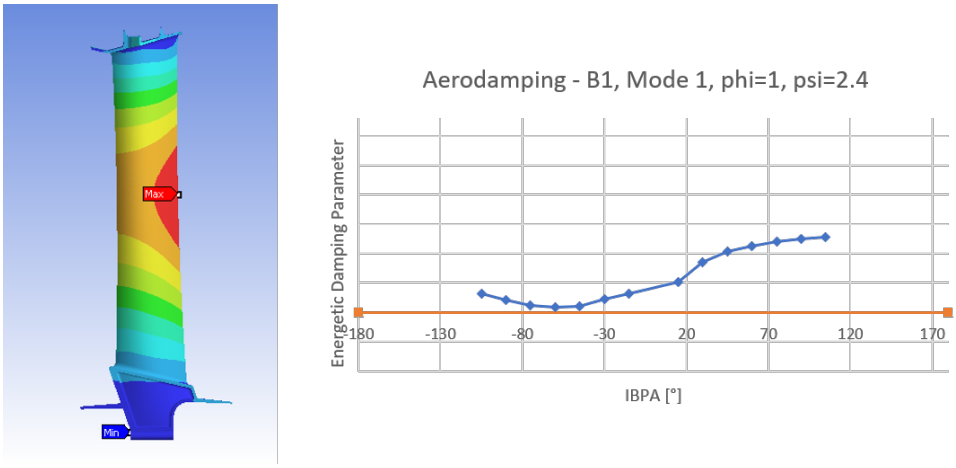

Figure 101: Case 13. Total deformation and Aeroplot for Blade 1, Mode 1.

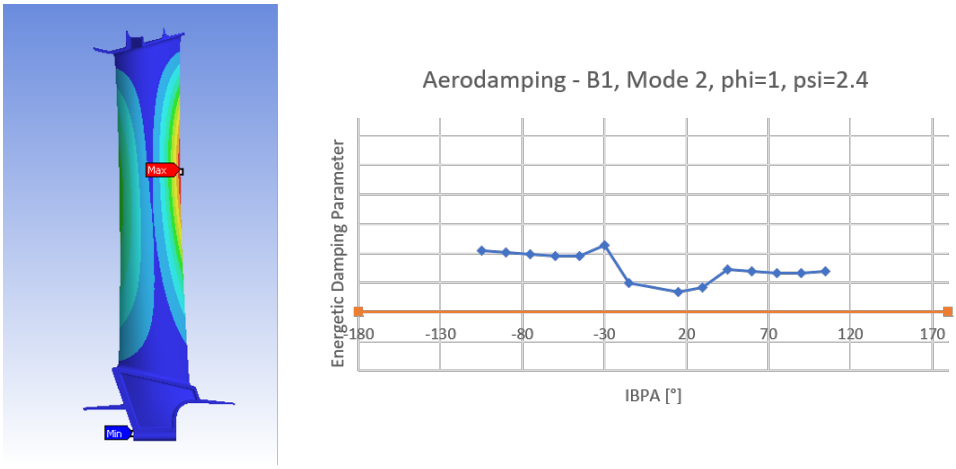

Figure 102: Case 13. Total deformation and Aeroplot for Blade 1, Mode 2.

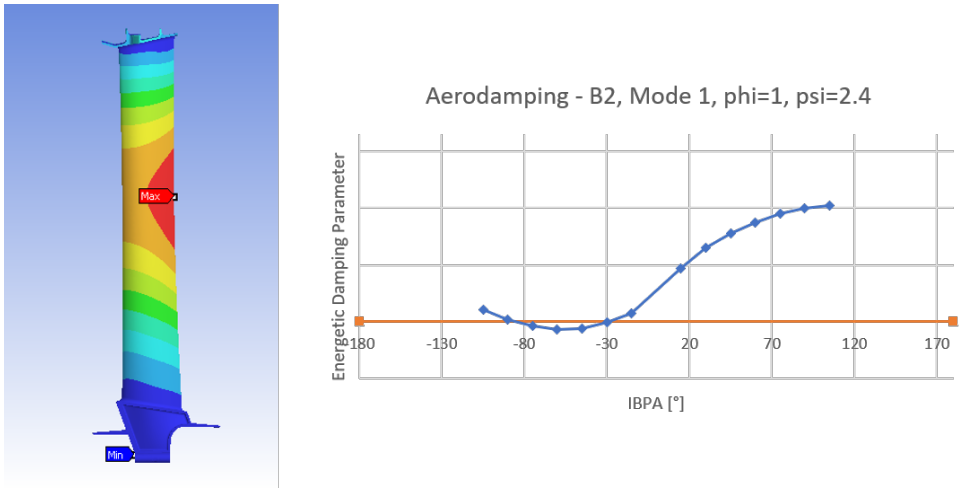

Figure 103: Case 13. Total deformation and Aeroplot for Blade 2, Mode 1.

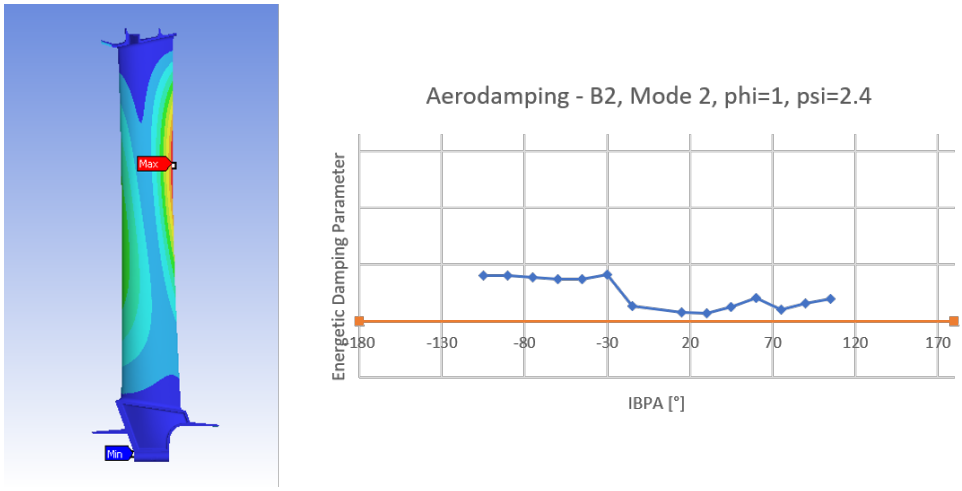

Figure 104: Case 13. Total deformation and Aeroplot for Blade 2, Mode 2.

With respect to *Case 12*, ϕ is kept constant while ψ is increased. The minimum values of aerodamping increase for both blades in both vibrating modes; however, while Blade 1 results now stable in Mode 1, Blade 2 still shows a range of flutter instability in Mode 1 for $IBPA = -75° \div -30°$.

9 Conclusions

The operational points considered in this Thesis Work are represented on the Smith Chart in Figure 105 and Figure 106. The red points represent the conditions for which the blade shows flutter instability, which means that negative aerodamping values occur for a certain range of IBPA values. Both green and yellow points represent, instead, a stability condition. However, after evaluating the average value of the minimun aerodamping coefficient for the considered blade and mode, a further distinction has been made between the operational points that show good aeromechanical behaviour (i.e. minumum aerodamping coefficient above average) and operational points that show an intermediate aeromechanical behaviour (i.e. minumum aerodamping coefficient below average but still positive).

Firstly, it can be observed that there is no complete matching between the aerodynamic optimum (represented by the *Optimum Line*) and the aeromechanical optimum. In general, by moving towards the area with high ϕ and ψ values, the aeromechanical behaviour tends to get worse. This is especially true for Blade 2, which shows instability for at least one of the two considered vibrating modes in a wide region for $\phi > 0.7$. For Blade 1, the best condition appears to be the one with $\phi = 0.7$, $\psi = 1.7$, which falls on the optimum line and shows a good aeromechanical behaviour as well. The operating point with $\phi = 0.8$, $\psi = 1.8$ also shows good performance from both the aerodynamic and the aeromechanical point of view; moreover, it has to be taken into account that a higher *Stage Loading Coefficient* will lead to a lower number of turbine stages, which results in a reduction in the turbine module's dimension and weight. With regard to Blade 2, the considerations on the aeromechanical behaviour impose a quite strong limit on the aera of the Smith Chart that can be considered for the turbine design ($\phi < 0.7$); as for Blade 1, the best compromise appers to be the one with $\phi = 0.7$, $\psi = 1.7$.

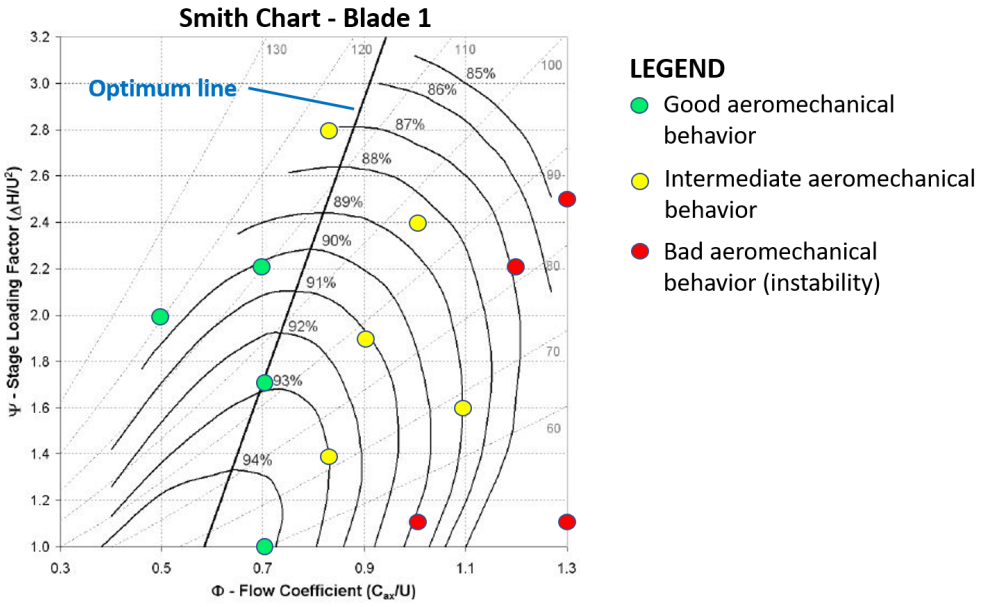

Figure 105: Smith Chart with operating points for Blade 1.

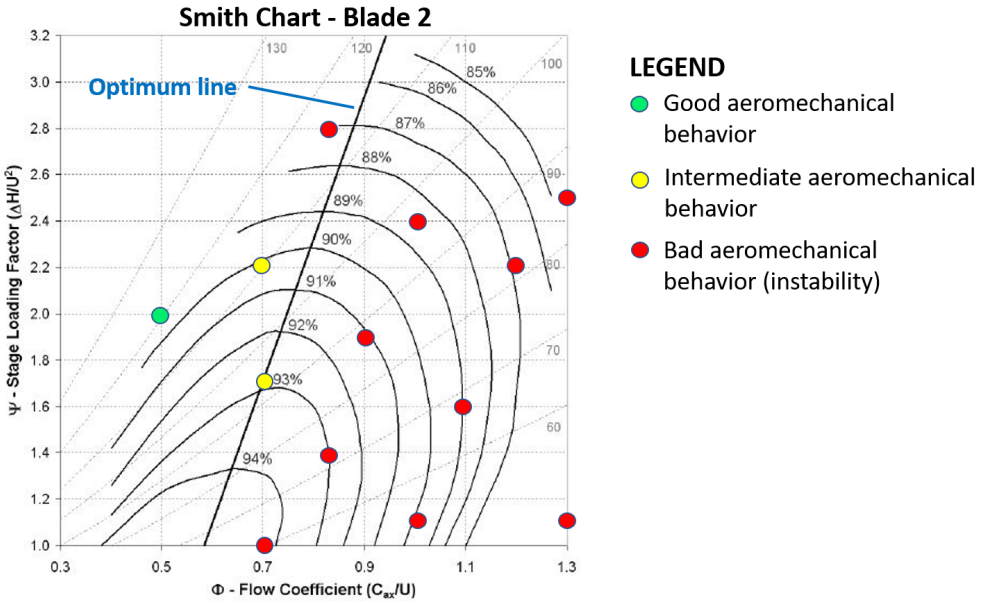

Figure 106: Smith Chart with operating points for Blade 2.

These observations lead to the conclusion that a multidimensional optimization process is required in order to obtain a blade geometry that not only allows to reach a good overall turbine effciency, but also proves stable to flutter phenomena. Finding a good compromise between the two aspects is essential and it is a goal that needs to be accomplished as early as possibile in the design phase. Therefore, having fast feedbacks from the aeromechanical point of view is of outmost importance and all the efforts that are being made in this direction, thorugh the integration and the automation of the preliminary design phase, will allow to reach increasingly good results with costs and time saving. Further development of the study considered in this Thesis Project may hence include analyses aimed at expanding the available database; this goal could be pursued by extending the analysis to the stator's vanes or by considering additional variations of the operating parameters as, for instance, Zweifel Coefficient values other that 1 or Degree of Reaction values other than 0.7, so that the optimum values from the aeromechanical point of view can be found.

References

[1] Rolls Royce, *The Jet Engine*, John Wiley & Sons, 2015

[2] Hill P.G., Peterson C.R., *Mechanics and Thermodynamics of Propulsion*, Addison-Wesley Publishing Company, 1992.

[3] J.H. Horlock, *Axial Flow Turbine*, Butterworth Published 621-154, 1966

[4] Blazek G., *Computational Fluid Dynamics: Principles and Applications*, Butterworth-Heinemann, 2015

[5] S.F. Smith, *A Simple Correlation of Turbine Efficiency*, Journal of Royal Aeronautical Society, 1965

[6] Hart C., *The prehistory of fight*, University of California Press Berkeley, 1985

[7] Shapiro A.H., Soderberg C.R., Stenning A.H., Taylor E.S., and Horlock J.H., *Notes of turbomachinery*, Department of Mechanical Engineering, Massachussets Institute of tecnology, 1957

[8] Fung Y. C., *An introduction to the theory of aeroelasticity*, Courier Dover Publications, 2008

[9] Farrashkhalvat M., Miles J.P., *Basic structured grid generation*, Butterworth-Heinemann, 2003

[10] Bern M., Plassmann P. , *Handbook of Computational Geometry*, Elsevier Science, 2000

[11] Chapman L., *Transport and climate change: a review*, Journal of transport geography, 354-367, 2007

[12] Bertini F., Ampellio E., Marconcini M., Giovannini M., *A critical numerical review of loss correlation models amd smith diagram for modern low pressure turbine stages*, ASME paper GT2013-94849, 2013

[13] Pierre C., *Mode Localization and Eigenvalue Loci Veering Phenomena in Disordered Structures*, Journal of Sound and Vibration, 126:485–502, 1988

[14] Srinivasan A.V., *Flutter and Resonant Vibration Characteristics of Engine Blades*, Journal of Engineering for Gas Turbines and Power, 742-775, 1997

[15] Arnone A., *Viscous Analysis of Three-Dimensional Rotor Flow Using a Multigrid Method*, ASME Journal of Turbomachinery, 435-445, 1994

[16] Arnone A., Pacciani R., *Rotor-Stator Interaction Analysis Using the Navier-Stokes Equations and a Multigrid Method*, ASME Journal of Turbomachinery, 679-689, 1996

[17] Coller B.D., Chamara P. A., *Structural non-linearities and the nature of the classic futter instability*, Journal of Sound and Vibration, 711-739, 2004

[18] Collar A.R., *The expanding domain of aeroelasticity*, The Aeronautical Journal, 613-636, 1946

[19] Giuseppe Battiato, *Vibrations prediction and measurement of multistage bladed disks with non-linear behavior due to friction contacts*, Tesi di Dottorato, Politecnico di Torino, 2017

[20] Federico Piccini, *Revisione di regole di base per progetto di turbine assiali*, Tesi di Laurea Magistrale, Politecnico di Torino, 2012

[21] Fabiola Cremonesi, *Stima delle performance di turbine aeronautiche di bassa pressione in analisi monodimensionali*, Tesi di Laurea Magistrale, Università degli Studi di Padova, 2014

[22] Riccardo Scarpulla, *Metodologia avanzata per la simulazione aeromeccanica di LPT per motori aeronautici commerciali*, Tesi di Laurea Magistrale, Politecnico di Torino, 2019

[23] Christian Fantino, *Caratterizzazione Dinamica di un Rotore LPT in Presenza di Mistuning Intenzionale*, Tesi di Laurea Magistrale, Politecnico di Torino, 2018

[24] Gianluca Mosiello, *Development of Intentional Mistuning Technologies applied to Aircraft Engines' Turbines Rotors aiming at Reducing Aeromechanical Instabilities*, Tesi di Laurea Magistrale, Politecnico di Torino, 2018

[25] Fabio Bellacicco, *Stabilizzazione di uno stadio di LPT bladed-disk in presenza della condizione di instabilità a flutter mediante mistuning intenzionale*, Tesi di Laurea Magistrale, Politecnico di Torino, 2016

[26] Andrea Bray, *Interazione fluido-struttura in turbine aeronautiche di bassa pressione*, Tesi di Laurea Magistrale, Politecnico di Torino, 2018

[27] *Great 2020*, URL: http://www.great2020.it

[28] *Idealized Brayton Cycle*, URL: https://en.wikipedia.org/wiki/Brayton_cycle

[29] *Quest for Performance: The Evolution of ModernAircraft*, URL: https://history.nasa.gov/SP-468/ch10-3.htm

[30] *Turboject Engine*, URL: https://en.wikipedia.org/wiki/Turbojet

[31] *Turbofan Engine*, URL: https://en.wikipedia.org/wiki/Turbofan

[32] *Turboprop Engine*, URL: https://en.wikipedia.org/wiki/Turboprop

[33] *Turboshaft Engine*, URL: https://en.wikipedia.org/wiki/Turboshaft

[34] *Twisted Contour of Blades*, URL: https://4.bp.blogspot.com/-4fiwsn3BOyw/UW1jMNG2frI/AAAAAAAAATo/S67NxzDU7X4/s1600/Picture1.png

[35] *Turbomachinery*, URL: https://www.avioaero.com/What/Turbomachinery

[36] *Example of Structured Grid*, URL: https://www.sciencedirect.com/topics/engineering/structured-grid

[37] *Structured Grid*, URL: https://commons.wikimedia.org/w/index.php?curid=1367873

[38] *Unstructured Grid*, URL: https://commons.wikimedia.org/w/index.php?curid=2358783